Mon. Not. R. Astron. Soc. **000**, 1–25 (2002) Printed 12 August 2021 (MN LATEX style file v2.2)

MOBSTER – VI. Centrifugal breakout reconnection as the electron acceleration mechanism powering the radio magnetospheres of early-type stars

M. E. Shultz[1⋆], S. P. Owocki[1], A. ud-Doula[2], A. Biswas[3], D. Bohlender[4], B. Das[3], A. David-Uraz[5,6], P. Chandra[3], V. Khalack[7], O. Kochukhov[8], J. D. Landstreet[9,10], P. Leto[11], D. Monin[4], C. Neiner[12], Th. Rivinius[13], and G. A. Wade[14]

[1] *Department of Physics and Astronomy, University of Delaware, 217 Sharp Lab, Newark, Delaware, 19716, USA*
[2] *Department of Physics, Penn State Scranton, Dunmore, PA 18512, USA*
[3] *National Centre for Radio Astrophysics, Tata Institute of Fundamental Research, Pune University Campus, Pune-411007, India*
[4] *National Research Council of Canada, Herzberg Astronomy and Astrophysics Research Centre, 5071 West Saanich Road, Victoria, BC V9E 2E7*
[5] *Department of Physics and Astronomy, Howard University, Washington, DC 20059, USA*
[6] *Center for Research and Exploration in Space Science and Technology, and X-ray Astrophysics Laboratory, NASA/GSFC, Greenbelt, MD 20771, USA*
[7] *Département de Physique et dAstronomie, Université de Moncton, Moncton, N.B., Canada E1A 3E9*
[8] *Department of Physics and Astronomy, Uppsala University, Box 516, Uppsala 75120, Sweden*
[9] *Armagh Observatory and Planetarium, College Hill, Armagh BT61 9DG, UK*
[10] *University of Western Ontario, London, Ontario, N6A 3K7, Canada*
[11] *INAF - Osservatorio Astrofisico di Catania, Via S. Sofia 78, 95123 Catania, Italy*
[12] *LESIA, Paris Observatory, PSL University, CNRS, Sorbonne Universit, Universit de Paris, 5 place Jules Janssen, 92195 Meudon*
[13] *ESO - European Organisation for Astronomical Research in the Southern Hemisphere, Casilla 19001, Santiago 19, Chile*
[14] *Department of Physics and Space Science, Royal Military College of Canada, Kingston, Ontario K7K 7B4, Canada*

ABSTRACT

Numerous magnetic hot stars exhibit gyrosynchrotron emission. The source electrons were previously thought to be accelerated to relativistic velocities in the current sheet formed in the middle magnetosphere by the wind opening magnetic field lines. However, a lack of dependence of radio luminosity on the wind power, and a strong dependence on rotation, has recently challenged this paradigm. We have collected all radio measurements of magnetic early-type stars available in the literature. When constraints on the magnetic field and/or the rotational period are not available, we have determined these using previously unpublished spectropolarimetric and photometric data. The result is the largest sample of magnetic stars with radio observations that has yet been analyzed: 115 stars with rotational and magnetic constraints, of which 48 are radio-bright. We confirm an obvious dependence of gyrosynchrotron radiation on rotation, and furthermore find that accounting for rotation neatly separates stars with and without detected radio emission. There is a close correlation between Hα emission strength and radio luminosity. We demonstrate that radio emission is explained by the same mechanism responsible for Hα emission from centrifugal magnetospheres, i.e. centrifugal breakout (CBO), where the Hα-emitting magnetosphere probes the cool plasma before breakout, while radio emission is a consequence of electrons accelerated in centrifugally-driven magnetic reconnection. CBO both accurately predicts the onset of detectable emission, and yields a luminosity scaling relationship that matches the observed luminosities with high confidence.

Key words: stars: magnetic field – stars: early type – stars: rotation – radio continuum: stars – magnetic reconnection

1 INTRODUCTION

Approximately 10% of OBA stars possess magnetic fields (Sikora et al. 2019a; Grunhut et al. 2017), with properties

⋆ E-mail: mshultz@udel.edu

that are remarkably consistent across the Hertzsprung-Russell diagram: they are strong (10^2 to 10^4 G; Shultz et al. 2019d); topologically simple (i.e., with only a few exceptions, approximately dipolar; Kochukhov et al. 2019); and stable over at least thousands of rotational cycles (i.e. at least decades; Shultz et al. 2018b). Unlike stars with convective envelopes, for which surface magnetic field strength increases with rotation (Vidotto et al. 2014; Folsom et al. 2016, 2018), there is no such correlation with rotation for the magnetic fields of stars with radiative envelopes (Shultz et al. 2019d; Sikora et al. 2019b). Instead, hot star magnetic fields decline in strength with age in a fashion consistent with conservation of magnetic flux in an expanding atmosphere (for intermediate mass stars; Sikora et al. 2019b) or gradual decay of magnetic flux (for stars above about 5 $M_{\odot}$; Landstreet et al. 2007; Shultz et al. 2019d; Fossati et al. 2016). These properties, together with the absence of a sustainable dynamo mechanism in radiative zones, has led to the interpretation of hot star magnetic fields as 'fossils' left over from a previous epoch, a scenario supported by magnetohydrodynamic (MHD) simulations that have demonstrated the stability of fossil magnetic fields over evolutionary timescales as well as the ability of processes such as binary mergers to generate fossil fields (Braithwaite & Spruit 2004; Braithwaite 2009; Duez et al. 2010; Schneider et al. 2019).

Strong magnetic fields stabilize the atmospheres of hot stars, enabling various chemical elements to accumulate in long-lived surface patches via radiative diffusion (e.g. Michaud et al. 1981; Alecian 2015; Alecian & Stift 2019). This leads directly to modulation of the light curve on rotational timescales (e.g. Krtička et al. 2009, 2012; Krtička et al. 2015), making it straightforward to infer precise rotation periods from photometric time series (e.g. Renson & Catalano 2001). A key goal of the MOBSTER collaboration (Magnetic OB(A) Stars with TESS: probing their Evolutionary and Rotational properties; David-Uraz et al. 2019) is to leverage space photometry from the *TESS* mission in order to dramatically expand the number of known rotational periods for magnetic chemically peculiar stars (e.g. Sikora et al. 2019c), as a means of investigating the evolutionary and magnetospheric characteristics of this population.

The radiation-driven winds of hot stars serve as ion sources which feed their magnetospheres (Landstreet & Borra 1978; Babel & Montmerle 1997; ud-Doula & Owocki 2002). Hot star magnetospheres have a number of observable consequences. They were first detected by Landstreet & Borra (1978) via eclipsing of σ Ori E by the dense plasma clouds of its magnetosphere. Ultraviolet observations demonstrated that the wind-sensitive resonance lines of magnetic hot stars exhibit clear rotational modulation indicating departures from spherical symmetry (e.g. Henrichs et al. 2013). Optical and near-infrared H emission is also formed in the dense plasma of the magnetosphere (Petit et al. 2013; Oksala et al. 2015b). Magnetically confined wind-shocks lead to X-ray emission (Nazé et al. 2014; ud-Doula et al. 2014). Finally, a large fraction of magnetic hot stars show gyrosynchrotron radiation at high frequencies (e.g. Drake et al. 1987) and occasionally auroral radio emission at low frequencies (e.g. Trigilio et al. 2000a; Das et al. 2018).

With the exception of radio diagnostics, magnetospheric emission is believed to be formed within the inner magnetosphere, i.e. the magnetically dominated region within the Alfvén surface, in which the wind kinetic energy density is less than the magnetic energy density. By contrast, radio diagnostics are believed to be a consequence of activity in the middle magnetosphere, a region beyond the Alfvén radius in which magnetically enforced corotation of the plasma with the star breaks down, while the ram pressure of the winds opens the magnetic field lines, the combination of which leads to the formation of a current sheet. Inside the current sheet, electrons are accelerated to relativistic velocities, some of which then return to the star along magnetic fields lines, leading to gyrosynchrotron emission (Trigilio et al. 2004) and, for those that are caught in auroral circuits, electron-cyclotron maser emission (Trigilio et al. 2011; Leto et al. 2016; Das et al. 2020).

Rotation has emerged as a key parameter governing the structure of the inner magnetosphere. In the absence of rotation, inner magnetosphere plasma exists in dynamical equilibrium: flowing up along magnetic field lines, colliding at the magnetic equator, and then being pulled back to the star by gravity (ud-Doula & Owocki 2002). These dynamical magnetospheres are generally detectable in Hα only for stars with high mass-loss rates (i.e. O-type stars; Petit et al. 2013). Due to corotation of the inner magnetosphere plasma, around rapid rotators centrifugal forces can prevent gravitational infall (ud-Doula et al. 2008). This leads to the formation of a centrifugal magnetosphere (CM) between the Kepler corotation radius (the equilibrium point between the gravitational and centrifugal forces) and the Alfvén radius. Within the CM, plasma can accumulate to high enough densities for Hα emission to be detectable even around stars with low mass-loss rates (i.e. B-type stars; Petit et al. 2013; Shultz et al. 2019d). Rotational influence furthermore distorts the plasma distribution, such that (for a tilted dipole) it departs from a torus in the magnetic equator to two distinct clouds located at the intersections of the rotational and magnetic equatorial planes, as described by the Rigidly Rotating Magnetosphere (RRM; Townsend & Owocki 2005) model. In addition to the canonical CM host star σ Ori E (e.g. Landstreet & Borra 1978; Oksala et al. 2015a), the variable Hα profiles of a large number of CM host stars has been examined in detail and found to be phenomenologically consistent with the RRM model (e.g. Leone et al. 2010; Bohlender & Monin 2011; Grunhut et al. 2012; Rivinius et al. 2013; Sikora et al. 2015, 2016; Shultz et al. 2021a), with significant differences so far apparent only in the case of tidally locked binaries (Shultz et al. 2018a).

The current understanding of radio magnetospheres assumes that the inner magnetosphere plasma makes no contribution to the current sheet (Trigilio et al. 2004). Within this framework the only importance of the inner magnetosphere is absorption and diffraction of radio emission due to the denser plasma in this region, and the primary role of rotation is signal modulation due to the changing projection of a tilted dipole on the sky, and a reduced density in the inner magnetospere due to centrifugal stress on the magnetic field. However, Shultz et al. (2020) and Owocki et al. (2020) have recently demonstrated that the Hα emission properties of magnetic early B-type stars can only be ex-

plained if mass-balancing in the CM is accomplished by centrifugal breakout (CBO), rather than steady-state leakage mechanisms operating via a combination of diffusion and drift across magnetic field lines (Owocki & Cranmer 2018). This process, analogous to magnetotail reconnection in planetary magnetospheres, occurs when mass-loading by the wind drives the plasma density beyond the ability of the magnetic field to contain it, at which point the plasma is ejected outwards in a centrifugally driven reconnection process (ud-Doula et al. 2006, 2008). In contrast to previous expectations that this should result in large-scale reorganization of the inner magnetosphere due to emptying of the plasma (e.g. Townsend et al. 2013), observations instead suggest that CBO events happen more or less continuously over small spatial scales, with the CM maintained at a constant state of near-breakout density (Shultz et al. 2020).

Since plasma ejected by CBO must flow away from the star and, therefore, should pass through the middle magnetosphere, it is reasonable to ask whether there might be some connection between gyrosynchrotron emission and rotation. Linsky et al. (1992) searched for just such a connection but were unable to find anything statistically significant. Since then the number of stars with precisely determined rotation periods has dramatically increased. A connection between rotation and gyrosynchrotron emission was suggested by Kurapati et al. (2017), who did not detect radio emission from slow rotators; however, their small sample size prevented firm conclusions. Leto et al. (2021) have recently demonstrated a close connection between rotation and radio luminosity, suggesting that the wind-driven current sheet model advanced by Trigilio et al. (2004) be abandoned in favour of a radiation belt model in which radio emission originates from a magnetic shell unrelated to the middle magnetospheric regions where the magnetic field lines are opened by the wind ram pressure. However, Das & Chandra (2021) have recently reported the detection of correlated flux enhancements emanating via the electron cyclotron maser mechanism from auroral circuits above both magnetic poles of CU Vir, which they interpreted as a possible result of centrifugal breakout events in the inner magnetosphere injecting electrons into both magnetic hemispheres, suggesting that gyrosynchrotron emission may also be connected to CBO.

In the current work we collect together all magnetic stars for which radio observations, magnetic data, and rotational periods have been obtained, both for radio-bright and radio-dim stars (i.e. stars from which radio emission respectively is and is not detected), in order to investigate the influence of rotation in gyrosynchrotron emission from hot star magnetospheres. Literature data are supplemented with unpublished magnetometry, photometry, and radio observations in order to provide the most comprehensive sample of radio emission from magnetic early-type stars that has been analyzed to date. In § 2 the sample and observations are described, together with the determination of atmospheric, fundamental, rotational, and magnetic parameters. The parameter space distributions of radio-bright and -dim stars are examined in § 3, together with comparison to Hα emission, and analysis of correlations between radio luminosities and various parameters. Drawing on this empirical analysis, § 4 develops a theoretical framework for understanding gyrosynchrotron emission in the context of CBO, together with a comparison to observations. In § 5 this framework is compared to previous models and the implications are discussed, while the conclusions are summarized in § 6. Stellar parameters are tabulated in Appendix A. The online appendices B, C, and D respectively provide the observation log of newly presented radio measurements, notes on individual stars for which new magnetic and rotational analyses are presented together with newly published magnetic data, and the tabulated radio flux density measurements for the individual stars.

Table 1. Sources for radio observations.

Source	Number of stars	Wavelength (cm)
Drake et al. (1987)	33	6
Linsky et al. (1992)	42	2, 3.6, 6, 20
Leone et al. (1994)	40	6
Leone et al. (1996)	7	1.3, 2, 6, 20
Leone et al. (2004)	11	0.3
Drake et al. (2006)	19	6
Chandra et al. (2015)	9	20, 50
Kounkel et al. (2017)	2	6
Kurapati et al. (2017)	19	1, 3, 13
Leto et al. (2017)	1	1, 2, 3
Leto et al. (2018)	1	1, 2, 3, 20
Das et al. (2019b)	1	50
Leto et al. (2020a)	1	1, 2, 3, 6
Leto et al. (2020b)	1	2, 3, 6, 13, 20
Pritchard et al. (2021)	5	20
Leto et al. (2021)	1	3
Das & Chandra (2021)	1	50
Drake (priv. comm.)	46	6
Das et al. (submitted)	4	50
This work	10	50

2 SAMPLE

The sample started with all chemically peculiar or magnetic OBA stars which have been observed in at least one radio band. For Ap/Bp stars, we assume them to be magnetic even if magnetic data are not available, as chemical peculiarity of this type is invariably associated with strong surface magnetic fields. For magnetic OB stars (i.e. stars of spectral type B0 and hotter, in which strong winds inhibit the formation of surface chemical abundance spots), only those stars known to be magnetic via spectropolarimetric measurement of the Zeeman effect are included, as chemical peculiarity is not an indicator of magnetism at the top of the main sequence. The sources consulted for radio data are summarized in Table 1. Note that there is considerable overlap in targets between the various surveys; across all papers, 186 unique targets were observed. In addition to literature measurements, we also include new radio measurements of 10 stars (see below).

Since some of the stars observed in the early surveys belong to non-magnetic classes (e.g., classical Be stars, HgMn stars), these stars (33 in total) were removed from the sample. After cross-referencing the catalogues and removing non-magnetic stars, 153 stars have at least one radio frequency observation, 48 of which are detected. These stars are listed in Table A1, with the observed fluxes given online in Table D1. Where more than one observation is available

at a given wavelength, the radio luminosity corresponds to the maximum observed flux density.

2.1 Stellar parameters

We searched the literature for determinations of atmospheric parameters effective temperature $T_{\rm eff}$ and bolometric luminosity $\log L_{\rm bol}$, and projected rotational velocities $v \sin i$. These are given together with references in Table A1. When stellar parameters could not be found in existing compilations or single studies, they were determined photometrically. As a first step, the catalogue was cross-referenced with SIMBAD[1], in order to obtain spectral types and Johnson photometry. Distances were obtained from the Gaia early Data Release 3 Catalogue (Gaia Collaboration et al. 2021); in the few cases where these were not available, *Hipparcos* parallaxes (van Leeuwen 2007) generally were. If Strömgren photometry is available (using the catalogues provided by Hauck & Mermilliod 1998; Paunzen 2015), effective temperatures were determined with the IDL program UVBYBETA (which uses the calibration determined by Napiwotzki et al. 1993). If Strömgren photometry is not available, Johnson photometry was used to obtain the $T_{\rm eff}$. All available de-reddened colours were compared to the empirical calibration provided by Worthey & Lee (2011). Reddening was found using the *Stilism* three-dimensional tomographic dust map (Lallement et al. 2014; Capitanio et al. 2017; Lallement et al. 2018) based on the positions and Gaia distances of the individual stars. While *Stilism* typically extends only out to around 1 kpc, the overwhelming majority of the sample stars are well within this distance; the few stars beyond this distance have stellar parameters available in the literature. Extinctions were determined with the usual reddening law ($A_V = 3.1E(B-V)$). For magnetic chemically peculiar (mCP) stars, the bolometric correction BC determined by Netopil et al. (2008) for mCP stars was used to determine bolometric luminosities $L_{\rm bol}$. Since the Netopil et al. BC is only calibrated up to 19 kK, for mCP stars hotter than this limit a larger uncertainty was adopted following Shultz et al. (2019b). For chemically normal stars, the Nieva (2013) BC was used.

We then searched the literature for determinations of rotational periods $P_{\rm rot}$ and magnetic oblique rotator model (ORM) parameters. In the simplest case of a tilted dipole (appropriate to first order for the vast majority of stars with fossil fields), an ORM consists of an inclination i of the rotational axis from the line of sight, an obliquity angle β of the magnetic axis from the rotational axis, and a polar surface strength $B_{\rm d}$ of the magnetic dipole at the stellar surface. In the simplest case of a tilted dipole, appropriate to the vast majority of stars (e.g. Kochukhov et al. 2019), the rotation of the star will lead to a sinusoidal variation in the longitudinal, or line-of-sight, magnetic field $\langle B_z \rangle$ averaged over the stellar disk. If $P_{\rm rot}$ is known, the $\langle B_z \rangle$ curve can then be used to obtain the ORM parameters (Preston 1967), however there is a degeneracy between the angular parameters i and β. Breaking this degeneracy requires knowledge of $v \sin i$ and the stellar radius R_*.

Where ORM parameters were not already available, we searched for longitudinal magnetic field measurements $\langle B_z \rangle$ with which to determine them. ORM parameters were determined simultaneously with fundamental, rotational, and magnetospheric parameters using the Monte Carlo Hertzsprung-Russell diagram (MCHRD) sampler described by Shultz et al. (2019d). The MCHRD sampler combines all available measurements with evolutionary models in order to infer self-consistent fundamental, ORM, wind, and magnetospheric parameters, automatically accounting for correlated error bars. In this case we utilized the rotating or non-rotating Geneva evolutionary models calculated by Ekström et al. (2012), as appropriate for a given stellar rotational period (non-rotating models were used if $P_{\rm rot} > 10$ d).

2.2 Radio observations

2.2.1 VLA

We report previously unpublished 6 cm observations of 46 stars acquired at the Very Large Array (VLA). The data were acquired in 1992 and 1994 in the context of the survey presented by Drake et al. (1987), Linsky et al. (1992), and Drake et al. (2006), and were reduced and analyzed following the procedures described in those works. All 46 observations are non-detections. One of the stars in this sample, HD 118022, was reanalyzed by Leto et al. (2021) and found to be a detection.

2.2.2 uGMRT

We report new 50 cm radio observations of 10 magnetic hot stars, including 2 new detections (HD 11503 and HD 64740). These data were acquired with the upgraded Giant Metrewave Radio Telescope (uGMRT), located at Pune, India. The uGMRT is a radio interferometer consisting of 30 antennae, and operates over the frequency range of 120–1450 MHz divided into four bands. Our observation frequency corresponds to band 4 (550–900 MHz). For each observation, we observed a set of calibrators in order to calibrate the absolute flux density scale and the bandpass (flux calibrator), and the time-dependent antenna gains (phase calibrator). The details of these observations, including the calibrators used, are provided in Table B1. The data were analyzed using the Common Astronomy Software Applications (CASA, McMullin et al. 2007) following the procedure described in Das et al. (2019b,a). The flux densities are given in Table B1.

These measurements were acquired in the context of an ongoing uGMRT survey aiming to detect and characterize auroral radio pulses emitted via the electron cyclotron maser mechanism (ECM; Das et al. 2018, 2019a,b; Das & Chandra 2021). These pulses occur at or near $\langle B_z \rangle$ nulls (i.e. at phases corresponding to the magnetic equator bisecting the stellar disk) since they are emitted tangent to the auroral circuits above the magnetic poles (e.g. Trigilio et al. 2000b, 2011; Leto et al. 2016; Das et al. 2020). For this reason, observations were acquired close to magnetic nulls, and care is required to ensure that the adopted flux density reflects basal gyrosynchrotron emission rather than the much stronger ECM pulse. For 5 additional stars for which phase coverage

[1] `http://simbad.u-strasbg.fr/simbad/`

was insufficient to cover the basal flux density level, uGMRT data were not included.

It should be noted that, since gyrosynchrotron emission is rotationally modulated and, unlike ECM pulses, is at a minimum rather than a maximum at magnetic nulls (e.g. Leto et al. 2017, 2018), there is the possibility that these data systematically under-estimate the peak 50 cm flux densities of these targets. However, in most cases when observations at other wavelengths are available, the measurements are comparable, consistent with expectations that the radio spectrum is approximately flat and that rotational modulation of the flux density is generally only a factor of a few (e.g. Trigilio et al. 2004; Leto et al. 2012, 2017, 2018, 2020a).

2.3 Spectropolarimetric and photometric observations

When neither ORM parameters nor published $\langle B_z \rangle$ measurements were available, or when rotation periods were unknown, we utilized both public and private archives of spectropolarimetric and space photometric data with which to constrain magnetic and rotational properties. These were then used in conjunction with stellar parameters and the MCHRD sampler to infer ORM models as described above. The data used for this analysis are described in detail in Appendix C. In total, we provide new magnetic data for 30 stars, of which magnetic fields were detected in 16, and utilized magnetic and/or photometric data to evaluate rotational periods for 59 stars, of which we refined the published periods of 14 stars and determined new periods for 16 stars. In some cases (HD 36629, HD 37041, HD 49606, and HD 89822), these analyses also led to the rejection of published rotational periods and magnetic data as spurious results arising from noisy data; these stars were removed from the sample.

2.3.1 Dominion Astrophysical Observatory spectropolarimetry

The dimaPol spectropolarimeter is a medium-resolution ($\lambda/\Delta\lambda \sim 10,000$) instrument covering the 25 nm region centred on the laboratory wavelength of the Hβ line. It is mounted on the 1.8 m Dominion Astrophysical Observatory (DAO) Plaskett Telescope. The instrument and reduction pipeline are described in detail by Monin et al. (2012). Magnetic measurements are obtained primarily using the wings of Hβ and are therefore fairly insensitive to either $v \sin i$ or surface chemical abundance patches (e.g. Borra & Landstreet 1977).

Unpublished DAO measurements are available for 16 stars in the sample, although in some cases no magnetic field can be detected at the available precision (generally hundreds of G). Of the 12 stars for which a magnetic field can certainly be detected and good constraints do not already exist, 217 individual measurements are available, with a median of 18 measurements per star. These data are provided in Appendix C.

2.3.2 ESPaDOnS and Narval spectropolarimetry

ESPaDOnS (Echelle SPectropolarimetric Device for the Observations of Stars) and Narval are identical high-resolution ($\lambda/\Delta\lambda$) spectropolarimeters respectively mounted at the 3.6 m Canada-France-Hawaii Telescope (CFHT) and the 2 m Bernard Lyot Telescope (TBL). They cover a wavelength rang of approximately 370 nm to 1050 nm across 40 overlapping spectral orders. Each observation consists of 4 differently polarized subexposures, yielding for unpolarized (Stokes I) spectra, one circularly polarized (Stokes V) spectrum, and two diagnostic null (N) spectra with which to check for normal instrument operation and determination of noise. The characteristics of the instruments and data reduction were described in detail by Wade et al. (2016).

We queried the PolarBase database of Narval and ESPaDOnS spectropolarimetry for unpublished spectropolarimetric measurements (Petit et al. 2014). These were found for 20 stars (overlapping with the DAO dataset), of which magnetic fields were detected via the multiline least-squares deconvolution (LSD; Donati et al. 1997; Kochukhov et al. 2010) method in 6. The magnetic analysis of these measurements is described in Appendix C.

2.3.3 Space photometry

The surface abundance spots of magnetic chemically peculiar stars lead to photometric variability that can be used to infer their rotational periods. We searched public archives (the *Hipparcos* archive and MAST, the Mikulsi Archive for Space Telscopes) for the light curves from the High precision parallax collecting satellite (*Hipparcos*), *Kepler*, and Transiting Exoplanet Survey Satellite (*TESS*) space telescopes. These light curves are provided in Appendix C. Period analysis was performed using the Lomb-Scargle program PERIOD04 (Lenz & Breger 2005). This was accomplished by identifying the lowest-frequency term in a harmonic series, fixing higher harmonics to whole number multiples of the rotational harmonic, and then optimizing the phases and amplitudes of the terms to minimize residuals, as is standard practice for the strictly periodic rotational variability of mCP stars (e.g. David-Uraz et al. 2019; Sikora et al. 2019c).

Hipparcos was an astrometric space telescope, whose mission lasted from 1989 to 1993. While the primary aim was to obtain high-precision trigonometric parallaxes, it also obtained time series photometry for a large number of stars (Perryman et al. 1997; van Leeuwen 2007), which is available for 12 stars without published rotation periods.

The NASA *Kepler* satellite was a μmag-precision space photometer with a 110 square degree field of view operating in the 400 to 850 nm bandpass, intended for high-cadence, long-duration observations with the goal of detecting transiting exoplanets (Borucki et al. 2010). The *K2* mission was an extension of the original *Kepler* mission, following the failure of two of the satellite's reaction wheels; by utilizing pressure from the solar wind, the satellite could be stabilized on a given field of view for about 3 months, enabling it to observe fields along the ecliptic (Howell et al. 2014). A *K2* light curve is available for 1 star.

TESS uses four cameras with a total field of view of $24^\circ \times 96^\circ$, with a bandpass covering 600 to 1050 nm (Ricker et al. 2015). The initial two-year TESS mission be-

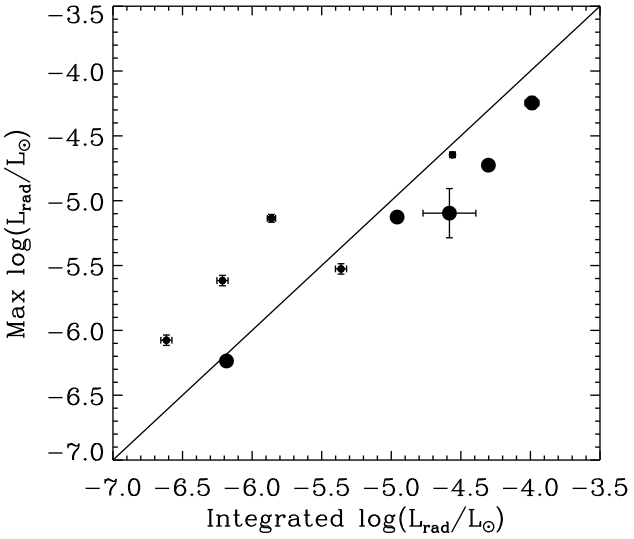

Figure 1. Radio luminosities inferred from the maximum flux density vs. radio luminosities obtained by integrating flux density across the full frequency range, for those stars with observations sampling at least 4 frequencies. Symbol size is proportional to number of observations (either 4, small, or 5, large).

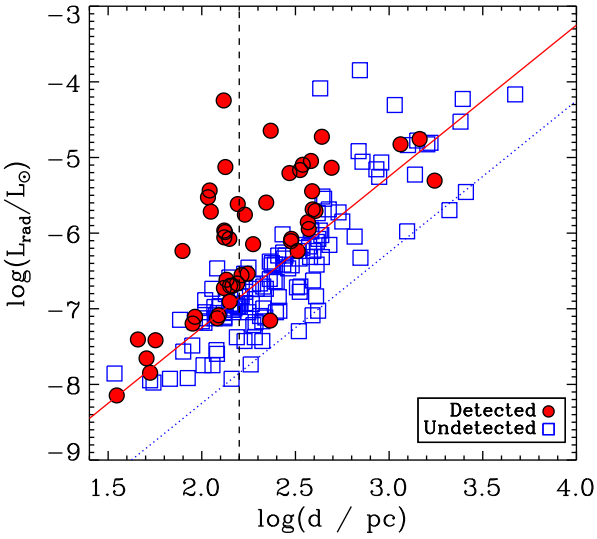

Figure 2. Radio luminosity as a function of a distance. Solid and dotted lines indicate distance-dependent detection limits as defined by the lower bounds of detected and non-detected stars, respectively. The vertical dashed line indicates the distance beyond which the lower detection limit begins to rise with increasing distance. Non-detections are upper limits.

gan in 2018, during which it completed coverage of almost the entire sky. During each year, 13 sectors were observed for 27 days each, with a nominal precision of 60 ppm hr^{-1} (although this varies between fields and targets). High-priority targets are observed with a two-minute cadence, and the processed light curves made available on the MAST archive immediately following reduction. Two-minute cadence TESS data are available for 9 stars. In other cases, we used the 30-minute cadence data extracted from Full Frame Images, obtained from MAST when available or, for 9 stars for which this was not the case, extracted ourselves. In total we utilized *TESS* data for 46 stars.

2.4 Final sample

In the end, magnetic data are available for 139 stars, rotational periods for 132 stars, and both for 116 stars, of which 48 have detected radio emission. Dipolar magnetic field strengths and rotation periods are given together with references in Table A1. In the cases in which ORM parameters were determined here using published $\langle B_z \rangle$ measurements, the references to the measurements are also included.

Radio luminosities were determined using parallax distances. When multiple radio measurements are available, the highest flux density measurement was chosen as representative of the radio luminosity of the star. When they have been measured, the spectral indices of radio emission from magnetic hot stars are approximately flat between 1 and 100 GHz (as has been shown by Leto et al. 2021, for the largest sample to date of stars with a sufficient number of multifrequency observations to perform this analysis), and the difference between measurements at different frequencies for a given star in the present sample is in general small. It is therefore likely that radio luminosities can be estimated with reasonable accuracy from single observations at a single frequency (which are all that are available for much of the sample). Following this, radio luminosity was determined by integrating a box function between 600 MHz and 30 GHz (i.e., 50 cm to 1 cm), scaled by the peak specific intensity measured across all observations (when more than one observation is available). In the end, 0.3 cm measurements were discarded as likely outliers due to significant discrepancies between these and observations at other wavelengths for the same stars. While this is a less-than-perfect approximation of the actual spectral energy distributions (SEDs) of the sample stars, in the absence of multi-wavelength measurements constraining the variation of SEDs across stellar parameters it is not yet possible to adopt a more sophisticated approach. Furthermore, rotational modulation of the signal and the reliance on snapshot observations makes it likely that the maximum flux density is under-estimated for much of the sample, for which this box function approach may partially compensate given that it may over-estimate the radio luminosity by failing to account for deparatures from perfectly flat spectral indices. As a check on this approximation, Fig. 1 shows the radio luminosity inferred from the maximum flux density, vs. the radio luminosity measured via integration of measured flux densities across the same frequency range, for those stars with observations sampling at least 4 frequencies. While there are outliers by up to about 1 dex, there is generally a good correlation between the two quantities, suggesting this approach is a reasonable approximation of the actual radio luminosities of the sample.

As can be seen in Fig. 2, radio luminosity varies over about 4 orders of magnitude. While radio emission is rotationally modulated, the amplitude of this modulation is a factor of a few (e.g. Trigilio et al. 2004; Leto et al. 2012, 2017, 2018), i.e. much smaller than the differences between

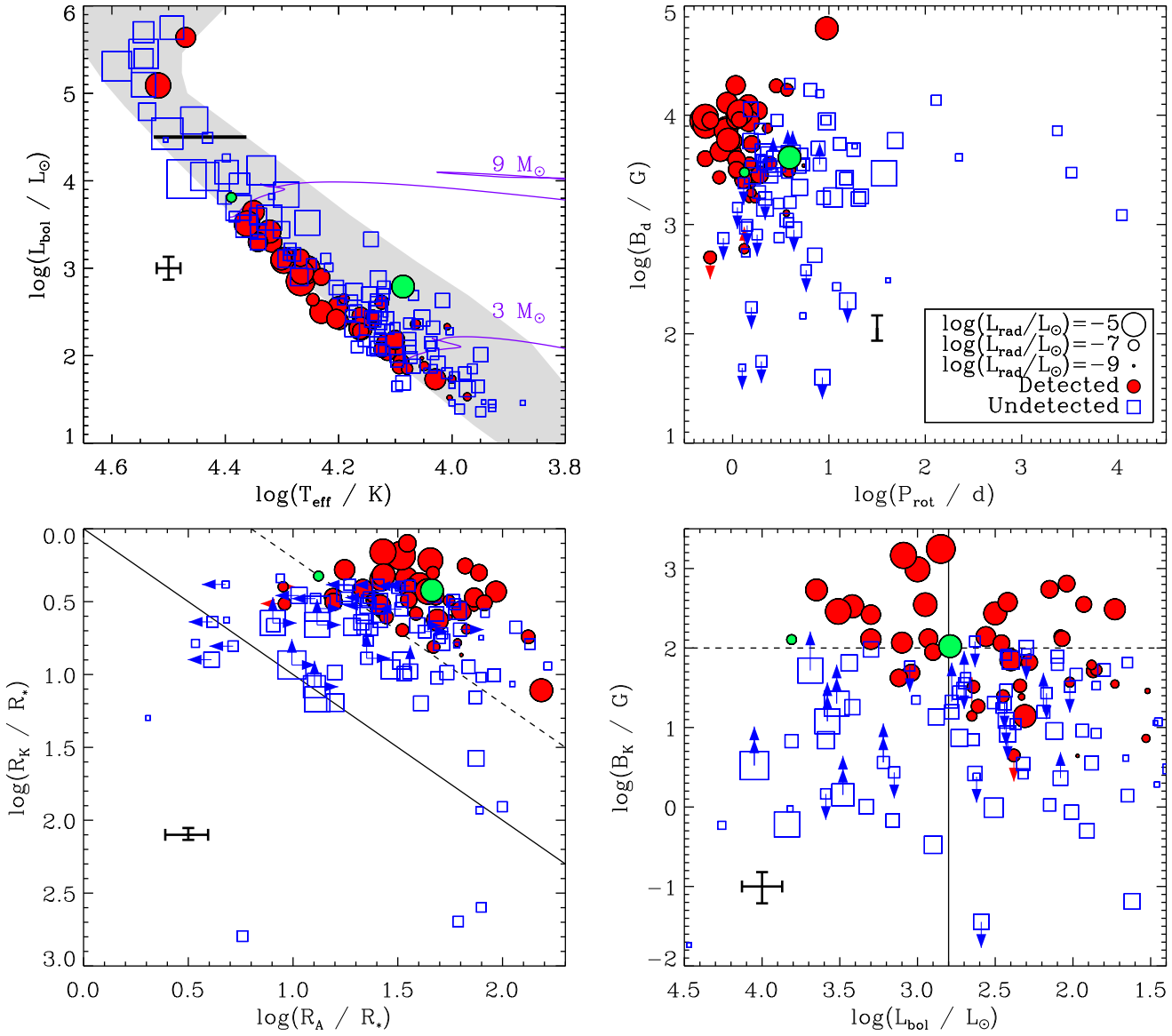

Figure 3. Parameter space distribution of the sample. Filled red circles indicate radio-bright stars, open blue squares radio-dim stars, and symbol size is proportional to radio luminosity (or its upper limit). Mean uncertainties are indicated by error bars. Filled green circles highlight HD 64740 and HD 171247 (discussed in the text). *Top Left*: Hertzsprung-Russell diagram showing all magnetic stars with radio observations. The grey shaded region indicates the main sequence. The thick line indicates the empirical bolometric luminosity cutoff applied to the subsequent analysis. *Top right*: the sample on the $\log B_{\rm d} - \log P_{\rm rot}$ plane. *Bottom left*: the sample on the rotation-magnetic wind confinement diagram. The solid line indicates $R_{\rm A} = R_{\rm K}$: points below have dynamical magnetospheres only, points above possess centrifugal magnetospheres. The dashed line shows $\log R_{\rm A}/R_{\rm K} = 0.8$, the approximate minimum threshold for Hα emission. *Bottom right*: the $\log B_{\rm K} - \log L_{\rm bol}$ plane. The minimum value of $\log B_{\rm K}$ extends to about -6; none of the stars not shown are detected in radio. The dashed line indicates the approximate $B_{\rm K}$ threshold for Hα emission, while the solid line indicates the lower luminosity limit for Hα.

individual stars in the sample. That radio observations sampling the entire phase curve are in general unavailable, and that the true peak luminosity is therefore unknown, is unimportant at the level of the full population.

Another consideration that is apparent from Fig. 2 is that the detection limit is a function of distance. However, below a distance of $\log(d/{\rm pc}) = 2.2$, the lower detection limit is fairly constant, with radio non-detections being comparable in luminosity to the weakest radio detections. Beyond this distance, it is more likely that radio-dim stars would have been detected if they were closer; below it, this scenario is less likely. This sub-sample is therefore in a sense more complete than the full sample, and can be used to test conclusions derived from the full sample of stars.

3 PARAMETER STUDY

We begin our analysis by examining the distributions of radio-bright and radio-dim stars in atmospheric, magnetic,

rotational, and magnetospheric parameter space, examining the effectiveness of each parameter in separating the two populations, as well as the strength of the correlation between radio luminosity and a given parameter.

3.1 Hertzsprung-Russell diagram

The top left panel of Fig. 3 shows all magnetic stars with radio observations on the Hertzsprung-Russell diagram (HRD). Most radio-bright stars are between about 3 and 9 $M_\odot$, and are generally close to the Zero-Age Main Sequence (ZAMS), where we have shown the non-rotating evolutionary models calculated with the solar metallicity Geneva evolutionary code by Ekström et al. (2012). They are relatively evenly distributed within this mass range, with no obvious tendency to cluster at high luminosities, consistent with the finding from Leto et al. (2021) that gyrosynchrotron emission is more or less independent of the wind power.

As discussd by Chandra et al. (2015), the strong winds of O-type stars lead to radio photospheres that are, in general, much larger than their Alfvén radii, and swallow any gyrosynchrotron emission that might be produced. Thermal radio emission from O-type stars can be produced by their winds (e.g. Bieging et al. 1989; Lamers & Leitherer 1993), and while this can in principle be rotationally modulated due to symmetry-breaking in the presence of a magnetic field (Daley-Yates et al. 2019), this is unrelated to the gyrosynchrotron emission of interest here. Furthermore, non-thermal synchrotron emission can be produced in the colliding wind shocks of close binaries (e.g. Pittard et al. 2006; Blomme et al. 2010). Only two O-type stars are detected in the sample (Kurapati et al. 2017), these being ζ Ori A (which has a thermal radio spectrum) and Plaskett's Star (a spectroscopic binary; Linder et al. 2008). O-type stars were therefore excluded from the sample, as indicated by the horizontal thick bar in Fig. 3. This removed 11 stars from the sample.

3.2 Rotation and magnetic field strength

The top right panel of Fig. 3 shows the sample on the $\log B_{\rm d} - \log P_{\rm rot}$ plane. The period axis is truncated for clarity, omitting three stars with periods on the order of several years, none of which are detected in the radio. Notably, all radio-bright stars are both strongly magnetic (as expected) as well as being rapid rotators ($P_{\rm rot} \lesssim 5$ d, with Babcock's Star, HD 215441, the only exception – a 'slow' rotator with a period of about 10 d).

Comparing radio-dim and radio-bright stars, their rotational and magnetic properties are clearly different. The mean rotational period and surface magnetic dipole strengths of the radio emitters are $\log\left(P_{\rm rot/d}\right) = 0.14^{+0.23}_{-0.14}$ and $\log\left(B_{\rm d}/{\rm G}\right) = 3.70^{+0.23}_{-0.25}$, while the corresponding means for the radio-dim stars are $\log\left(P_{\rm rot/d}\right) = 0.81^{+0.87}_{-0.22}$ and $\log\left(B_{\rm d}/{\rm G}\right) = 3.31^{+0.24}_{-0.49}$, where the error bars correspond to standard deviations above and below the mean. Notably, radio emission is not detected in any star with $\log P_{\rm rot} > 1$, regardless of magnetic field strength.

3.3 The rotation-magnetic wind confinement diagram

The bottom left panel of Fig. 3 shows the sample on the rotation-magnetic wind confinement diagram (introduced as a fundamental plane of magnetospheres by Petit et al. 2013). The vertical axis shows the Kepler corotation radius $R_{\rm K}/R_* = W^{-2/3}$, where the critical rotation parameter W is given by the ratio of the equatorial velocity $v_{\rm eq}$ to the orbital velocity $v_{\rm orb}$ necessary to maintain a Keplerian orbit at the stellar equator (ud-Doula et al. 2008):

$$W = \frac{v_{\rm rot}}{v_{\rm orb}} = \frac{2\pi R_*}{P_{\rm rot}} \left(\frac{GM_*}{R_*}\right)^{-1/2}, \qquad (1)$$

where R_* and M_* are the stellar radius and mass, and G is the gravitational constant. The Kepler radius corresponds to the distance from the star at which gravity and the centrifugal force due to magnetically enforced corotation are in balance, and therefore decreases (moves closer to the stellar surface) with increasing rotational velocity.

The horizontal axis of the bottom left panel of Fig. 3 shows the Alfvén radius $R_{\rm A}$, i.e. the distance from the star at which the wind ram pressure and magnetic pressure equalize. The Alfvén radius was determined from the wind magnetic confinement parameter η_* as $R_{\rm A}/R_* = 0.3 + (\eta_* + 0.25)^{1/4}$, where η_* is the ratio of the magnetic energy to the wind kinetic energy given by ud-Doula & Owocki (2002):

$$\eta_* = \frac{B_{\rm eq}^2 R_*^2}{\dot{M} v_\infty}, \qquad (2)$$

with $B_{\rm eq} = B_{\rm d}/2$ the surface magnetic field strength at the magnetic equator, $\dot{M}$ the mass-loss rate in the absence of a magnetic field (i.e., the surface mass flux), and $\rm v_\infty$ the wind terminal velocity. For mass-loss we adopted the usual Castor, Abbott & Klein (1975, CAK) scaling formula,

$$\dot{M} = \frac{\alpha}{1-\alpha} \frac{L_{\rm bol}}{c^2} \left(\frac{\bar{Q}\Gamma_e}{1-\Gamma_e}\right)^{-1+1/\alpha} \sim L_{\rm bol}^{1/\alpha}, \qquad (3)$$

where $\bar{Q} \approx 1000$ (Gayley 1995), c is the speed of light, and the electron Eddington parameter scales as $\Gamma_e = \kappa_e L_{\rm bol}/(4\pi G M_* c)$ for electron opacity κ_e. The effective CAK exponent can range from $\alpha \approx 1/2$ to $\alpha \approx 2/3$, with $\alpha \approx 0.55$ applicable for the magnetic B-stars considered here (see e.g. Petit et al. 2013). We used CAK mass-loss in preference to the B-star mass-loss rates developed by Krtička (2014) because the latter are effectively zero for stars below about 14 kK for the default solar metallicity[2]. Wind terminal velocities were scaled with the escape speed $v_{\rm esc}$

$$v_{\rm esc} = \left(\frac{2GM_*(1-\Gamma_e)}{R*}\right)^{1/2}, \qquad (4)$$

where we adopted a scaling factor f, such that $v_\infty = f v_{\rm esc}$, where $f = 1.3$ and 2.6 on either side of the bistability jump at 25 kK (Vink et al. 2000, 2001). We did not, however, adopt an abrupt change in $\dot{M}$ across the bistability jump

[2] While essentially all of these stars are chemically peculiar, detailed mean surface abundances are not generally available.

as, in contrast to the change in v_∞ which is observationally motivated (Lamers et al. 1995), the predicted change in $\dot{M}$ has not been confirmed (Markova & Puls 2008).

If $R_K > R_A$ the inner magnetosphere is purely dynamical, meaning that rotation plays no role; no stars in this regime show radio emission. When $R_K < R_A$ the inner magnetosphere forms a centrifugal component. The dashed line indicates $\log(R_A/R_K) = 0.8$, the approximate threshold for Hα emission (Petit et al. 2013; Shultz et al. 2019d). Essentially all of the radio-bright stars are above this threshold, once again indicating that rotation plays a crucial role. It is also noteworthy that radio and Hα emission occur in the same part of the rotation-magnetic confinement diagram. Furthermore, while there are relatively few stars in the DM-only regime with radio observation, there are numerous stars in the small-CM regime ($0 < \log(R_A/R_K) < 0.8$), all but two of which are not detected in the radio (with the two detected stars having limiting values of B_d). Since it seems to be necessary for a star to have a large CM for it to display gyrosynchrotron emission, it also seems unlikely that additional observations will detect DM stars with non-thermal radio (although this should naturally be checked in the future).

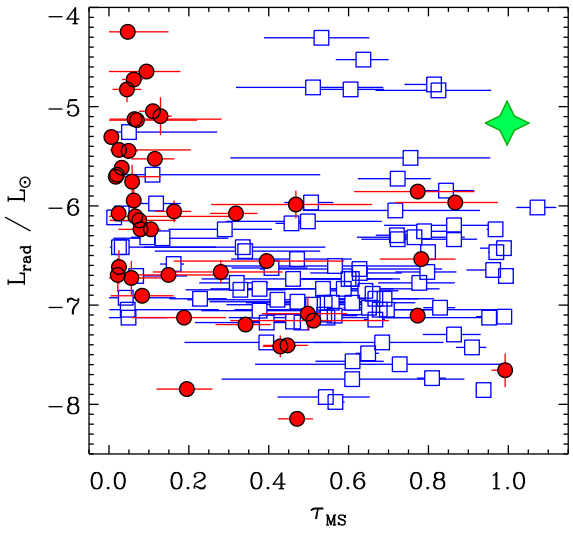

Figure 4. Radio luminosity as a function of fractional main sequence age τ_{MS}. HD 171247 is highlighted with a green star.

3.4 Magnetic field at the Kepler radius

Shultz et al. (2020) showed that Hα emission is regulated directly by the strength of the magnetic field at the Kepler radius in the magnetic equatorial plane, which for a dipole is $B_K = B_{eq}/R_K^3$, for R_K in units of stellar radii. Hα emission appears only in stars with $B_K \sim 100$ G. As demonstrated by Owocki et al. (2020), this is the magnetic field strength necessary for the plasma density at R_K to reach an Hα optical depth of unity, under the assumption that mass balancing is governed by centrifugal breakout.

The bottom right panel of Fig. 3 shows the sample on the $\log B_K - \log L_{bol}$ plane (compare to the right panel of Fig. 3 in Shultz et al. 2020). The dashed line indicates the Hα emission threshold; essentially all stars above this threshold are radio-bright. The vertical line indicates the low-luminosity cutoff for Hα emission; notably, radio emission extends to lower luminosities, including essentially the entire B-type spectral sequence. Gyrosynchrotron emission is also seen at lower values of B_K than those at which Hα can be detected, down to about 10 G.

3.5 Evolution of radio luminosity

As is apparent from the HRD in Fig. 3, the majority of radio-bright stars are found close to the ZAMS. Fig. 4 shows radio luminosity as a function of fractional main sequence age τ_{MS}, and demonstrates that radio luminosity drops precipitously by about 2 dex beyond a fractional main-sequence age of $\tau_{MS} \sim 0.2$. The stars with the weakest radio emission are furthermore found in the second half of the main sequence. This is just as would be expected if radio emission is tied to rotation, since magnetic braking rapidly removes angular momentum (ud-Doula et al. 2009; Keszthelyi et al. 2019, 2020). A similar phenomenon has been seen in the Hα magnetospheres of early B-type stars: emission is found only in young stars (Shultz et al. 2019d), and drops in strength steeply with age (Shultz et al. 2020).

The one exception to this trend is HD 171247, highlighted in Fig. 3 with a large green circle and in Fig. 4 with a green star. This is a somewhat curious object as its radio luminosity is relatively high ($\log L_{rad} = -5.16 \pm 0.02$) despite being a relatively slow rotator ($P_{rot} = 3.9$ d) with a surface magnetic field of average strength ($B_d \sim 4.1$ kG). Furthermore, in contrast to the general case in which radio-bright stars are found close to the ZAMS, HD 171247 is apparently a fairly evolved object very near to the terminal age main sequence. As described in the Appendix, there is considerable uncertainty regarding HD 171247's rotational period, as strikingly different values (about 1 d vs. 4 d) are found from $\langle B_z \rangle$ and photometry.

It is possible that HD 171247 is affected by some other factor. For example, an undetected binary companion might lead to an overestimated bolometric luminosity or, in the case of an interacting system, enhance its radio luminosity; however, there is nothing particularly strange about the measurements from the well-studied binary systems HD 36485 or HD 37017 (Leone et al. 2010; Bolton et al. 1998), and there is furthermore no indication of asymmetry or radial velocity variability in the available DAO spectra. The star does, however, have a substellar companion of approximately 46 Jupiter masses at a separation of about 2 AU, detected via *Gaia* astrometry (Kervella et al. 2019); if the companion is also magnetic, it may be an additional source of radio emission. Alternatively, its reported radio flux density measurement might have been obtained at a rotational phase corresponding to an auroral radio emission pulse, which can result in substantial enhancements over the basal flux (while its 6 cm observations are not in the usual wavelength regime for this phenomenon, which is predominantly seen at longer wavelengths, ECM was detected at this wavelength by Das & Chandra 2021, in the case of HD 124224). Given HD 171247's anomalous position on the HRD, and the uncertainty in its rotational period, this ob-

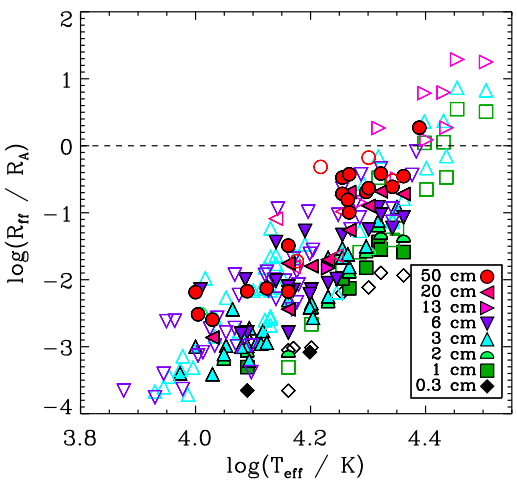

Figure 5. Ratio between the radius of the free-free emission photosphere $R_{\rm ff}$ and the Alfvén radius $R_{\rm A}$ as a function of $T_{\rm eff}$. Symbol colour and type indicates wavelength; filled symbols correspond to radio-bright stars. Above the dashed line, the radio photosphere is larger than $R_{\rm A}$ for the given frequency. Only one radio-bright star, HD 64740, is above the dashed line.

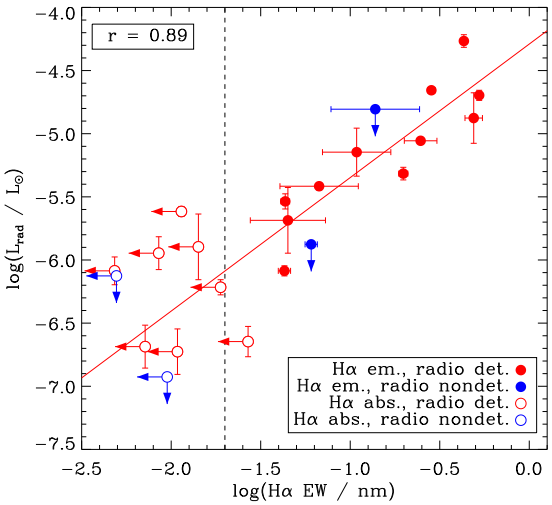

Figure 6. Radio luminosity as a function of Hα emission equivalent width. The solid diagonal line shows a fit to the measurements of stars detected in both Hα and radio. The vertical dashed line indicates the approximate noise floor identified by Shultz et al. (2020). Red and blue points are stars detected and not detected in the radio; filled and open symbols are stars with Hα in emission and absorption.

ject was removed from the subsequent analysis as likely suffering from one or more systematic errors.

3.6 Wind absorption

To determine to what degree the remaining sample might still be affected by wind absorption, following Chandra et al. (2015) we calculated the ratio between the radius of free-free emission $R_{\rm ff}$ and $R_{\rm A}$, where $R_{\rm ff}$ gives the extent of the radio photosphere at a given frequency. If $R_{\rm ff} > R_{\rm A}$, it is likely that gyrosynchrotron emission will be absorbed by the wind, and any radio emission detected from the source will arise from free-free emission in the wind. Fig. 5 shows $R_{\rm ff}/R_{\rm A}$ as a function of $T_{\rm eff}$. Since $R_{\rm ff}$ is a strong function of wavelength, this analysis was done for observations at specific wavelengths rather than integrated values. As can be seen in Fig. 5, for all but one radio-bright star $R_{\rm ff} \ll R_{\rm A}$. The sole exception is HD 64740, which is the hottest and most luminous of the radio-bright stars remaining in the sample after removing the O-type stars, and the only radio-bright B-type star with a mass above 9 $M_\odot$. This star is highlighted in Fig. 3 by a small green circle. HD 64740 has a relatively low radio luminosity, $\log L_{\rm rad}/L_\odot = -7.16 \pm 0.06$, and was subsequently found to be under-luminous in comparison to stars with similar rotational, magnetic, and stellar parameters. Following Kurapati et al. (2017)'s Eqn. 1, the minimum mass-loss rate that could explain the star's radio luminosity via free-free emission is $\sim 2 \times 10^{-7}$ M$_\odot$ yr^{-1}, which is about 100 times higher than the star's CAK mass-loss rate, indicating that the radio emission cannot be due to free-free emission from the wind. While HD 64740's radio emission is therefore almost certainly gyrosynchrotron, it seems probable that the sole 50 cm observation of this star is strongly attenuated by self-absorption in the wind, and it was therefore removed from the subsequent analysis.

3.7 Comparison to Hα emission

The co-occurence of radio-bright and Hα-bright stars in the same part of the rotation-magnetic confinement diagram (see Fig. 3) is suggestive of a relationship between the two forms of magnetospheric emission. Fig. 6 demonstrates that the two forms of emission do in fact correlate. Hα emission equivalent widths (EWs) were taken from the measurements of Shultz et al. (2020), with the addition of measurements of HD 156424 (Shultz et al. 2021b), ALS 9522 (Shultz et al. 2021a), and HD 147932 (Shultz et al., in prep.). For stars in which both gyrosynchrotron emission and Hα emission are detected, Pearson's correlation coefficient is $r = 0.89$.

Stars without Hα emission (open symbols) are of course all at or below the noise level (dashed line) inferred from the median EW error bar. Furthermore, the radio luminosities of these stars are systematically lower than those of stars with Hα emission, consistent with magnetic confinement in their CMs being too weak to contain plasma that is optically thick in Hα. Only two stars have Hα emission but are not detected in radio; in these cases, the upper limits on their radio luminosities lie very close to the regression line.

3.8 Regression analysis

In order to identify the primary parameters affecting radio emission in a relatively hypothesis-independent fashion, we compared radio luminosities to a variety of stellar, magnetic, and rotational parameters, using one-, two-, and three-variable regressions (regressions with four variables yielded no statistical improvement). The results of these tests are summarized in Table 2. The best regressions are shown in Fig. 7.

The particular quantities chosen for regression analysis are: the bolometric luminosity $L_{\rm bol}$; the effective temper-

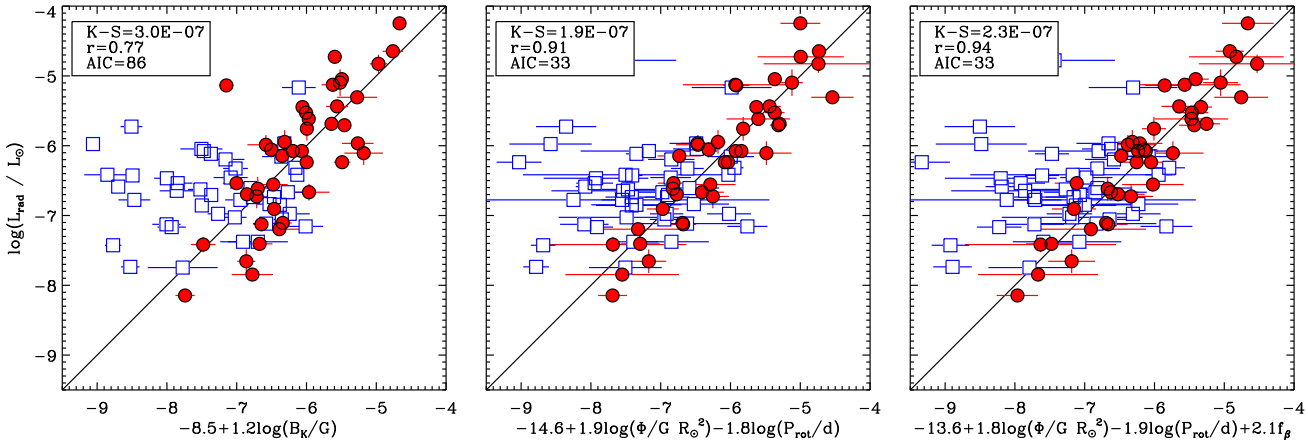

Figure 7. Best results for (*left* – *right*) single-, double-, and triple-variable regressions of various parameters vs. radio luminosity. Red circles show radio-bright stars; open squares are upper limits for radio-dim stars. Legends give the K-S probability for separating radio-bright and -dim stars into different populations; Pearson's r; and the Akaike Information Criterion (AIC).

Table 2. Regression parameters for maximum radio luminosity. From left to right, the columns give: the tested variable; the two-sample K-S test probability that the variable separates radio-bright and -dim stars into separate populations; Pearson's correlation coefficient r; the reduced χ^2 of the regression; the Akaike Information Criterion (AIC) for the regression; and the slope of the regression.

Variable	K-S	r	χ^2/ν	AIC	Slope
One-Variable Regressions					
$\log(L_{\rm bol}/{\rm L}_\odot)$	0.65	0.68	191	99	1.1±0.2
$\log(T_{\rm eff}/{\rm K})$	0.77	0.75	154	83	6.7±0.9
$\log(R_*/{\rm R}_\odot)$	0.05	0.23	249	124	2.0±1.3
$\log(M_*/{\rm M}_\odot)$	0.43	0.73	156	84	4.4±0.7
$\log(P_{\rm rot}/{\rm d})$	10^{-8}	-0.53	261	129	-1.7±0.4
$\log(B_{\rm d}/{\rm G})$	10^{-2}	0.60	131	73	1.6±0.3
$\log(\dot{M}/{\rm M}_\odot\ {\rm yr}^{-1})$	0.82	0.56	194	100	0.6±0.2
$\log(R_{\rm A}/R_*)$	0.02	-0.18	242	121	-0.7±0.6
$\log(R_{\rm K}/R_*)$	10^{-5}	-0.47	243	122	-2.1±0.7
$\log(R_{\rm A}/R_{\rm K})$	0.15	-0.28	237	119	-0.7±0.4
$\log(B_{\rm K}/G)$	10^{-7}	0.77	162	86	1.2±0.2
$\log(\Phi/{\rm G\ R}_\odot^2)$	0.23	0.71	139	76	1.8±0.3
$\log f_\beta$	0.21	0.34	287	141	3.0±1.4
Best Two-Variable Regression					
$\log(\Phi/{\rm G\ R}_\odot^2)$	10^{-7}	0.91	36	34	1.9±0.2
$\log(P_{\rm rot}/{\rm d})$					-1.8±0.2
Best Three-Variable Regression					
$\log(\Phi/{\rm G\ R}_\odot^2)$	10^{-7}	0.94	30	34	1.8±0.2
$\log(P_{\rm rot}/{\rm d})$					-1.9±0.2
f_β					2.1±0.5

ature $T_{\rm eff}$; the stellar radius R_*; the stellar mass M_*; the rotation period $P_{\rm rot}$; the surface magnetic dipole strength $B_{\rm d}$; the mass-loss rate $\dot{M}$; the Alfvén radius $R_{\rm A}$; the Kepler radius $R_{\rm K}$; the dimensionless size of the CM $\log(R_{\rm A}/R_{\rm K})$; the strength of the equatorial magnetic field at the Kepler radius $B_{\rm K}$; the unsigned magnetic flux $\Phi = B_{\rm d}R_*^2$; and as a test of the dependence on the geometry of the magnetic field, $f_\beta = (1+\cos\beta)/2$, where β is the obliquity angle of the magnetic axis from the rotational axis. The inclusion of the geometric parameter f_β is motivated by the RRM model, since at higher β the amount of plasma retained in the CM is reduced (Townsend & Owocki 2005).

Each parameter was tested in several ways. First, the two-sample Kolmogorov-Smirnov test was used to compare the distributions of stars with and without detected radio emission, in order to determine if the parameter or combination of parameters effectively separates the two populations. Second, for the radio-bright stars, Pearson's correlation coefficient r was calculated for each parameter or set of parameters, where r values close to ±1 indicate a strong correlation, and values close to 0 no correlation. Third, the reduced χ^2/ν (where ν is the number of degrees of freedom) was calculated, in order to estimate the quality of the fit of the linear regression to the data. Finally, the Akaike Information Criterion (AIC) was calculated, which provides a relative estimator of the quality of a given model based upon the fit and the number of variables (a lower value indicating a superior fit despite additional model parameters). Since adding additional parameters to a regression will naturally improve the fit to the data, χ^2/ν and AIC help to determine whether the improvement is a meaningfully better fit, or simply a consequence of the additional degrees of freedom. In calculating χ^2/ν and the AIC, we used the uncertainties in the radio luminosities, rather than also including the uncertainties in the tested parameters, since the latter are widely variable between parameters (e.g., on the order of 10% or higher in $B_{\rm d}$, as compared to around 0.0001% in $P_{\rm rot}$), and including these uncertainties results in the goodness-of-fit tests simply reflecting the parameter uncertainties, making meaningful comparison difficult.

For one-variable regressions, stellar parameters ($T_{\rm eff}$, $\log L_{\rm bol}$, R_*, M_*, $\dot{M}$) have large K-S probabilities, indicating that they do not separate the radio-bright and -dim populations. However, r is relatively high for $T_{\rm eff}$, $\log L_{\rm bol}$, and M_*, indicating that stellar parameters play some role. By contrast, parameters associated with the magnetic field or rotation achieve K-S probabilities close to 0, indicating that they do a good job of distinguishing between radio-bright and -dim stars, with parameters involving rotation ($P_{\rm rot}$, $R_{\rm K}$, $B_{\rm K}$) achieving the smallest K-S probabilities. Interest-

ingly, the correlation coefficients associated with $B_{\rm d}$ and $P_{\rm rot}$ are lower than those achieved for some stellar parameters. The highest r is achieved for $B_{\rm K}$, while Φ gives the smallest AIC.

The one-variable results indicate that radio emission is primarily an effect of magnetic field strength and rotation, however they also point to at least some role for stellar parameters. With the addition of a second variable, the best $r = 0.91$ and AIC = 34 is provided by $L_{\rm rad} \propto \Phi^{1.9\pm0.2} P_{\rm rot}^{-1.8\pm0.2}$, which also yields a very small K-S probability. Adding a third variable yields the best $r = 0.94$ for $L_{\rm rad} \propto \Phi^{1.8\pm0.2} P_{\rm rot}^{-1.9\pm0.2} f_\beta^{2.1\pm0.5}$, with the AIC unchanged from the best two-variable result.

The overall results favour a strong dependence of radio luminosity on surface magnetic field strength, rotational period, and the size of the star, with a possible residual dependence on the magnetic geometry. The overall basic best-fit regression seems to go as $L_{\rm rad} \propto (\Phi/P_{\rm rot})^2 = (B_{\rm d} R_*^2/P_{\rm rot})^2$. This confirms the basic result found by Leto et al. (2021).

As demonstrated by Fig. 2, beyond a distance of $\log(d/{\rm pc}) = 2.2$ the lower limit on $L_{\rm rad}$ is a strong function of distance. If the above analysis is repeated only using those stars closer than this distance, the basic results are qualitatively unchanged. The best single-variable regression (K-S = 0.01, $r = 0.85$, AIC = 42) is given by $L_{\rm rad} \propto B_{\rm K}^{1.4\pm0.2}$. Two variables yield a best fit (K-S = 0.02, $r = 0.93$, AIC = 28) for $L_{\rm rad} \propto B_{\rm K}^{1.1\pm0.1} T_{\rm eff}^{4.2\pm0.9}$. Adding a third variable provids the overall best model (K-S = 0.02, $r = 0.97$, AIC = 21) for $L_{\rm rad} \propto \Phi^{1.7\pm0.2} P_{\rm rot}^{-2.4\pm0.2} f_\beta^{2.6\pm0.6}$. Once again, the results favour a dependence of radio luminosity on magnetic field strength, and an inverse dependence on rotation period. The best one- and three-variable regressions are identical to those obtained with the full dataset.

In order to test for robustness against individual outliers, the analysis was repeated removing individual stars. Results were qualitatively unchanged in all cases. Results were also qualitatively unchanged if HD 171247 and HD 64740 were reintroduced to the analysis (see § 3), although r was reduced and the AIC increased (further suggesting them to be outliers).

Linsky et al. (1992) found an empirical relationship of $L_{\rm rad} \propto \dot{M}^{0.38} B_{\rm rms}^{1.06} P_{\rm rot}^{-0.32}$, where $B_{\rm rms}$ is the root-mean-square $\langle B_z \rangle$ (as $B_{\rm d}$ was not available for most of the stars). The improvement of this relationship over a two-parameter scaling relationship involving only $\dot{M}$ and $B_{\rm rms}$ was only marginal. The much stronger dependence on magnetic field strength and rotation period is due to our much larger sample, as well as the fact that magnetic field strengths and rotational periods are known for a much larger number of stars.

Leto et al. (2021) found an essentially identical scaling relationship to that found here, i.e. a dependence of radio luminosity on the ratio $\Phi/P_{\rm rot}$, which they noted the physical dimension of an electromotive force. However, dimensional analysis of the correlation with $P_{\rm rot}$, $B_{\rm d}$, and R_* is suggestive of an alternative. B^2 is the magnetic energy density, while R_*^3 suggests the volume of the star; combined, this yields the magnetic energy of the system. The relationship $B_{\rm d}^2 R_*^3/P_{\rm rot}$ then directly yields a luminosity: the magnetic energy of the star being tapped on a rotational timescale. Indeed, if $B_{\rm d}$, R_*, and $P_{\rm rot}$ are allowed to vary independently, the best-fit relationship is $L_{\rm rad} \propto B_{\rm d}^{2.0\pm0.2} P_{\rm rot}^{-1.8\pm0.2} R_*^{3.4\pm0.6}$, i.e. a somewhat weaker R_* dependence is favoured than in the case of the magnetic flux. However, the dependence on the inverse *square* of the rotation period introduces an extra dimension of time, which must somehow be accounted for, as must the possible additional R_* term.

4 SCALING LAWS FOR MAGNETOSPHERIC EMISSION

Hα emission is governed by the CBO mechanism, which simultaneously explains the onset of emission, the increase of emission strength with increasing magnetic field strength and decreasing rotation period, and the morphology of emission line profiles (Shultz et al. 2020; Owocki et al. 2020). Plasma fed by the wind into the CM builds up to a density beyond which the magnetic field can no longer hold it. At this point, rather than the plasma being dragged by the magnetic field, magnetic field lines are pulled by the plasma which, due to the considerable rotational stress in a CM, is then hurled away from the star. As demonstrated by Townsend & Owocki (2005), the breakout density at $R_{\rm K}$ is set by $B_{\rm K}$, and is independent of $\dot{M}$; precisely this dependence on $B_{\rm K}$, and lack of sensitivity to $\dot{M}$, was found by Shultz et al. (2020) for both emission onset and emission strength scaling. Owocki et al. (2020) found an expression for the strength B_1 necessary for the density at $R_{\rm K}$ to produce an optical depth of unity in the Hα line, and showed that the threshold $B_{\rm K}/B_1$ neatly divides stars with and without Hα emission. Two-dimensional MHD simulations of CBO by ud-Doula et al. (2006, 2008) yielded a radial density gradient associated with the CBO mechanism, which in conjunction with the density at $R_{\rm K}$ set by $B_{\rm K}$ can be used to predict the optically thick area and, hence, the scaling of emission strength (Owocki et al. 2020). Finally, a characteristic emission line profile morphology, common across all Hα-bright CM host stars, was reported by Shultz et al. (2020) and shown by Owocki et al. (2020) to be a straightforward consequence of a corotating optically thick inner disk transitioning to optically transluscent in the outermost region.

A crucial subtlety that deserves emphasis is that, in contrast to expectations from 2D MHD simulations that CBO should manifest as catastrophic ejection events accompanied by large-scale reorganization of the magnetosphere (ud-Doula et al. 2006, 2008), which has indeed never been observed in the densest inner regions (Townsend et al. 2013), the Hα analysis performed by Shultz et al. (2020) instead indicates that the magnetosphere must be continuously maintained at breakout density, with CBO occuring more or less continuously on small spatial scales. However, it is worth noting that the 'giant ECM pulse' observed by Das & Chandra (2021) may have been the signature of a large-scale breakout occuring in magnetospheric regions in which the density is too low to be probed by Hα or photometry.

Hα emission and gyrosynchrotron emission occur in the same part of the rotation-magnetic confinement diagram (see Fig. 3), and Hα emission EW and radio luminosity are closely correlated (see Fig. 6). Since Hα emission is regulated by CBO, this suggests that the same may be true of gyrosynchrotron emission. In the following we develop a the-

oretical basis for this connection, which we then compare to the empirical regression analyses and measured radio luminosities.

4.1 Rotational spindown

The rotational energy of a star with moment of inertia I and rotational frequency Ω is given by

$$E_{\rm rot} = \frac{1}{2} I \Omega^2 \,. \tag{5}$$

If we assume a fixed moment of inertia, the release of rotational energy associated with a spindown $-d\Omega/dt \equiv -\dot{\Omega}$ is

$$L_{\rm rot} = I \Omega \dot{\Omega} \,. \tag{6}$$

For a magnetized star with a wind of mass loss rate $\dot{M}$, Weber & Davis (1967) argued that the loss of the star's angular momentum $J = I\Omega$ scales as

$$\dot{J} = I \dot{\Omega} = \dot{M} \Omega R_{\rm A}^2 \,, \tag{7}$$

This gives the associated release of rotational luminosity the scaling,

$$L_{\rm rot} = \dot{M} \Omega^2 R_{\rm A}^2 \,. \tag{8}$$

For a star with an equatorial field of strength $B_{\rm eq}$ at the stellar surface radius R_*, ud-Doula & Owocki (2002) and ud-Doula et al. (2008) showed that the Alfvén radius depends on a dimensionless wind magnetic confinement parameter η_* (Eqn. 2). Specifically, for a magnetic multipole of order p (=1, 2 for monopole, dipole, etc.), with radial scaling as $B \sim r^{-(p+1)}$, $R_{\rm A}$ scales as

$$\frac{R_{\rm A}}{R_*} = \eta_*^{1/2p} \,. \tag{9}$$

The Weber & Davis (1967) analysis treated the simple case of a pure radial field from a spit monopole, with $p = 1$. But ud-Doula et al. (2008) showed a base dipole field leads to a spindown that follows the Weber & Davis (1967) scaling (7), where $R_{\rm A}$ is given by eqn. (9) with a multipole index set to the $p = 2$ value for a dipole.

4.2 Breakout from centrifugal magnetospheres

The above wind-confinement scalings work well for wind-magnetic braking, which operates through wind stress on open field lines, wherein the associated Poynting flux carries away most of the angular momentum.

But for rapid rotators with a strong field, the magnetic trapping of the wind into a centrifugal magnetosphere (CM) leads to some important differences for scalings of the associated luminosity.

First, as discussed in the Appendix of Townsend & Owocki (2005, see their equation A7), for trapping and breakout from a CM, the wind speed v_∞ in the usual wind confinement parameter η_* is replaced with a characteristic dynamical speed of the stellar gravity, which we take here to be the surface orbital speed $v_{\rm orb} \equiv \sqrt{GM_*/R_*}$, giving the *centrifugal* magnetic confinement parameter

$$\eta_{\rm c} \equiv \frac{B_{\rm d}^2 R_*^2}{\dot{M} v_{\rm orb}} \,. \tag{10}$$

A second difference stems from the fact that, even for an initially dipolar field, the rotational stress of material trapped in the CM has the effect of stretching the field outwards, thus weakening its radial drop off, and so reducing the effective multipole index to $p < 2$.

Finally, this stretching ultimately leads to centrifugal breakout (CBO) events, with associated release of energy via magnetic reconnection. In general the overall total luminosity available from CBO events should follow a general scaling analogous to that for $L_{\rm rot}$,

$$\boxed{L_{\rm CBO} \approx \dot{M} \Omega^2 R_*^2 \eta_{\rm c}^{1/p}} \,. \tag{11}$$

4.2.1 Split monopole case

As a first example, consider the limit in which field lines are completely opened by the wind ram pressure into a split monopole, with $p = 1$, which gives

$$\begin{aligned} L_{\rm CBO}(p=1) &\equiv \dot{M} \Omega^2 R_*^2 \eta_{\rm c} \\ &= \frac{\Omega^2 R_*^4 B_{\rm d}^2}{v_{\rm orb}} \\ &= W \Omega R_*^3 B_{\rm d}^2 \,, \end{aligned} \tag{12}$$

where W is the critical rotation fraction (Eqn. 1). Note that the second equality recovers the empirical scaling $L_{\rm rad} \propto B^2 R_*^4 / P_{\rm rot}^2$ found in § 3.8.

Remarkably, note that in this monopole field case the dependence on wind feeding rate $\dot{M}$ has canceled! Dimensionally, the scaling now is as if the total magnetic energy over a volume set by R_*^3 is being tapped on a rotational timescale.

An alternative physical interpretation is that the field acts more like a conduit, trapping mass in a CM, with total rotational energy tapped on a breakout timescale, set in this monopole case by the orbital timescale.

4.2.2 Dipole case

More generally, this breakout luminosity depends on the wind feeding rate.

In particular, for the pure dipole scaling with $p = 2$, we find

$$\begin{aligned} L_{\rm CBO}(p=2) &= \dot{M} \Omega^2 R_*^2 \eta_{\rm c}^{1/2} \\ &= \frac{L_{\rm CBO}(p=1)}{\sqrt{\eta_{\rm c}}} \,. \end{aligned} \tag{13}$$

This has $L_{\rm CBO} \sim \sqrt{\dot{M}}$, with a weaker, linear scaling with $B_{\rm d} t$.

In general, empirical evaluation of $L_{\rm CBO}$ thus requires evaluation of the wind feeding rate $\dot{M}$, where we have used the same CAK mass-loss rates as adopted in § 3.

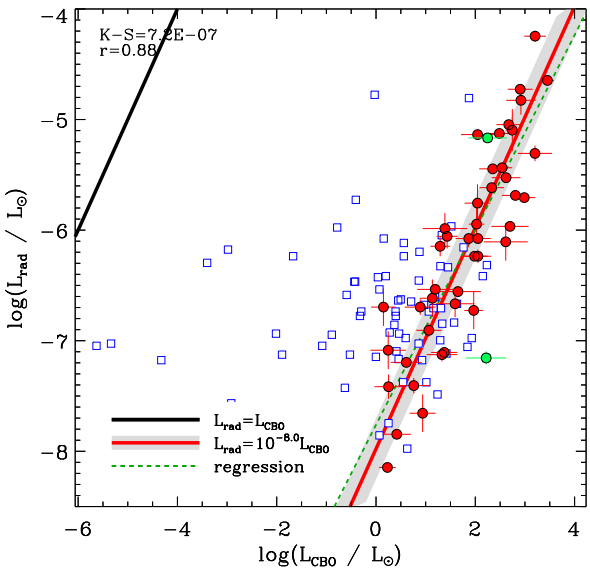

Figure 8. Radio luminosity $L_{\rm rad}$ as a function of breakout luminosity $L_{\rm CBO}$ for the split monopole case. The thick black line indicates $L_{\rm rad} = L_{\rm CBO}$; the solid red line shows the same line shifted by the mean difference. The dashed green line shows the regression. Red circles indicate stars with detected emission; blue squares, stars without emission. Green circles indicate HD 171247 and HD 64740.

In the applications below, we consider multipole indices $1 < p < 2$, intermediate between these monopole and dipole limits.

4.3 Application to radio emission

Let us next consider how well such breakout scalings for rotational luminosity correlate with observed radio luminosities, $L_{\rm rad}$. Noting that the dimensional scaling of breakout luminosity is set by the $p = 1$ case, it is convenient to cast the general scaling in the form

$$L_{\rm CBO}(p) = L_{\rm CBO}(p=1)\eta_{\rm c}^{-1+1/p} = L_{\rm CBO}(p=1)\eta_{\rm c}^{q}\,, \quad (14)$$

by which we see an inferred empirical exponent q in $\eta_{\rm c}$ implies an effective multipole exponent $p = 1/(1+q)$.

Let us first examine how well this basic, dimensional scaling of the monopole model, with $p = 1$ and so $q = 0$, fits the observed radio emission. Fig. 8 shows the observed radio luminosity $L_{\rm rad}$ as a function of $L_{\rm CBO}$ for the monopole case (Eqn. 12, i.e. with no dependence on $\dot{M}$). The thick black line shows $L_{\rm rad} = L_{\rm CBO}$, while the thick red line shows the same relationship shifted by about 8 dex, the mean difference between $L_{\rm rad}$ and $L_{\rm CBO}$ for radio-bright stars for the monopole scaling. This line is almost indistinguishable from a regression of $L_{\rm rad}$ vs. $L_{\rm CBO}$ for radio-bright stars. The relationship yields a correlation coefficient $r = 0.87$, and separates radio-bright from radio-dim stars with a K-S probability of about 10^{-8}. Further, there are very few radio-dim stars with scaled breakout luminosities greater than the upper limits on their radio luminosities, i.e. to the right of the red line; those radio-dim stars that are to the right of the line, are very close to it.

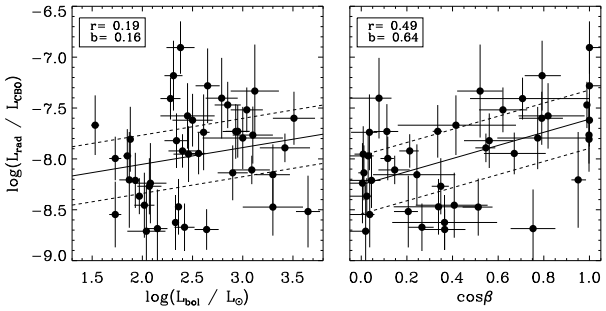

Figure 9. Ratio between $L_{\rm rad}$ and $L_{\rm CBO}$ as a function of bolometric luminosity (*left*) and $\cos\beta$ (right).

Eqn. 12 does not yield quite as high of a correlation coefficient as the purely empirical scaling in Fig. 7. To see if there is some dependence on the mass-loss rate, the left panel of Fig. 9 shows the residual radio luminosity after subtraction of the monopole $L_{\rm CBO}$ as a function of bolometric luminosity. There is only a weak dependence on $L_{\rm bol}$, with a correlation coefficient $r = 0.19$ and a slope $b = 0.16$.

Another factor that may affect radio luminosity is the obliquity angle β of the magnetic dipole axis from the rotational axis. Indeed, in the empirical regression analysis the factor f_β was found to improve the correlation (§ 3.8). In the RRM model the plasma distribution in the CM is a strong function of β, since the densest material accumulates at $R_{\rm K}$ at the intersections of the magnetic and rotational equatorial planes (Townsend & Owocki 2005). For the special case of an aligned rotator ($\beta = 0°$) this will result in plasma being evenly distributed around $R_{\rm K}$. With increasing β the plasma distribution becomes increasingly concentrated at the two intersection points, leading to a warped disk that eventually becomes two distinct clouds. Therefore, the mass confined within the CM will be a maximum for $\beta = 0°$ and a minimum for $\beta = 90°$. If reconnection in the CM is the source of the high-energy electrons that populate the radio magnetosphere, we would then naturally expect that radio luminosity should decrease with increasing β. The left panel of Fig. 9 shows the residual radio luminosity as a function of $\cos\beta$, and demonstrates that radio luminosity in fact does increase with decreasing β; in fact, the relationship is much stronger than for $\log L_{\rm bol}$, with $r = 0.49$ and $b = 0.64$.

Fig. 10 replicates Fig. 8, with the difference that corrections for $\dot{M}$ and β are accounted for. Following Eqn. 14, $\dot{M}$ dependence was determined by scaling Eqn. 12 with $\eta_{\rm C}^q$. A purely empirical correction for β was adopted as $f_\beta^x = ((1+\cos\beta)/2)^x$, such that $f_\beta(\beta = 0°) = 1$ and $f_\beta(\beta = 90°) \neq 0$. By minimizing the residuals, the best-fit exponents are $q = -0.09$ and $x = 2$. The former exponent corresponds to $p = 1.1$, implying only a very slight departure from the monopole scaling. The latter indicates an increase in $L_{\rm rad}$ by a factor of 4 as β decreases from 90° to 0°. As can be seen in Fig. 10, these corrections lead to a tighter correlation ($r = 0.92$) and a somewhat reduced ratio between $L_{\rm CBO}$ and $L_{\rm rad}$ to around 7 dex.

Changing $\alpha_{\rm eff}$ from 0.55 to 2/3 has a negligible effect on the optimal value of p. That the optimal value is so close to

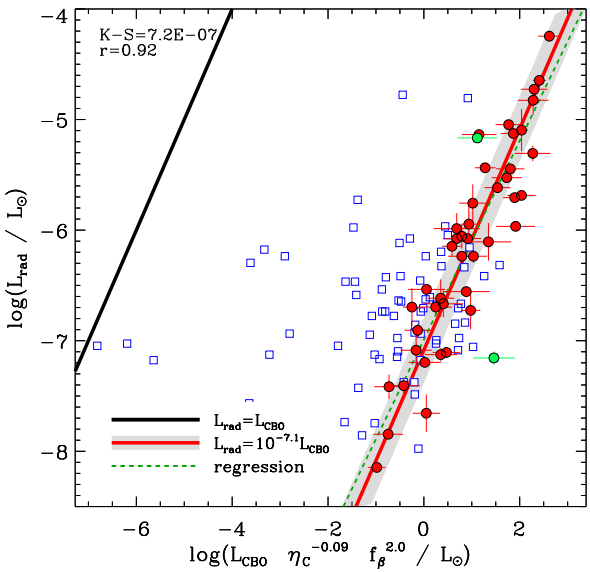

Figure 10. As Fig. 8, with $L_{\rm CBO}$ modified to account for the residual dependence on bolometric luminosity (i.e. the surface mass-flux from the wind) and the tilt angle of the magnetic dipole (Fig. 9).

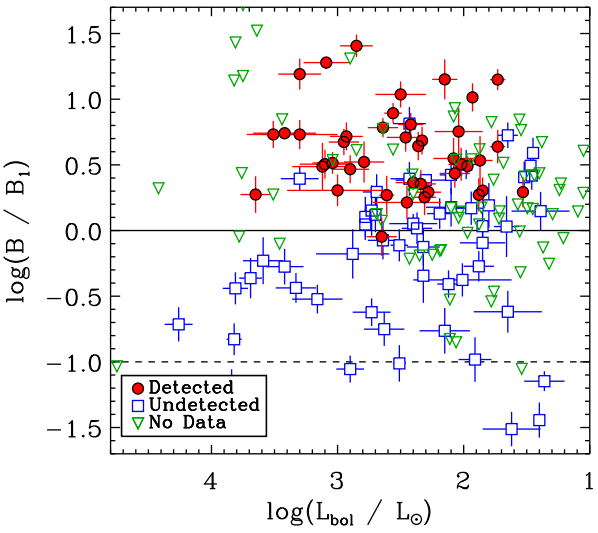

Figure 11. Ratio between surface magnetic field strength and the threshold magnetic field strength necessary to achieve a flux density of 1 mJy, as a function of bolometric luminosity.

the monopole scaling is suggestive that electron acceleration occurs in the outermost region of the magnetosphere, where the field lines have very nearly been opened.

4.3.1 Emission threshold

In their development of a breakout scaling relationship for Hα emission from CMs, Owocki et al. (2020) defined a threshold magnetic field strength $B_{\rm K1}$ as the strength of the magnetic field at $R_{\rm K}$ necessary to confine a sufficient quantity of plasma at $R_{\rm K}$ for the optical depth to reach unity. They demonstrated that all magnetic early B-type stars with $B_{\rm K}/B_{\rm K1} > 1$ are Hα-bright, while all stars with $B_{\rm K} < B_{\rm K1}$ do not display Hα emission. By solving Eqn. 12 for $B_{\rm d}$ we can derive a similar threshold value for the radio luminosity:

$$B_{\rm thresh} = \left(\frac{\epsilon L_{\rm CBO} P_{\rm rot}}{R_*^3 W} \right)^{1/2}, \qquad (15)$$

where $\epsilon \sim 10^{-8}$ is an efficiency scaling determined from the empirical ratio between $L_{\rm CBO}$ and $L_{\rm rad}$, and additional dependence on β and $\eta_{\rm C}$ is implicitly ignored. Since what is actually observed is a flux density $F_{\rm rad}$ rather than a luminosity $L_{\rm rad} \propto F_{\rm rad} d^2$, Eqn. 15 is necessarily a function of distance d. Amongst the radio-bright stars, the median flux density uncertainty is 0.1 mJy, while the median significance of a detection is around 10σ i.e. 1 mJy. We therefore take the flux density detectability threshold for the sample as 1 mJy and solve Eqn. 15 accordingly to obtain B_1 (i.e. the surface magnetic field necessary to generate 1 mJy of flux density at the star's distance). The results are shown in Fig. 11.

As expected, all radio-bright stars have $\log B_{\rm d}/B_1 \gtrsim 0$. The relationship for non-detected stars is not as clean as for the similar plot for Hα shown by Owocki et al. (2020), as there are a large number of stars with surface magnetic fields above this threshold. However, the radio observations comprising this sample, having been obtained at a variety of observatories with different capabilities over a span of over 30 years, are quite heterogeneous, with a wide range of upper limits, and many of the non-detected stars in this regime have upper limits comparable to 1 mJy. Further, generally only a single snapshot at one frequency is available, and it is possible that they were observed at inopportune rotational phases. These stars should certainly be reobserved with modern facilities.

The dashed line in Fig. 11 shows the theoretical detection limit for radio telescopes such as the upcoming Square Kilometre Array able to achieve μJy precision, under the assumption that a 10σ detection (i.e. 10 μJy) is necessary for the star's radio emission to be securely detected. As can be seen, such facilities can at least double the number of stars with measured gyrosynchrotron emission. This is especially true when stars that have not yet been observed in the radio are included: the green triangles in Fig. 11 show those stars from the samples studied by Aurière et al. (2007), Sikora et al. (2019a,b), and Shultz et al. (2019d) without radio observations, essentially all of which are expected to have radio fluxes above 10 μJy and about half of which should have fluxes above 1 mJy.

4.3.2 How CBO reconnection can lead to radio emission

Breakout events are accompanied by centrifugally driven reconnection of magnetic fields that have been stretched outward by rotational stress acting against the magnetic tension of the initially closed loops. As these loops reconnect, the associated release of magnetic energy can strongly heat the ejected plasma. Some fraction of this reconnection energy can accelerate both ions and electrons to highly

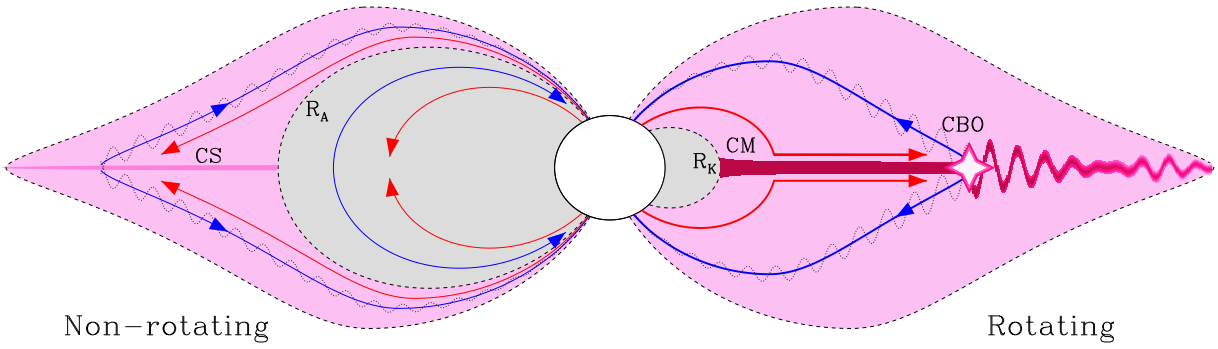

Figure 12. Schematic of the proposed model. Pink shaded regions indicate magnetic field lines contributing plasma to the electron acceleration region; grey shaded regions indicate magnetospheric regions isolated from the locus of electron acceleration. In the non-rotating case (meaning that rotation is dynamically unimportant), plasma in the inner magnetosphere is in dynamical equilibrium, with upflow (red arrows) and downflow (blue arrows) occuring at the same rate. Beyond the Alfvén radius $R_{\rm A}$, corotation ceases, and ram pressure from the wind stretches magnetic field lines, leading to the formation of a current sheet (CS) which accelerates electrons to relativistic velocities. The electrons return to the star along magnetic field lines, leading to the emission of gyrosynchrotron radiation. The inner magnetosphere is entirely isolated from the current sheet, as all plasma flow is internal. By contrast, in the rotating case, centrifugal support of plasma above the Kepler corotation radius $R_{\rm K}$ leads to the formation of a centrifugal magnetosphere (CM), in which plasma accumulates to high density (below $R_{\rm K}$ the magnetosphere remains dynamical, as in the non-rotating case). When gas pressure overloads the ability of the magnetic field to confine the plasma, plasma is ejected outwards by a centrifugal breakout (CBO) event. Magnetic reconnection during CBO leads to flaring, which accelerates electrons to high energies (indicated by the starburst), thereby providing the source electrons to populate the radio magnetosphere. Note also that the fraction of the wind plasma captured by the CM is much higher than that captured by the CS in the non-rotating case.

super-thermal energies, with some of these particles becoming trapped into gyration along closed magnetic field loops near the reconnection site. The associated gyrosynchrotron emission of the much lighter electrons can then produce the observed radio emission. This concept is illustrated in the right half of Fig. 12.

The basic scenario of electron acceleration in reconnection events, followed by gyrosynchrotron emission along magnetic loops, is indeed already a central component of the model for radio emission (Trigilio et al. 2004), illustrated in the left half of Fig. 12. However, this model is based on *wind*-driven reconnection, with no inclusion for any role of stellar rotation. As such, the available reconnection luminosity is expected to scale with the wind kinetic energy $L_{\rm wind} = \dot{M} v_\infty^2/2$. By comparison, the rotational luminosity for a multipole exponent p is larger by a factor

$$\begin{aligned} \frac{L_{\rm CBO}(p)}{L_{\rm wind}} &= 2\eta_{\rm c}^{1/p} \left(\frac{v_{\rm rot}}{v_\infty}\right)^2 \\ &= \eta_{\rm c}^{1/p}\, W^2 \left(\frac{v_{\rm esc}}{v_\infty}\right)^2 \\ &\approx \frac{\eta_{\rm c}^{1/p}\, W^2}{9}\,, \end{aligned} \tag{16}$$

where the last equality stems from the standard result that the stellar wind speed scales with the escape speed as $v_\infty \approx 3 v_{\rm esc}$. For typical values for B-star magnetospheres with $\eta_{\rm c} \approx 10^6$, $W \approx 1/2$ and $p = 4/3$, we find $L_{\rm CBO}(p = 4/3)/L_{\rm wind} \approx 880$ (using the empirically derived value of $p = 1.1$ yields an even greater ratio of almost 8000). For these W and p values, the ratio is greater than unity for even moderate confinement values $\eta_{\rm c} > 120$.

Regardless of the relative values, a central empirical result here is the finding that $L_{\rm rad}$ has a clear scaling with rotation frequency as Ω and with surface field as $B_{\rm d}^{2/p}$, dependences which are entirely missing from $L_{\rm wind}$. Indeed, we find that $\log(L_{\rm rad})$ shows only weak correlation with $L_{\rm wind}$, with $r = 0.3$. This strongly disfavors the wind-driven reconnection model proposed by Trigilio et al. (2004); instead it indicates that centrifugal breakout reconnection provides the underlying energy that leads to the radio luminosity through gyrosynchrotron emission.

While we have cast available energy in terms of loss of the star's rotational energy, one has to be careful not to take this too literally. Most (70+%) of the angular momentum loss in spindown is through magnetic field Poynting stresses. But the CBO material that leads to reconnection should share the same basic Weber-Davis scaling with $R_{\rm A}$, and it is that component that this scenario associates with the reconnection and the resulting electron acceleration and radio emission.

4.3.3 Energy source - magnetic or rotational?

The energy term in Eqn. 12 is B^2R^3, and it would therefore be natural to assume that the magnetic field is the energy source powering radio emission. However, as suggested in § 4.2.1, this is probably not the case. The mean magnetic energy $E_{\rm mag}$ amongst the radio-bright stars is about 10^{42} erg, whereas the mean rotational kinetic energy $E_{\rm rot}$ in the same sub-sample is about 10^{47} erg, i.e. the star's rotation is a vastly greater energy reservoir. Indeed $E_{\rm mag} > E_{\rm rot}$ for only 3 stars (HD 46328, HD 165474, and HD 187474), all of which have $P_{\rm rot} \sim$ years (and none of which are, of course, detected at radio frequencies).

An additional consideration is that, if the magnetic field

were the energy source, radio emission should over time draw down the magnetic energy of the star. The peak radio luminosity is around 10^{29} erg s^{-1}, implying that the magnetic energy of the most radio-luminous stars would be consumed in about 10^{13} s ~ 0.3 kyr. To the contrary, fossil magnetic fields are stable throughout a star's main sequence lifetime. For Ap/Bp stars below about 4 $M_\odot$, the decline in surface magnetic field strength is entirely consistent with flux conservation in an expanding stellar atmosphere (e.g. Kochukhov & Bagnulo 2006; Landstreet et al. 2007; Sikora et al. 2019b), while for more massive stars there is an additional, gradual decay of flux (e.g. Landstreet et al. 2007, 2008; Fossati et al. 2016; Shultz et al. 2019d) that is however, much longer than the abrupt field decay timescale that would be implied if the breakout luminosity was powered by the magnetic field. Furthermore, the most plausible mechanism for flux decay is found in small-scale convective dynamos formed in the opacity-bump He and Fe convection zones inside the radiative envelope (e.g. MacDonald & Petit 2019; Jermyn & Cantiello 2020), which naturally explains why flux does not decay in A-type stars (which lack these convection zones), and why flux apparently decays more slowly for the strongest magnetic fields (Shultz et al. 2019d) since strong fields inhibit convection (Sundqvist et al. 2013; MacDonald & Petit 2019).

In contrast to the magnetic field, which decays slowly or not at all, magnetic braking is quite abrupt (Shultz et al. 2019d; Keszthelyi et al. 2020), making the larger rotational energy reservoirs of rapidly rotating stars a more far more plausible power source. Quantitatively, for the most radio-luminous stars in the sample it would take about 30 Myr for the energy radiated by gyrosynchrotron emission to remove the total rotational energy of the star. For stars above 5 $M_\odot$ (the mass range of the brightest radio emitters), this is comparable to or greater than the main sequence lifetime.

It therefore seems that the magnetic field cannot serve as the energy source, but rather acts as a conduit for the extraction of rotational energy and its conversion into gyrosynchrotron emission. The magnetic energy lost in breakout events is immediately replenished as mass is injected into the CM by the wind, with the ion-loaded magnetic field then stretching under the centrifugal stress acting on the corotating plasma.

5 DISCUSSION

5.1 Comparison to previous results

The scaling relationship discovered by Leto et al. (2021) and confirmed in the present work, $L_{\rm rad} \propto B_{\rm d}^2 R_*^4/P_{\rm rot}^2 = (\Phi/P_{\rm rot})^2$, was explained in § 4 as a consequence of electron acceleration via centrifugal breakout. However, Leto et al. pointed out that $\Phi/P_{\rm rot}$ has the physical dimension of an electromative force $\mathcal{E}$ (EMF), which they speculated may be suggestive of an underlying mechanism. In this section we examine gyrosynchrotron emission from this standpoint, in order to contrast it with the CBO mechanism described above.

This empirical association by Leto et al. (2021) of radio emission with the voltage of an EMF also stands in contrast with the previous theoretical model by Trigilio et al. (2004), which associates the acceleration of radio-emitting non-thermal electrons with the wind-induced current sheet that forms in the middle magnetosphere. However, Leto et al. (2021) conclusively demonstrated that the wind does not provide sufficient power to the middle magnetosphere to drive the observed levels of radio emission.

The highly ionized plasma in these magnetospheres implies a very high conductivity, and so currents can form even with a vanishingly small EMF. Instead, the current density J is set by Ampere's law as a result of a curl induced in a stressed field,

$$J = \frac{c}{4\pi} \nabla \times B \,. \tag{17}$$

Even in a non-rotating wind-fed magnetosphere, large-scale stressing of the magnetic field by the wind ram pressure forces outlying closed loops to open, with a Y-type neutral point at the top of the last closed loop; above this there develops a split monopole, with a current sheet separating field lines of opposite polarity. But unless there are instabilities or induced variability, this current sheet does not by itself lead to energy dissipation that can heat the plasma or accelerate electrons. This, together with the lack of observed radio emission from stars with slow rotation, thus strongly disfavors the Trigilio et al. (2004) model based on the wind-induced current sheet.

The general principles regarding current vs. EMF scenarios can be well illustrated by a simple circuit model, using an Ohm's law $I = \mathcal{E}/\mathcal{R}$ to related current I and EMF $\mathcal{E}$ through a resistance $\mathcal{R}$. The associated dissipated power, or luminosity, scales as

$$L_{\rm emf} = I\mathcal{E} = I^2\mathcal{R} = \frac{\mathcal{E}^2}{\mathcal{R}} \,. \tag{18}$$

If one fixes the current I, then the second equality shows that in the limit of vanishing resistivity $\mathcal{R} \to 0$, the luminosity also vanishes; this underlies the fundamental issue with the current-sheet model advocated by Trigilio et al. (2004).

To understand the ramifications of the last equality of Eqns. 18 within the context of the empirical association of the gyrosynchrotron scaling law with an EMF, let us return to consideration of plasma conditions in such magnetospheres. In the notation of the present paper, the EMF can be written as $\mathcal{E} = B_* R_*^2 \Omega/c$, where the speed of light c comes in from the CGS form for the induction equation. In terms of a plasma resistivity ρ (with units of time), the circuit resistance scales with resistivity times a length over area, which in this context gives $\mathcal{R} \approx \rho R_*/R_*^2 = \rho/R_*$. Thus Eqn. 18 becomes

$$L_{\rm emf} = \frac{B_*^2 R_*^5 \Omega^2}{\rho c^2} \tag{19}$$

$$= (B_*^2 R_*^3 \Omega) \left[\frac{v_{\rm rot} R_*}{\rho c^2} \right] , \tag{20}$$

where in the latter equality, $v_{\rm rot} = \Omega R_*$ is the surface rotation speed at the stellar equator. Here the term in parenthesis separates out the dimensional luminosity, while the dimensionless ratio in square brackets can be identified as a *magneto-rotational Reynold's number*,

$$Re_{\rm mr} \equiv \frac{v_{\rm rot} R_*}{\rho c^2} \,. \tag{21}$$

Rather remarkably, Eqn. 20 has a form very similar to that derived above (cf. eqn. 12) for the monopole ($p = 1$) CBO model. However an important, indeed crucial difference is that the CBO rotation scaling is relative to the near-surface orbital speed, $v_{\rm orb} = \sqrt{GM_*/R_*}$. As such in this CBO model the associated dimensional rotation parameter $W = v_{\rm rot}/v_{\rm orb}$ is always *less than unity*.

In contrast, because of the typically very low resistivity of the ionized plasma in hot-star magnetospheres, the associated dimensionless Reynolds number is expected to be very large. To quantify this, a simple Coulomb collision model for interaction of conducting electrons with background ions in fully ionized hydrogen plasma gives

$$\rho c^2 = 4\pi r_e c \left(\frac{c}{v_e}\right)^3 \ln\Lambda \quad (22)$$

$$\approx 1.9\times 10^6 \,\frac{\rm cm^2}{\rm s}\, T_{20}^{-3/2}\,. \quad (23)$$

Here: $r_e = e^2/m_e c^2 = 2.8\times 10^{-13}$ cm is the classical electron radius (with m_e and e the electron mass and charge); $\ln\Lambda \approx 10$ is the Coulomb logarithm (which is only a very weak function of density and temperature); and the electron thermal speed for temperature T_e is given by $v_e = \sqrt{2kT_e/m_e}$.

The latter equality (23) gives the numerical evaluation as a function of a scaled temperature $T_{20} \equiv T_e/20\,{\rm kK}$. Application in (21) for typical B-star stellar parameters $R_* \approx 5R_\odot$, $v_{\rm rot} \approx 100\,{\rm km/s}$ and $T_{20} \approx 1$ then implies an exceedingly large Reynold's number,

$$Re_{\rm mr} \approx 1.8\times 10^{12}\,. \quad (24)$$

The associated dissipation luminosity (20) in this EMF scenario would thus be enormous, leading in effect to a "short circuit" that would quickly draw down the available pool of magnetic energy.

The difficulties with an association of gyrosynchrotron scaling with EMF, and with the current sheet model, stand in contrast to some key advantages of the CBO mechanism proposed here.

First, this CBO model has a more modest magnetic dissipation rate, set by the base dimensional rate $B_*^2R_*^3\Omega$ *reduced* by the rotation factor $W < 1$, instead of the enormous $Re_{\rm rm} \sim 10^{12}$ enhancement of an EMF mechanism. This CBO dissipation can be quite readily replenished over time by the centrifugal stretching of closed magnetic field lines by the constant addition of mass from the stellar wind. As such, the ultimate source of energy thus comes not from the field – which acts merely as a conduit – but from the star's rotational energy.

Second, these eventual centrifugal breakout events lead naturally and inevitably to magnetic reconnection. This thus preserves the longstanding notion (Trigilio et al. 2004) that such reconnection provides the basic mechanism to accelerate electrons to high energies, whereupon the gyration along the remaining field lines connecting back to the star results in the gyrosynchrotron emission of the observed radio luminosity.

Third, and perhaps most significantly, instead of the previous notion (Trigilio et al. 2004) that this reconnection is driven by the stellar wind – with no consideration of any role for stellar rotation – our model for CBO-driven reconnection puts rotation at the heart of the process, and so yields a scaling for luminosity that matches the strong dependence on rotation rate, as well as on magnetic field energy. Indeed, while the wind can certainly open the magnetic field and lead to the formation of a current sheet, this does not of itself provide a power source, but merely results in a slower radial decline of the magnetic field strength as compared to that of a dipole. By contrast, CBO provides a clear power source for the acceleration of electrons to high energies.

Thus, although only a small fraction of the breakout luminosity $L_{\rm CBO}$ ends up as radio luminosity, with an inferred effective efficiency $\epsilon \approx 10^{-7}$, the strong correlation between observed and predicted scalings provides strong empirical support for such a CBO model.

5.2 The case of Jupiter

Leto et al. (2021) showed that the scaling relationship for the non-thermal radio emission from dipole-like rotating magnetospheres also predicts the radio luminosity of Jupiter, suggesting an underlying similarity in the physics driving gyrosynchrotron emission from giant planets and magnetic hot stars. Adopting the same parameters as used by Leto et al. ($B_{\rm eq} = 4$ G, $P_{\rm rot} = 0.41$ d, $M_{\rm J} = 1.9\times 10^{27}$ kg, and $R_{\rm J} = 7.1\times 10^5$ km) gives $W = 0.3$. The breakout luminosity is then $\log L_{\rm CBO}/L_\odot \sim -15.9$ or, at 1 cm, $L_\nu \sim 10^7 {\rm erg\ s^{-1}\ hz^{-1}}$, translating to an expected flux of around 40 Jy at a distance of 4 AU. This is about an order magnitude higher than the observed radio luminosity of Jupiter (de Pater & Dunn 2003; de Pater et al. 2003). However, it is worth noting that in the extrapolation shown by Leto et al., Jupiter's EMF of 376 MV is near the lower envelope of the range of uncertainty inferred from hot stars, i.e. Jupiter is somewhat less luminous than predicted by a direct extrapolation of the hot star scaling relationship. Furthermore, 1 dex is at the upper range of the scatter about the $L_{\rm CBO}$ relationship (see Figs. 8 and 10).

One possible explanation for Jupiter being less luminous than predicted is that Jupiter's primary ion source, the volcanic moon Io, is effectively a point source offset from the centre of the Jovian magnetosphere. This is in contrast to stellar winds, which feed the magnetosphere isotropically and continuously from the centre. The result is that hot star magnetospheres are relatively more populated, and there is therefore more material available for the generation of gyrosynchrotron emission. Another potential issue is that in the Jovian magnetosphere reconnection takes place in the magnetotail due to stretching by the solar wind; its azimuthal extent will therefore be limited, in analogy to the obliquity dependence found in stellar magnetospheres. Exploring whether the approximate consistency between the Jovian and stellar radio luminosities is indeed due to a similarity in the underlying physics, or is merely coincidental, will require a detailed analysis that is outside the subject of this paper.

5.3 Indirect magnetometry

The magneto-rotational scaling law discovered by Leto et al. (2021) and confirmed and explained here as a consequence

Table 3. Parameters for radio-bright stars with known rotational periods but without detected magnetic fields. References: *a*, Wraight et al. (2012); *b* Catalano & Renson (1998); *c* Linsky et al. (1992); *d* Pritchard et al. (2021).

Parameter	HD 143699	HD 146001	HD 77653
$P_{\rm rot}$/d	1.323	0.586^a	1.488^b
$R_*/\mathrm{R}_\odot$	3.0 ± 0.3	2.5 ± 0.3	2.6 ± 0.1
$M_*/\mathrm{M}_\odot$	5.3 ± 0.3	4.3 ± 0.2	3.4 ± 0.1
$\log(L_{\rm rad}/L_\odot)$	-7.08 ± 0.17^c	-6.69 ± 0.17^c	-5.71 ± 0.08^d
$B_{\rm d}$/G (obs.)	<600	<500	–
$B_{\rm d}$/G (pred.)	450	430	2900

of CBO reconnection shows the potential, as pointed out by Leto et al., to be utilized as a reliable form of 'indirect magnetometry', enabling measurement of stellar magnetic fields in objects beyond the reach of contemporary spectropolarimeters. Three stars in the present sample are radio-bright and have known rotational periods, but do not have detected magnetic fields. While these stars could not be used to constrain the scaling law, they can serve as test cases for the predictive ability of the scaling law. Table 3 summarizes their key parameters.

For HD 143699 and HD 146001, the 'observed' values of $B_{\rm d}$ correspond to the 1σ upper limits derived via modelling their $\langle B_z \rangle$ error bars (both around 70 G; see Appendix C) using the MCHRD sampler, where in both cases high-resolution spectropolarimetry was used. The predicted $B_{\rm d}$ was found by solving Eqn. 15 for $B_{\rm d}$, using an efficiency $\epsilon = 10^{-7}$. For the two stars with available $\langle B_z \rangle$ measurements, the predicted $B_{\rm d}$ – about 400 G in both cases – is in both cases just below the upper limits. For HD 77653, for which spectropolarimetry is not available, Eqn. 15 predicts $B_{\rm d} \sim 3$ kG, which should be easily detectable.

5.4 Radio emission from stars with ultra-weak magnetic fields

The nearby A7 V star Altair was recently discovered by White et al. (2021) to emit non-thermal radio at cm wavelengths, with a brightness temperature around 10^4 K and a luminosity of around $\log L_{\rm rad}/L_\odot \sim -10.5$. White et al. interepreted this as chromospheric emission, possibly related to the equatorial convection zone formed due to the star's extremely rapid rotation. Robrade & Schmitt (2009) furthermore detected X-ray emission from Altair, which they interpreted as magnetic activity.

Altair was observed with Narval as part of the BRIght Target Explorer (BRITE; Weiss et al. 2014) spectropolarimetric survey (Neiner et al. 2017). No magnetic field was detected, with an uncertainty in $\langle B_z \rangle$ of about 10 G, implying that a surface magnetic dipole of around 100 G could easily have gone undetected. Using the fundamental parameters (equatorial radius $R_{\rm eq} = 2.008 \pm 0.006\ R_\odot$, $M_* = 1.86 \pm 0.03\ M_\odot$) and rotation period $P_{\rm rot} = 0.323$ d determined via careful interferometric modelling performed by Bouchaud et al. (2020) yields a critical rotation parameter $W = 0.75$ and a Kepler corotation radius $R_{\rm K} = 1.2\ R_*$. The star's CAK mass-loss rate is $\dot{M} = 10^{-13}$ $\mathrm{M}_\odot$ yr^{-1}; assuming a terminal velocity of 3000 $\mathrm{km\,s^{-1}}$, $R_{\rm K}$ will be inside the Alfvén surface so long as $B_{\rm d} > 0.1$ G, well within the upper limits on Altair's surface magnetic field and consistent with the range of ultra-weak fields detected in other main sequence A-type stars (Petit et al. 2010a; Blazère et al. 2020).

To see if the star's non-thermal radio emission might be consistent with a magnetospheric origin given the limits on the surface magnetic field, we solve Eqn. 15 for $B_{\rm d}$. We assumed the efficiency $\epsilon \sim 10^{-8}$ as inferred from the monopole relationship (i.e. ignoring corrections for $\eta_{\rm c}$ and β). This yields a predicted surface magnetic field of $B_{\rm d} \sim 10$ G. Altair's radio emission may therefore be consistent with a magnetospheric origin, although actually detecting such a weak field (which would require uncertainties on the order of a few G) is a challenging prospect given the star's broad spectral lines.

Unlike Altair, magnetic fields have actually been detected in Vega and Sirius (Petit et al. 2010a, 2011), with both stars having sub-gauss $\langle B_z \rangle$. Radio observations at mm and sub-mm wavelengths of both stars are consistent with thermal emission (Hughes et al. 2012; White et al. 2019). Sirius is a slow rotator and therefore unlikely to produce gyrosynchrotron emission. Taking Vega's stellar parameters (Yoon et al. 2010) and 0.732 d rotation period (Petit et al. 2010b) yields $R_{\rm K} = 1.5\ R_\odot$. With the CAK mass-loss rate $\dot{M} = 10^{-11.9}$ $\mathrm{M}_\odot$ yr^{-1} and the same assumption of a 3000 $\mathrm{km\,s^{-1}}$ wind terminal velocity, the miniumum surface dipole strength capable of confining the wind out to $R_{\rm K}$ is 2.3 G, $4\times$ higher than the dipolar component of about 0.5 G recovered via Zeeman Doppler Imaging (Petit et al. 2010b). The expected radio luminosity from the breakout scaling is then $\log L_{\rm rad}/L_\odot = -12$, translating at 1 cm to 0.15 μJy at Vega's 7.67 pc distance: certainly undetectable, since this is much less than the expected 1 cm photospheric flux of about 0.5 mJy.

5.5 A solution to the low-luminosity problem?

Given that Hα emission strength from CMs is apparently fully explained by CBO, as shown by Shultz et al. (2020) and Owocki et al. (2020), and as shown in the present work the same seems to be true of gyrosynchrotron emission, we would expect there to be a direct correlation between the two.

It is notable that magnetospheres are detectable in the radio in stars with CMs that are too small to be detectable in Hα. In addition to being a more sensitive magnetospheric diagnostic, this may also suggest an answer to the low-luminosity problem identified by Shultz et al. (2020) and Owocki et al. (2020). While CBO matches all of the characteristics of Hα emission from CM host stars, emission disappears entirely for stars with luminosities below about $\log L_{\rm bol}/L_\odot \sim 2.8$. This could be either a consequence of a 'leakage' mechanism, operating in conjunction with CBO to remove plasma via diffusion and/or drift across magnetic field lines (Owocki & Cranmer 2018), or due to the winds of low-luminosity stars switching into a runaway metallic wind regime (Springmann & Pauldrach 1992; Babel 1995; Owocki & Puls 2002). In the former case the leakage mechanism only becomes significant when $\dot{M}$ is low. In the latter case, Hα emission is not produced for the simple reason that the wind does not contain H ions. Notably, the peculiar surface abundances of magnetic stars may lead to enhanced

mass-loss rates as compared to non-magnetic, chemically normal stars (Krtička 2014).

Since CBO apparently governs gyrosynchrotron emission, and is seen in stars down to $\log L_{\rm bol}/L_\odot \sim 1.5$, the leakage scenario seems to be ruled out as an explanation for the absence of Hα emission. This therefore points instead to runaway metallic winds. One possible complication is that, as is apparent from Fig. 6, stars without Hα so far are also relatively dim in the radio (at least for those stars for which Hα measurements have been obtained). As can be seen in Fig. 3, these stars have systematically lower values of $B_{\rm K}$ than have been found in more luminous Hα-bright stars. Thus, a crucial test will be examination of both Hα and radio for a star with a luminosity well below 2.8, but $B_{\rm K} \sim 3$, i.e. it must be cool, very rapidly rotating ($P_{\rm rot} \sim 0.5$ d), and strongly magnetic ($B_{\rm d} \sim 10$ kG). So far no such stars are apparently known.

A further complication to the runaway wind hypothesis is provided by 36 Lyn, a relatively cool ($T_{\rm eff} \sim 13$ kK), radio-bright star which, while it does not show Hα emission, does display eclipses in Hα (Smith et al. 2006) and therefore must have H inside its magnetosphere which, presumably, originated in the stellar wind. Why no other star in 36 Lyn's $T_{\rm eff}$ range should show evidence of a similar phenomenon is not currently understood, although its peculiar magnetosphere may be related to the remarkably high toroidal component of its magnetic field in comparison to other magnetic stars, in which the toroidal component is generally quite weak (Oksala et al. 2018; Kochukhov et al. 2019).

6 CONCLUSIONS

By combining both published and unpublished radio observations, published rotational and magnetic data, and new determinations of magnetic models and rotational periods via space photometry and previously unpublished high- and low-resolution spectropolarimetry, we have conducted the largest analysis of the gyrosynchrotron emission properties of magnetic early-type stars undertaken to date.

We find that radio-bright stars occur in the same part of the rotation-magnetic confinement diagram as stars with Hα emission originating from centrifugal magnetospheres: that is to say, gyrosynchrotron emission requires rapid rotation as well as a strong magnetic field. This confirms the central result of Leto et al. (2021). Radio-bright stars are additionally generally young, with a steep drop in radio luminosity with age consistent with magnetospheric braking rapidly removing the angular momentum necessary to power the radio magnetosphere. Furthermore, there is a close correlation between the Hα emission equivalent width and radio luminosity, which is strongly suggestive of a unifying mechanism.

Multivariable regression analysis of radio luminosity yields a relation of the form $L_{\rm rad} \propto B^2 R_*^4/P_{\rm rot}^2 = (\Phi/P_{\rm rot})^2$, further confirming the results of Leto et al. (2021), although we add the refinement of an additional dependence on the geometry of the magnetic dipole such that radio luminosty declines with increasing tilt angle β. Leto et al. did not provide a definitive physical explanation regarding the origin of the non-thermal electrons, and tentatively suggested a relation to the electromotive force given that the scaling relationship has units of an EMF. We find this mechanism suffers from the difficulty that, when the resistivity is added in order to turn the voltage into a power, the magnetosphere is likely to 'short out'. Instead, we have extended the centrifugal breakout model that successfully predicts the Hα emission properties of stars with centrifugal magnetospheres (Shultz et al. 2020; Owocki et al. 2020), deriving a breakout luminosity $L_{\rm CBO} \propto (B^2 R_*^3/P_{\rm rot})W$, where the first term in brackets has natural units of luminosity, and the dimensionless critical rotation parameter W is an order-unity correction that includes the additional R_* and $P_{\rm rot}$ dependence. The radio luminosity is then $L_{\rm rad} = \epsilon L_{\rm CBO}$, where $\epsilon \sim 10^{-7}$ is an efficiency factor. Crucially, there is a nearly 1:1 correspondence between $L_{\rm rad}$ and $\epsilon L_{\rm CBO}$.

The basic scaling relationship is appropriate for a split monopole. Generalization to higher-order multipoles is accomplished with a correction $\eta_{\rm c}^{1/p}$, where η_c is the centrifugal magnetic confinement parameter and p is the multipolar order (1 for a monopole, 2 for a dipole, etc.). The small residual dependence of radio luminosity on bolometric luminosity is removed by adopting $p \sim 1.1$, i.e. a nearly monopolar field. The minimal residual dependence on bolometric luminosity confirms that the radio magnetosphere is nearly independent of the mass-loss rate. However, we find that there is a stronger dependence of the residuals on the obliquity β of the magnetic axis with respect to the rotation axis, with $L_{\rm rad}$ increasing by about a factor of 4 from $\beta = 90^\circ$ to 0°. This is consistent with expectations from the rigidly rotating magnetosphere model that the amount of plasma trapped in a centrifugal magnetosphere is a strong function of β (Townsend & Owocki 2005), since with less plasma in the CM, there will be fewer electrons available to populate the radio magnetosphere.

While radio emission and Hα emission are explained by a unifying mechanism, they probe different parts of the magnetosphere as well as different parts of the centrifugal breakout process. Hα emission probes the cool plasma trapped in the CM, which has not yet been removed by breakout. During a breakout event, some of the energy released by magnetic reconnection accelerates electrons to relativistic velocities, which then return to the star, emitting gyrosynchrotron radiation as they spiral around magnetic field lines. Following the result reported in this paper, we explain the radiation belt model proposed by Leto et al. to be the magnetic shell connected to the centrifugal breakout region close to the magnetic equator. This largely preserves the Trigilio et al. (2004) model, with the primary difference being the mechanism of electron acceleration.

Overall, the results here provide a revised foundation on which to build a detailed theoretical model for how centrifugal-breakout reconnection leads to acceleration of electrons and the associated radio gyrosynchrotron emission. In particular, we might be able to quantify the level of reconnection heating through MHD simulations, and how it scales with W, η_*, etc., as has been done for other scalings like spindown.

Future theoretical work should focus on the details of the acceleration of the electrons through reconnection, and their subsequent gyrosynchrotron emission of polarized radio emission (and perhaps other observable spectral bands like X-rays), with the specific aim to understand, and quantitatively reproduce, the inferred emission efficiencies ϵ.

There is a pressing need for more radio observations to be acquired. SEDs have been measured for only a small number of stars, and it is not known how these vary with fundamental, magnetic, or rotational parameters. Rotational phase coverage is likewise available in only a small number of cases; the geometrical dependence found here for the radio luminosity suggests that comparable effects might be seen in phase curves, which may be important in reconstructing plasma distributions out of the magnetic-equatorial plane probed by visible data. More sensitive observations might seek to discover if gyrosynchrotron emission disappears entirely in stars without centrifugal magnetospheres, or if slowly rotating stars in fact emit ultra-weak radio driven by the classical middle magnetosphere current sheet mechanism. Indeed, while gyrosynchroton emission has not yet been detected from slow rotators, there are very few stars in the dynamical magnetosphere regime with radio data. Finally, as pointed out by Leto et al. (2021), the close correlation between radio luminosity and magnetic field strength suggests that radio data might become an important form of indirect magnetometry for stars that are too dim for their surface magnetic fields to be measured using Zeeman effect spectropolarimetry, but for which rotational periods are known via e.g. *TESS* space photometry.

ACKNOWLEDGMENTS

The authors thank Dr. Stephen Drake for providing his unpublished radio measurements, which they hope have been put to good use. This work is based on observations obtained at the Canada-France-Hawaii Telescope (CFHT) which is operated by the National Research Council of Canada, the Institut National des Sciences de l'Univers (INSU) of the Centre National de la Recherche Scientifique (CNRS) of France, and the University of Hawaii, and at the Observatoire du Pic du Midi (France), operated by the INSU. This paper includes data collected by the TESS mission, which are publicly available from the Mikulski Archive for Space Telescopes (MAST). Funding for the TESS mission is provided by NASAs Science Mission directorate. We thank the staff of the GMRT that made the uGMRT observations possible. The GMRT is run by the National Centre for Radio Astrophysics of the Tata Institute of Fundamental Research. This work has made use of the VALD database, operated at Uppsala University, the Institute of Astronomy RAS in Moscow, and the University of Vienna. This research has made use of the SIMBAD database, operated at CDS, Strasbourg, France. MES acknowledges the financial support provided by the Annie Jump Cannon Fellowship, supported by the University of Delaware and endowed by the Mount Cuba Astronomical Observatory. AuD acknowledges support by NASA through Chandra Award 26 number TM1-22001B issued by the Chandra X-ray Observatory 27 Center, which is operated by the Smithsonian Astrophysical Observatory for and behalf of NASA under contract NAS8-03060. VK acknowledges support by Natural Sciences and Engineering Research Council of Canada (NSERC). PC and BD acknowledge support of the Department of Atomic Energy, Government of India, under project no. 12-R&D-TFR-5.02-0700. GAW acknowledges Discovery Grant support from the Natural Science and Engineering Research Council (NSERC) of Canada. JDL acknowledges support from the Natural Sciences and Engineering Research Council of Canada (NSERC), funding reference number 6377–2016. OK acknowledges support by the Swedish Research Council and the Swedish National Space Board. The material is based upon work supported by NASA under award number 80GSFC21M0002.

DATA AVAILABILITY STATEMENT

Reduced ESPaDOnS spectra are available at the CFHT archive maintained by the CADC[3], where they can be found via standard stellar designations. ESPaDOnS and Narval data can also be obtained at the PolarBase archive[4]. *Kepler-2* and *TESS* data are available at the MAST archive[5]. *Hipparcos* data are available through SIMBAD and Vizier[6]. DAO and uGMRT observations are available from the authors at request.

REFERENCES

Adelman S. J., 1994, *MNRAS*, 266, 97
Adelman S. J., 1997, *A&AS*, 125, 65
Adelman S. J., 2008, *PASP*, 120, 595
Alecian G., 2015, *MNRAS*, 454, 3143
Alecian G., Stift M. J., 2019, *MNRAS*, 482, 4519
Alecian E., et al., 2008, *A&A*, 481, L99
Alecian E., et al., 2011, *A&A*, 536, L6
Alecian E., et al., 2014, *A&A*, 567, A28
Aurière M., et al., 2007, *A&A*, 475, 1053
Babcock H. W., 1958, *ApJS*, 3, 141
Babel J., 1995, *A&A*, 301, 823
Babel J., Montmerle T., 1997, *ApJ*, 485, L29
Bagnulo S., Fossati L., Landstreet J. D., Izzo C., 2015a, *A&A*, 583, A115
Bagnulo S., Fossati L., Landstreet J. D., Izzo C., 2015b, *A&A*, 583, A115
Bailey J. D., Landstreet J. D., 2013, *MNRAS*, 432, 1687
Bernhard K., Hümmerich S., Paunzen E., 2020, *MNRAS*, 493, 3293
Bieging J. H., Abbott D. C., Churchwell E. B., 1989, *ApJ*, 340, 518
Blazère A., Petit P., Neiner C., Folsom C., Kochukhov O., Mathis S., Deal M., Landstreet J., 2020, *MNRAS*, 492, 5794
Blomme R., De Becker M., Volpi D., Rauw G., 2010, *A&A*, 519, A111
Bohlender D. A., Monin D., 2011, *AJ*, 141, 169
Bohlender D. A., Landstreet J. D., Brown D. N., Thompson I. B., 1987, *ApJ*, 323, 325
Bohlender D. A., Landstreet J. D., Thompson I. B., 1993a, *A&A*, 269, 355
Bohlender D. A., Landstreet J. D., Thompson I. B., 1993b, *A&A*, 269, 355

[3] https://www.cadc-ccda.hia-iha.nrc-cnrc.gc.ca/en/
[4] http://polarbase.irap.omp.eu/
[5] https://mast.stsci.edu/portal/Mashup/Clients/Mast/Portal.html
[6] https://vizier.u-strasbg.fr/viz-bin/VizieR

Bolton C. T., Harmanec P., Lyons R. W., Odell A. P., Pyper D. M., 1998, *A&A*, 337, 183
Borra E. F., 1975, *ApJ*, 196, L109
Borra E. F., 1981, *ApJ*, 249, L39
Borra E. F., Landstreet J. D., 1977, *ApJ*, 212, 141
Borra E. F., Landstreet J. D., 1980, *ApJS*, 42, 421
Borra E. F., Landstreet J. D., Thompson I., 1983, *ApJS*, 53, 151
Borucki W. J., et al., 2010, Science, 327, 977
Bouchaud K., Domiciano de Souza A., Rieutord M., Reese D. R., Kervella P., 2020, *A&A*, 633, A78
Braithwaite J., 2009, *MNRAS*, 397, 763
Braithwaite J., Spruit H. C., 2004, *Nature*, 431, 819
Briquet M., Aerts C., De Cat P., 2001, *A&A*, 366, 121
Brown D. N., Shore S. N., Sonneborn G., 1985, *AJ*, 90, 1354
Bychkov V. D., Shtol' V. G., Hubrig S., 1997, in Glagolevskij Y., Romanyuk I., eds, Stellar Magnetic Fields. pp 197–199
Bychkov V. D., Bychkova L. V., Madej J., 2003, *A&A*, 407, 631
Bychkov V. D., Bychkova L. V., Madej J., 2005, *A&A*, 430, 1143
Bychkov V. D., Bychkova L. V., Madej J., 2020, arXiv e-prints, p. arXiv:2004.14099
Capitanio L., Lallement R., Vergely J. L., Elyajouri M., Monreal-Ibero A., 2017, *A&A*, 606, A65
Castor J. I., Abbott D. C., Klein R. I., 1975, *ApJ*, 195, 157
Catalano F. A., Leone F., 1991, *A&A*, 244, 327
Catalano F. A., Renson P., 1998, *A&AS*, 127, 421
Chandra P., et al., 2015, *MNRAS*, 452, 1245
Conti P. S., 1970, *ApJ*, 159, 723
Daley-Yates S., Stevens I. R., ud-Doula A., 2019, *MNRAS*, 489, 3251
Das B., Chandra P., 2021, arXiv e-prints, p. arXiv:2107.00849
Das B., Chandra P., Wade G. A., 2018, *MNRAS*, 474, L61
Das B., Chandra P., Shultz M. E., Wade G. A., 2019a, *MNRAS*, 489, L102
Das B., Chandra P., Shultz M. E., Wade G. A., 2019b, *ApJ*, 877, 123
Das B., Mondal S., Chandra P., 2020, *ApJ*, 900, 156
David-Uraz A., et al., 2019, *MNRAS*, 487, 304
Donati J.-F., Semel M., Rees D. E., 1992, *A&A*, 265, 669
Donati J.-F., Semel M., Carter B. D., Rees D. E., Collier Cameron A., 1997, MNRAS, 291, 658
Donati J.-F., et al., 2006, *MNRAS*, 370, 629
Drake S. A., Abbott D. C., Bastian T. S., Bieging J. H., Churchwell E., Dulk G., Linsky J. L., 1987, *ApJ*, 322, 902
Drake S. A., Wade G. A., Linsky J. L., 2006, in Wilson A., ed., ESA Special Publication Vol. 604, The X-ray Universe 2005. p. 73
Dubath P., et al., 2011, *MNRAS*, 414, 2602
Duez V., Braithwaite J., Mathis S., 2010, *ApJ*, 724, L34
Ekström S., et al., 2012, *A&A*, 537, A146
Erba C., Shultz M. E., Petit V., Fullerton A. W., Henrichs H. F., Kochukhov O., Rivinius T., Wade G. A., 2021, *MNRAS*, 506, 2296
Folsom C. P., et al., 2016, *MNRAS*, 457, 580
Folsom C. P., et al., 2018, *MNRAS*, 474, 4956
Fossati L., et al., 2014, *A&A*, 562, A143
Fossati L., et al., 2016, *A&A*, 592, A84
Gaia Collaboration et al., 2021, *A&A*, 649, A6
Gayley K. G., 1995, *ApJ*, 454, 410
Ghazaryan S., Alecian G., Hakobyan A. A., 2018, *MNRAS*, 480, 2953
Ghazaryan S., Alecian G., Hakobyan A. A., 2019, *MNRAS*, 487, 5922
Głębocki R., Gnaciński P., 2005, in Favata F., Hussain G. A. J., Battrick B., eds, ESA Special Publication Vol. 560, 13th Cambridge Workshop on Cool Stars, Stellar Systems and the Sun. p. 571
Gollnow H., 1971, The Observatory, 91, 37
Grunhut J. H., et al., 2012, *MNRAS*, 419, 1610
Grunhut J. H., et al., 2017, *MNRAS*, 465, 2432
Hauck B., Mermilliod M., 1998, *A&AS*, 129, 431
Henrichs H. F., et al., 2013, *A&A*, 555, A46
Howell S. B., et al., 2014, *PASP*, 126, 398
Hubrig S., North P., Schöller M., Mathys G., 2006, Astronomische Nachrichten, 327, 289
Hubrig S., North P., Schöller M., 2007, *Astron. Nachr.* , 328, 475
Hughes A. M., et al., 2012, *ApJ*, 750, 82
Hümmerich S., et al., 2018, *A&A*, 619, A98
Järvinen S. P., Hubrig S., Ilyin I., Schöller M., Nieva M. F., Przybilla N., Castro N., 2018, *A&A*, 618, L2
Jermyn A. S., Cantiello M., 2020, *ApJ*, 900, 113
Kemp J. C., Wolstencroft R. D., 1973, *ApJ*, 182, L43
Kervella P., Arenou F., Mignard F., Thévenin F., 2019, *A&A*, 623, A72
Keszthelyi Z., Meynet G., Georgy C., Wade G. A., Petit V., David-Uraz A., 2019, *MNRAS*, 485, 5843
Keszthelyi Z., et al., 2020, *MNRAS*, 493, 518
Khalack V., LeBlanc F., 2015, *AJ*, 150, 2
Kochukhov O., Bagnulo S., 2006, *A&A*, 450, 763
Kochukhov O., Wade G. A., 2016, *A&A*, 586, A30
Kochukhov O., Bagnulo S., Wade G. A., Sangalli L., Piskunov N., Landstreet J. D., Petit P., Sigut T. A. A., 2004, *A&A*, 414, 613
Kochukhov O., Makaganiuk V., Piskunov N., 2010, *A&A*, 524, A5
Kochukhov O., Lundin A., Romanyuk I., Kudryavtsev D., 2011, *ApJ*, 726, 24
Kochukhov O., Lüftinger T., Neiner C., Alecian E., MiMeS Collaboration 2014, *A&A*, 565, A83
Kochukhov O., Silvester J., Bailey J. D., Landstreet J. D., Wade G. A., 2017, *A&A*, 605, A13
Kochukhov O., Shultz M., Neiner C., 2019, *A&A*, 621, A47
Kochukhov O., Khalack V., Kobzar O., Neiner C., Paunzen E., Labadie-Bartz J., David-Uraz A., 2021, arXiv e-prints, p. arXiv:2107.09096
Kounkel M., et al., 2017, *ApJ*, 834, 142
Krtička J., 2014, *A&A*, 564, A70
Krtička J., Mikulášek Z., Henry G. W., Zverko J., Žižovský J., Skalický J., Zvěřina P., 2009, *A&A*, 499, 567
Krtička J., Mikulášek Z., Lüftinger T., Shulyak D., Zverko J., Žižňovský J., Sokolov N. A., 2012, *A&A*, 537, A14
Krtička J., Mikulášek Z., Lüftinger T., Jagelka M., 2015, *A&A*, 576, A82
Kudryavtsev D. O., Romanyuk I. I., Elkin V. G., Paunzen E., 2006, *MNRAS*, 372, 1804
Kupka F. G., Piskunov N., Ryabchikova T. A., Stempels H. C., Weiss W. W., 1999, *A&AS*, 138, 119

Kupka F. G., Ryabchikova T. A., Piskunov N. E., Stempels H. C., Weiss W. W., 2000, Balt. Astron., 9, 590
Kurapati S., et al., 2017, *MNRAS*, 465, 2160
Lallement R., Vergely J. L., Valette B., Puspitarini L., Eyer L., Casagrande L., 2014, *A&A*, 561, A91
Lallement R., et al., 2018, *A&A*, 616, A132
Lamers H. J. G. L. M., Leitherer C., 1993, *ApJ*, 412, 771
Lamers H. J. G. L. M., Snow T. P., Lindholm D. M., 1995, *ApJ*, 455, 269
Landstreet J. D., 1982, *ApJ*, 258, 639
Landstreet J. D., Borra E. F., 1978, *ApJ*, 224, L5
Landstreet J. D., Mathys G., 2000, *A&A*, 359, 213
Landstreet J. D., Bagnulo S., Andretta V., Fossati L., Mason E., Silaj J., Wade G. A., 2007, *A&A*, 470, 685
Landstreet J. D., et al., 2008, *A&A*, 481, 465
Lanz T., Mathys G., 1991, *A&AS*, 90, 365
Lenz P., Breger M., 2005, Communications in Asteroseismology, 146, 53
Leone F., Catanzaro G., 2001, *A&A*, 365, 118
Leone F., Trigilio C., Umana G., 1994, *A&A*, 283, 908
Leone F., Umana G., Trigilio C., 1996, *A&A*, 310, 271
Leone F., Trigilio C., Neri R., Umana G., 2004, *A&A*, 423, 1095
Leone F., Bohlender D. A., Bolton C. T., Buemi C., Catanzaro G., Hill G. M., Stift M. J., 2010, *MNRAS*, 401, 2739
Leto P., Trigilio C., Buemi C. S., Leone F., Umana G., 2012, *MNRAS*, 423, 1766
Leto P., Trigilio C., Buemi C. S., Umana G., Ingallinera A., Cerrigone L., 2016, *MNRAS*, 459, 1159
Leto P., et al., 2017, *MNRAS*, 467, 2820
Leto P., et al., 2018, *MNRAS*, 476, 562
Leto P., et al., 2020a, *MNRAS*, 493, 4657
Leto P., et al., 2020b, *MNRAS*, 499, L72
Leto P., et al., 2021, *MNRAS*,
Linder N., Rauw G., Martins F., Sana H., De Becker M., Gosset E., 2008, *A&A*, 489, 713
Linsky J. L., Drake S. A., Bastian T. S., 1992, *ApJ*, 393, 341
MacDonald J., Petit V., 2019, *MNRAS*, 487, 3904
Makaganiuk V., et al., 2011, *A&A*, 525, A97
Markova N., Puls J., 2008, *A&A*, 478, 823
Mathys G., 1989, FCPh, 13, 143
Mathys G., 1991a, *A&AS*, 89, 121
Mathys G., 1991b, *A&AS*, 89, 121
Mathys G., 2017, *A&A*, 601, A14
Mathys G., Hubrig S., 1997a, *A&AS*, 124, 475
Mathys G., Hubrig S., 1997b, *A&AS*, 124, 475
Mathys G., Manfroid J., Renson P., 1986, *A&AS*, 63, 403
McMullin J. P., Waters B., Schiebel D., Young W., Golap K., 2007, in Shaw R. A., Hill F., Bell D. J., eds, Astronomical Society of the Pacific Conference Series Vol. 376, Astronomical Data Analysis Software and Systems XVI. p. 127
Michaud G., Charland Y., Megessier C., 1981, *A&A*, 103, 244
Mikulášek Z. Z., Krtička J., Janík J., Henry G. W., Zejda M., Shultz M., Paunzen E., Jagelka M., 2017, in Balega Y. Y., Kudryavtsev D. O., Romanyuk I. I., Yakunin I. A., eds, Astronomical Society of the Pacific Conference Series Vol. 510, Stars: From Collapse to Collapse. p. 220 (arXiv:1702.02195)
Moiseeva A. V., Romanyuk I. I., Semenko E. A., Kudryavtsev D. O., Yakunin I. A., 2019, Astrophysical Bulletin, 74, 62
Monin D., Bohlender D., Hardy T., Saddlemyer L., Fletcher M., 2012, *PASP*, 124, 329
Napiwotzki R., Schoenberner D., Wenske V., 1993, *A&A*, 268, 653
Nazé Y., Petit V., Rinbrand M., Cohen D., Owocki S., ud-Doula A., Wade G. A., 2014, *ApJS*, 215, 10
Neiner C., Geers V. C., Henrichs H. F., Floquet M., Frémat Y., Hubert A. M., Preuss O., Wiersema K., 2003a, *A&A*, 406, 1019
Neiner C., et al., 2003b, *A&A*, 411, 565
Neiner C., Wade G., Marsden S., Blazère A., 2017, in Zwintz K., ed., Proceedings of the Polish Astronomical Society Vol. 5, Second BRITE-Constellation Science Conference - Small satellites - big science. p. 86 (arXiv:1502.00226), doi:10.1017/S1743921315004524
Netopil M., Paunzen E., Maitzen H. M., North P., Hubrig S., 2008, *A&A*, 491, 545
Netopil M., Paunzen E., Hümmerich S., Bernhard K., 2017, *MNRAS*, 468, 2745
Nieva M.-F., 2013, *A&A*, 550, A26
North P., 1984, *A&A*, 141, 328
Oksala M. E., Wade G. A., Marcolino W. L. F., Grunhut J., Bohlender D., Manset N., Townsend R. H. D., Mimes Collaboration 2010, *MNRAS*, 405, L51
Oksala M. E., et al., 2015a, *MNRAS*, 451, 2015
Oksala M. E., Grunhut J. H., Kraus M., Borges Fernandes M., Neiner C., Condori C. A. H., Campagnolo J. C. N., Souza T. B., 2015b, *A&A*, 578, A112
Oksala M. E., Silvester J., Kochukhov O., Neiner C., Wade G. A., MiMeS Collaboration 2018, *MNRAS*, 473, 3367
Owocki S. P., Cranmer S. R., 2018, *MNRAS*, 474, 3090
Owocki S. P., Puls J., 2002, *ApJ*, 568, 965
Owocki S. P., Shultz M. E., ud-Doula A., Sundqvist J. O., Townsend R. H. D., Cranmer S. R., 2020, *MNRAS*, 499, 5366
Paunzen E., 2015, *A&A*, 580, A23
Perryman M. A. C., et al., 1997, *A&A*, 323, L49
Petit P., et al., 2010a, *A&A*, 523, A41
Petit P., et al., 2010b, *A&A*, 523, A41
Petit P., et al., 2011, *A&A*, 532, L13
Petit V., et al., 2013, *MNRAS*, 429, 398
Petit P., Louge T., Théado S., Paletou F., Manset N., Morin J., Marsden S. C., Jeffers S. V., 2014, *PASP*, 126, 469
Petit V., et al., 2019, *MNRAS*, 489, 5669
Piskunov N. E., Kupka F., Ryabchikova T. A., Weiss W. W., Jeffery C. S., 1995, *A&AS*, 112, 525
Pittard J. M., Dougherty S. M., Coker R. F., O'Connor E., Bolingbroke N. J., 2006, *A&A*, 446, 1001
Plachinda S. I., Yakushechkin A. V., Sergeev S. G., 1993, Bulletin Crimean Astrophysical Observatory, 87, 83
Pourbaix D., et al., 2004, *A&A*, 424, 727
Preston G. W., 1967, *ApJ*, 150, 547
Pritchard J., et al., 2021, *MNRAS*, 502, 5438
Rebull L. M., Stauffer J. R., Cody A. M., Hillenbrand L. A., David T. J., Pinsonneault M., 2018, *AJ*, 155, 196
Renson P., Catalano F. A., 2001, *A&A*, 378, 113
Renson P., Manfroid J., 2009, *A&A*, 498, 961
Ricker G. R., et al., 2015,

Journal of Astronomical Telescopes, Instruments, and Systems, 1, 014003
Rivinius T., Szeifert T., Barrera L., Townsend R. H. D., Štefl S., Baade D., 2010, *MNRAS*, 405, L46
Rivinius T., Townsend R. H. D., Kochukhov O., Štefl S., Baade D., Barrera L., Szeifert T., 2013, *MNRAS*, 429, 177
Robrade J., Schmitt J. H. M. M., 2009, *A&A*, 497, 511
Romanyuk I. I., Semenko E. A., Kudryavtsev D. O., 2015, Astrophysical Bulletin, 70, 444
Romanyuk I. I., Semenko E. A., Yakunin I. A., Kudryavtsev D. O., Moiseeva A. V., 2016a, Astrophysical Bulletin, 71, 436
Romanyuk I. I., Semenko E. A., Kudryavtsev D. O., Moiseevaa A. V., 2016b, Astrophysical Bulletin, 71, 302
Romanyuk I. I., Semenko E. A., Yakunin I. A., Kudryavtsev D. O., Moiseeva A. V., 2017a, Astrophysical Bulletin, 72, 165
Romanyuk I. I., Semenko E. A., Kudryavtsev D. O., Moiseeva A. V., Yakunin I. A., 2017b, Astrophysical Bulletin, 72, 391
Romanyuk I. I., Semenko E. A., Moiseeva A. V., Kudryavtsev D. O., Yakunin I. A., 2018, Astrophysical Bulletin, 73, 178
Romanyuk I. I., Semenko E. A., Moiseeva A. V., Yakunin I. A., Kudryavtsev D. O., 2019, Astrophysical Bulletin, 74, 55
Romanyuk I. I., Moiseeva A. V., Semenko E. A., Kudryavtsev D. O., Yakunin I. A., 2020, Astrophysical Bulletin, 75, 294
Romanyuk I. I., Semenko E. A., Moiseeva A. V., Yakunin I. A., Kudryavtsev D. O., 2021a, Astrophysical Bulletin, 76, 39
Romanyuk I. I., Semenko E. A., Moiseeva A. V., Yakunin I. A., Kudryavtsev D. O., 2021b, Astrophysical Bulletin, 76, 163
Ruediger G., Scholz G., 1988, Astronomische Nachrichten, 309, 181
Rusomarov N., Kochukhov O., Ryabchikova T., Ilyin I., 2016, *A&A*, 588, A138
Ryabchikova T. A., Piskunov N. E., Kupka F., Weiss W. W., 1997, Balt. Astron., 6, 244
Ryabchikova T., Piskunov N., Kurucz R. L., Stempels H. C., Heiter U., Pakhomov Y., Barklem P. S., 2015, Phys. Scr., 90, 054005
Schneider F. R. N., Ohlmann S. T., Podsiadlowski P., Röpke F. K., Balbus S. A., Pakmor R., Springel V., 2019, *Nature*, 574, 211
Semenko E. A., Kudryavtsev D. O., Ryabchikova T. A., Romanyuk I. I., 2008, Astrophysical Bulletin, 63, 128
Shore S. N., Brown D. N., 1990, *ApJ*, 365, 665
Shultz M., et al., 2015, *MNRAS*, 449, 3945
Shultz M., Wade G. A., Rivinius T., Neiner C., Henrichs H., Marcolino W., MiMeS Collaboration 2017, *MNRAS*, 471, 2286
Shultz M., Rivinius T., Wade G. A., Alecian E., Petit V., 2018a, *MNRAS*, 475, 839
Shultz M. E., et al., 2018b, *MNRAS*, 475, 5144
Shultz M., Kochukhov O., Wade G. A., Rivinius T., 2018c, *MNRAS*, 478, L39
Shultz M., et al., 2019a, *MNRAS*, 482, 3950
Shultz M. E., Wade G. A., Rivinius T., Alecian E., Neiner C., Petit V., Wisniewski J. P., 2019b, *MNRAS*, 485, 1508
Shultz M., Rivinius T., Das B., Wade G. A., Chandra P., 2019c, *MNRAS*, 486, 5558
Shultz M. E., et al., 2019d, *MNRAS*, 490, 274
Shultz M. E., et al., 2020, *MNRAS*, 499, 5379
Shultz M. E., Alecian E., Petit V., Bagnulo S., Böhm T., Folsom C. P., Wade G. A., MiMeS Collaboration 2021a, *MNRAS*, 504, 3203
Shultz M. E., Rivinius T., Wade G. A., Kochukhov O., Alecian E., David-Uraz A., Sikora J., 2021b, *MNRAS*, 504, 4850
Sikora J., et al., 2015, *MNRAS*, 451, 1928
Sikora J., et al., 2016, *MNRAS*, 460, 1811
Sikora J., Wade G. A., Power J., Neiner C., 2019a, *MNRAS*, 483, 2300
Sikora J., Wade G. A., Power J., Neiner C., 2019b, *MNRAS*, 483, 3127
Sikora J., et al., 2019c, *MNRAS*, 487, 4695
Silvester J., et al., 2009, *MNRAS*, 398, 1505
Silvester J., Wade G. A., Kochukhov O., Bagnulo S., Folsom C. P., Hanes D., 2012, *MNRAS*, 426, 1003
Silvester J., Kochukhov O., Wade G. A., 2014a, *MNRAS*, 440, 182
Silvester J., Kochukhov O., Wade G. A., 2014b, *MNRAS*, 444, 1442
Silvester J., Kochukhov O., Wade G. A., 2015, *MNRAS*, 453, 2163
Smith M. A., Wade G. A., Bohlender D. A., Bolton C. T., 2006, *A&A*, 458, 581
Springmann U. W. E., Pauldrach A. W. A., 1992, *A&A*, 262, 515
Sundqvist J. O., Petit V., Owocki S. P., Wade G. A., Puls J., MiMeS Collaboration 2013, *MNRAS*, 433, 2497
Thompson I. B., Brown D. N., Landstreet J. D., 1987, *ApJS*, 64, 219
Townsend R. H. D., Owocki S. P., 2005, *MNRAS*, 357, 251
Townsend R. H. D., Oksala M. E., Cohen D. H., Owocki S. P., ud-Doula A., 2010, *ApJ*, 714, L318
Townsend R. H. D., et al., 2013, *ApJ*, 769, 33
Trigilio C., Leto P., Leone F., Umana G., Buemi C., 2000a, *A&A*, 362, 281
Trigilio C., Leto P., Leone F., Umana G., Buemi C., 2000b, *A&A*, 362, 281
Trigilio C., Leto P., Umana G., Leone F., Buemi C. S., 2004, *A&A*, 418, 593
Trigilio C., Leto P., Umana G., Buemi C. S., Leone F., 2011, *ApJ*, 739, L10
Vidotto A. A., et al., 2014, *MNRAS*, 441, 2361
Vink J. S., de Koter A., Lamers H. J. G. L. M., 2000, *A&A*, 362, 295
Vink J. S., de Koter A., Lamers H. J. G. L. M., 2001, *A&A*, 369, 574
Wade G. A., et al., 2016, *MNRAS*, 456, 2
Watson C. L., Henden A. A., Price A., 2006, Society for Astronomical Sciences Annual Symposium, 25, 47
Weber E. J., Davis Jr. L., 1967, *ApJ*, 148, 217
Weiss W., Malanushenko V. P., Shakhovskoi N. M., 1990, Izvestiya Ordena Trudovogo Krasnogo Znameni Krymskoj Astrofizicheskoj Observatorii, 82, 69
Weiss W. W., et al., 2014, *PASP*, 126, 573
White J. A., et al., 2019, *ApJ*, 875, 55
White J. A., et al., 2021, *ApJ*, 912, L5

Wolff S. C., Bonsack W. K., 1972, *ApJ*, 176, 425

Woodcock K., Wade G. A., Kochukhov O., Sikora J., Pigulski A., 2021, *MNRAS*, 502, 5200

Worthey G., Lee H.-c., 2011, *ApJS*, 193, 1

Wraight K. T., Fossati L., Netopil M., Paunzen E., Rode-Paunzen M., Bewsher D., Norton A. J., White G. J., 2012, *MNRAS*, 420, 757

Yakunin I., et al., 2015, *MNRAS*, 447, 1418

Yoon J., Peterson D. M., Kurucz R. L., Zagarello R. J., 2010, *ApJ*, 708, 71

de Pater I., Dunn D. E., 2003, Icarus, 163, 449

de Pater I., et al., 2003, Icarus, 163, 434

ud-Doula A., Owocki S. P., 2002, ApJ, 576, 413

ud-Doula A., Townsend R. H. D., Owocki S. P., 2006, ApJl, 640, L191

ud-Doula A., Owocki S. P., Townsend R. H. D., 2008, MNRAS, 385, 97

ud-Doula A., Owocki S. P., Townsend R. H. D., 2009, MNRAS, 392, 1022

ud-Doula A., Owocki S., Townsend R., Petit V., Cohen D., 2014, *MNRAS*, 441, 3600

van Leeuwen F., 2007, *A&A*, 474, 653

APPENDIX A: SAMPLE SUMMARY TABLE

Table A1. Stellar parameters, rotational periods, dipolar magnetic field strengths, and radio luminosities for the sample. Stars with superscripts are listed in Appendix B if they have new radio (*f*)lux density observations, and are discussed in Appendix C if new (*m*)agnetic data or (*r*)otational periods are available. Superscipt numbers in square brackets in other columns correspond to the reference key at the end of the table.

Star	$\log \frac{L_{\rm bol}}{L_\odot}$	$\frac{T_{\rm eff}}{\rm kK}$	$\frac{M_*}{\rm M_\odot}$	$\frac{v \sin i}{\rm km\ s^{-1}}$	$\frac{P_{\rm rot}}{\rm d}$	$\frac{\beta}{\rm deg}$	$\frac{B_{\rm d}}{\rm kG}$	$\log \frac{L_{\rm rad}}{\rm L_\odot}$
ALS8988^{r}	4.05±0.27	27.3± 1.4[126]	10.6± 0.6	23[40]	–	–	>1.5[40]	<-4.31[84]
ALS9522	3.65±0.12	22.4± 1.1[117]	6.0± 0.1	105[117]	1.091[117]	78^{+2}_{-3}	11^{+3}_{-1}[117]	-5.31±0.06[84]
CPD-271791	3.69±0.09	23.8± 1.6[126]	8.8± 0.4	37[88]	2.641[88]	–	>3.9[88]	<-4.81[6]
HD3360	3.82±0.06	20.8± 0.2[103]	8.6± 0.1	19[92]	5.370[27]	82^{+1}_{-1}	$0.15^{+0.02}_{-0.02}$[106]	<-7.74[84]
HD5737	3.33±0.16	13.9± 0.4[41]	5.0± 0.4	17[105]	21.7[25]	73^{+6}_{-7}	$1.8^{+0.2}_{-0.3}$[4,10,21,126]	<-6.43[6]
HD11503^{f}	1.52±0.03	10.1± 0.2[101]	2.35± 0.03	54[101]	1.610[102]	84^{+4}_{-37}	$2.3^{+3.7}_{-0.7}$[102]	-7.85±0.06[14,126]
HD12447	1.73±0.06	10.0± 0.2[101]	2.49± 0.05	70[101]	1.491[102]	87^{+1}_{-9}	$1.7^{+0.5}_{-0.4}$[102,126]	-7.41±0.06[34]
HD12767	2.43±0.15	13.0± 0.3[41]	4.0± 0.1	40[32]	1.892[25]	89^{+0}_{-3}	$2.0^{+0.5}_{-0.6}$[9,112,126]	<-6.74[124]
HD19832	2.08±0.16	12.4± 0.4[41]	3.3± 0.1	160[95]	0.728[110]	89^{+0}_{-3}	$2.7^{+0.6}_{-0.3}$[110]	-6.67±0.06[34]
HD21699^{mr}	2.78±0.04	16.0± 0.1[41]	4.7± 0.2	35[105]	2.492[25,126]	78^{+2}_{-2}	$2.8^{+0.5}_{-0.1}$[5,126]	<-6.46[6]
HD22470	2.43±0.13	13.8± 0.3[41]	3.8± 0.2	62[32]	1.929[110]	87^{+1}_{-2}	$7.5^{+1.2}_{-0.5}$[110]	<-6.98[6]
HD22920^{mr}	2.64±0.12	13.6± 0.2[66]	4.2± 0.1	34[32]	3.947[22,126]	28^{+6}_{-7}	$1.6^{+1.1}_{-0.0}$[4,126]	<-6.86[124]
HD25267	2.32±0.03	12.6± 0.2[115]	3.5± 0.2	20[101]	3.823[115]	17^{+7}_{-8}	$1.0^{+0.1}_{-0.1}$[115]	<-7.13[124]
HD27309	1.88±0.02	11.2± 0.3[101]	2.81± 0.04	56[101]	1.569[102]	3^{+5}_{-3}	$1.9^{+2.6}_{-0.6}$[102]	-7.20±0.06[34]
HD28843^{mr}	2.51±0.07	14.8± 0.2[41]	4.20± 0.06	91[126]	1.374[25,126]	87^{+1}_{-5}	$0.93^{+0.30}_{-0.24}$[4,126]	<-6.78[6]
HD32633	1.94±0.12	12.5± 0.5[86]	3.50± 0.09	25[95]	6.430[20]	76^{+3}_{-3}	17^{+1}_{-2}[56,72]	<-6.71[14]
HD34452	2.45±0.27	13.8± 0.8[41]	4.2± 0.1	53[95]	2.469[25]	35^{+13}_{-16}	$3.6^{+1.1}_{-1.4}$[3,15,126]	-6.70±0.06[6,14]
HD35298	2.40±0.14	15.8± 0.8[103]	4.3± 0.2	60[92]	1.855[92]	77^{+2}_{-2}	10^{+0}_{-0}[106]	-5.32±0.06[14,31,34]
HD35456	2.88±0.29	13.5± 1.4[126]	4.1± 0.5	22[76]	4.951[76]	15^{+9}_{-11}	$2.2^{+0.2}_{-0.3}$[76,126]	<-6.20[124]
HD35502^{f}	2.95±0.12	18.4± 0.6[103]	5.8± 0.2	78[92]	0.854[77]	70^{+1}_{-1}	$7.3^{+0.4}_{-0.3}$[106]	-5.05±0.06[34,126]
HD35575^{r}	3.11±0.09	16.7± 1.3[126]	5.8± 0.3	150[98]	0.984[126]	–	<1.3[98,126]	<-7.09[17]
HD36313^{r}	2.04±0.19	13.0± 0.5[113]	3.4± 0.2	160[113]	0.589[113,126]	88^{+1}_{-5}	$9.0^{+1.8}_{-1.3}$[113,126]	-6.11±0.06[34]
HD36429^{mr}	2.42±0.02	13.8± 0.1[126]	3.87± 0.03	77[126]	15.6[126]	–	<0.20[28,126]	<-6.18[124]
HD36485	3.10±0.20	20.0± 2.0[103]	6.3± 0.2	33[92]	1.478[46]	3^{+1}_{-1}	$8.8^{+0.2}_{-0.1}$[106]	-5.45±0.06[6,14,31,71]
HD36526^{f}	2.30±0.24	15.0± 2.0[103]	4.3± 0.2	59[92]	1.542[92]	56^{+1}_{-2}	11^{+0}_{-0}[106]	<-6.42[14,126]
HD36540^{mr}	2.73±0.15	14.9± 0.7[86]	4.54± 0.09	80[82]	2.173[126]	9^{+26}_{-8}	$1.4^{+3.2}_{-0.1}$[82,126]	<-6.08[124]
HD36668^{mr}	2.40±0.19	13.5± 0.2[113]	3.81± 0.05	60[113]	2.119[113,126]	80^{+5}_{-6}	$4.5^{+2.3}_{-2.7}$[113,126]	<-5.97[124]
HD36916^{mr}	2.10±0.20	14.7± 0.2[82]	4.2± 0.1	78[82]	1.565[82,126]	30^{+8}_{-10}	$3.4^{+3.3}_{-0.2}$[4,65,82,90,107,126]	<-6.85[14,17]
HD37017	3.42±0.25	21.0± 2.0[103]	8.4± 0.5	134[92]	0.901[92]	56^{+2}_{-3}	$6.0^{+0.8}_{-0.6}$[106]	-5.10±0.06[6,14,18,31,71,8
HD37058	2.90±0.11	18.6± 0.6[103]	5.8± 0.2	11[92]	14.6[92]	55^{+11}_{-13}	$2.6^{+2.5}_{-0.1}$[106]	<-5.98[14]
HD37061^{f}	3.30±0.30	22.0± 1.0[103]	7.7± 0.4	100[92]	1.095[100]	59^{+4}_{-4}	$9.2^{+0.6}_{-0.6}$[106]	-5.69±0.06[81,126]
HD37140^{mr}	2.12±0.09	13.5± 0.2[113]	3.46± 0.05	25[126]	2.761[113,126]	80^{+3}_{-4}	$3.9^{+0.7}_{-0.4}$[113,126]	<-6.12[124]
HD37151	2.08±0.08	13.5± 0.9[126]	3.4± 0.2	–	–	87^{+1}_{-12}	$1.4^{+1.2}_{-1.4}$[114,126]	<-6.42[124]
HD37210^{mr}	2.51±0.05	13.5± 0.6[126]	3.92± 0.09	20[114]	11.0[22,126]	78^{+7}_{-8}	$1.8^{+0.9}_{-0.1}$[64,114,126]	<-5.73[124]
HD37479	3.51±0.21	23.0± 2.0[103]	7.9± 0.2	145[92]	1.191[45]	37^{+7}_{-10}	10^{+11}_{-0}[70]	-4.73±0.06[6,14,18,31,71]
HD37642^{mr}	2.42±0.10	16.0± 0.5[114]	4.3± 0.1	85[114]	1.079[114,126]	74^{+3}_{-3}	18^{+1}_{-0}[114,126]	-5.71±0.06[34]
HD37752	2.63±0.14	15.0± 0.7[41]	4.5± 0.2	35[32]	1.305[86]	–	<2.4[28]	<-7.00[17]
HD37776^{f}	3.30±0.15	22.0± 1.0[103]	8.3± 0.3	101[92]	1.539[80]	47^{+8}_{-10}	$5.8^{+0.6}_{-0.4}$[52,106]	<-6.32[6,126]
HD37808^{mr}	2.28±0.10	14.5± 0.2[114]	3.90± 0.08	30[95]	1.099[108,114,126]	45^{+20}_{-24}	$3.2^{+1.0}_{-0.3}$[114,126]	-6.15±0.06[17,31]
HD40312	2.33±0.01	10.2± 0.1[101]	3.11± 0.06	55[95]	3.619[102]	68^{+13}_{-15}	$1.3^{+0.4}_{-0.2}$[96]	-7.66±0.06[14]
HD43819	2.15±0.20	10.9± 0.4[38]	3.1± 0.2	10[38]	15.0[38]	47^{+16}_{-19}	$2.6^{+75.7}_{-0.1}$[38]	<-6.78[17]
HD45583	2.07±0.12	13.3± 0.3[42]	3.35± 0.09	70[95]	1.177[110]	69^{+2}_{-2}	$9.1^{+0.3}_{-0.3}$[110]	-6.24±0.06[34,123]
HD46328	4.49±0.11	27.0± 1.0[103]	14.4± 0.8	8[92]	30.0 (yr)[87,94,119]	89^{+0}_{-9}	$1.2^{+2.4}_{-0.0}$[106]	<-7.03[84]
HD47777	3.42±0.15	22.0± 1.0[103]	7.9± 0.4	60[92]	2.640[59]	82^{+5}_{-5}	$3.2^{+0.6}_{-0.5}$[106]	<-6.33[84]
HD49333	2.73±0.04	15.8± 0.1[41]	4.8± 0.3	65[32]	2.180[25]	85^{+3}_{-12}	$3.6^{+1.0}_{-1.2}$[15,126]	<-6.61[14]
HD49606^{mr}	2.59±0.06	13.5± 0.1[41]	4.08± 0.06	19[95]	8.546[122]	–	<0.040[126]	<-6.30[124]

Table A1 – *continued*

Star	$\log \frac{L_{\rm bol}}{L_\odot}$	$\frac{T_{\rm eff}}{\rm kK}$	$\frac{M_*}{\rm M_\odot}$	$\frac{v \sin i}{\rm km\ s^{-1}}$	$\frac{P_{\rm rot}}{\rm d}$	$\frac{\beta}{\rm deg}$	$\frac{B_{\rm d}}{\rm kG}$	$\log \frac{L_{\rm rad}}{\rm L_\odot}$
HD51418^{mr}	1.80±0.04	9.5± 0.8[99]	2.48± 0.09	28[83]	5.431[112,126]	89^{+0}_{-0}	$3.5^{+1.0}_{-0.4}$[83,126]	<-6.74[124]
HD58260	3.22±0.26	19.3± 1.3[103]	6.2± 0.5	3[92]	–	–	>8.8[106]	<-6.84[6,84]
HD60344^{r}	3.58±0.09	21.0± 0.3[41]	7.9± 0.2	55[105]	–	–	>1.2[88,126]	<-4.83[6]
HD61556^{f}	3.12±0.24	18.5± 0.8[69]	6.1± 0.3	58[69]	1.909[69]	58^{+6}_{-7}	$2.8^{+0.3}_{-0.3}$[106]	-5.99±0.06[116,126]
HD64740^{f}	3.81±0.15	24.5± 1.0[103]	10.1± 0.5	135[92]	1.330[92]	71^{+5}_{-5}	$3.0^{+0.4}_{-0.5}$[106]	-7.16±0.06[126]
HD65339	1.45±0.02	8.5± 0.1[101]	2.09± 0.02	13[95]	8.027[102]	89^{+0}_{-1}	15^{+2}_{-1}[30]	<-7.49[6,14]
HD66665	4.69±0.23	28.5± 1.0[103]	15.9± 1.1	8[92]	24.5[92]	75^{+3}_{-3}	$0.58^{+0.09}_{-0.04}$[106]	<-4.53[84]
HD66765^{f}	3.44±0.24	20.0± 2.0[61]	7.2± 0.6	58[92]	1.608[92]	73^{+5}_{-5}	$2.8^{+0.5}_{-0.4}$[106]	<-6.16[126]
HD79158	2.61±0.06	13.3± 0.1[41]	4.3± 0.1	49[95]	3.835[91]	87^{+1}_{-4}	$3.1^{+0.4}_{-0.4}$[91]	-6.54±0.06[6,34]
HD90044	1.66±0.10	10.0± 0.2[86]	2.8± 0.3	23[101]	4.379[25]	89^{+0}_{-0}	$4.4^{+1.2}_{-1.5}$[15,24,126]	<-7.75[17]
HD105382	3.04±0.16	18.0± 0.5[26]	5.8± 0.2	74[92]	1.295[26]	51^{+7}_{-8}	$2.6^{+0.1}_{-0.1}$[106]	-6.06±0.06[116]
HD112413	1.97±0.02	11.3± 0.2[101]	2.93± 0.03	15[95]	5.469[102]	88^{+1}_{-8}	$3.5^{+0.8}_{-0.2}$[62,63]	-8.15±0.06[6,34]
HD118022	1.53±0.04	9.4± 0.1[101]	2.26± 0.02	12[101]	3.722[102]	65^{+15}_{-17}	$3.2^{+8.0}_{-0.2}$[102]	-7.42±0.06[120]
HD122532	2.37±0.12	11.9± 0.5[86]	2.99± 0.04	–	3.681[12]	89^{+0}_{-3}	$3.0^{+0.7}_{-0.9}$[7,13,15,112,126]	<-6.98[14]
HD124224	1.93±0.01	12.3± 0.2[101]	3.02± 0.01	169[101]	0.521[80]	87^{+2}_{-11}	$4.0^{+0.3}_{-0.2}$[60]	-6.24±0.06[17,18,31,34,116,121]
HD125248	1.39±0.23	9.7± 0.3[41]	2.42± 0.07	11[95]	9.300[39]	89^{+0}_{-3}	$9.0^{+1.1}_{-1.3}$[74]	<-7.17[124]
HD125823	3.16±0.20	19.0± 2.0[103]	5.9± 0.2	16[92]	8.817[92]	75^{+4}_{-6}	$1.8^{+0.2}_{-0.1}$[106]	<-6.59[6]
HD126515	1.36±0.16	8.9± 0.2[126]	2.65± 0.07	16[126]	129.9[23]	84^{+4}_{-13}	13^{+1}_{-0}[23]	<-7.13[14]
HD131120^{mr}	3.15±0.09	19.4± 1.5[126]	6.3± 0.3	57[32]	1.569[53,126]	–	<0.17[64]	<-6.95[14]
HD133029^{mr}	1.98±0.08	11.8± 0.9[41]	2.8± 0.1	30[32]	2.888[43,126]	12^{+4}_{-4}	$9.0^{+5.0}_{-0.3}$[3,126]	<-6.84[14]
HD133652	2.02±0.10	12.8± 0.5[86]	3.27± 0.09	48[95]	2.304[25]	65^{+8}_{-11}	$7.6^{+0.8}_{-1.0}$[15,126]	-7.13±0.06[34]
HD133880	1.73±0.06	10.7± 0.1[41]	3.08± 0.08	103[95]	0.877[79]	83^{+1}_{-1}	12^{+0}_{-1}[79]	-5.44±0.06[71,34]
HD135679^{mr}	2.46±0.19	15.1± 2.8[126]	2.86± 0.06	1[83]	5.321[126]	14^{+6}_{-8}	$4.4^{+9.3}_{-0.2}$[83,90,126]	<-7.03[17]
HD137193^{mr}	1.91±0.13	10.6± 0.7[86]	3.5± 0.2	–	4.867[126]	0^{+25}_{-0}	$3.5^{+16.1}_{-0.5}$[8,126]	<-6.42[14]
HD137909	1.46±0.01	7.5± 0.1[101]	1.98± 0.03	3[95]	18.5[102]	89^{+0}_{-2}	$5.2^{+7.1}_{-1.0}$[102,126]	<-7.86[6]
HD138764	2.62±0.17	15.7± 2.7[126]	4.3± 0.4	19[32]	1.259[86]	–	<0.049[44]	<-7.60[17]
HD142184	2.85±0.13	18.5± 0.5[103]	5.7± 0.1	288[92]	0.508[54]	8^{+3}_{-3}	$8.9^{+2.9}_{-0.4}$[106]	-4.25±0.06[93,116]
HD142301	2.56±0.07	15.9± 0.2[41]	4.46± 0.05	78[32]	1.459[110]	47^{+9}_{-11}	12^{+9}_{-0}[110]	-5.62±0.06[14,17,18,31]
HD142884^{mr}	2.17±0.12	14.3± 0.5[86]	3.7± 0.1	130[32]	0.803[108]	–	<0.75[4,126]	<-6.93[14]
HD142990	2.93±0.13	18.0± 0.5[103]	5.6± 0.2	122[92]	0.979[104]	83^{+2}_{-3}	$4.6^{+0.3}_{-0.3}$[106]	-5.76±0.06[14,17,18,31,97]
HD143473	1.87±0.10	12.4± 1.0[86]	2.25± 0.08	25[32]	2.843[25]	18^{+5}_{-6}	18^{+2}_{-2}[13,15,126]	-6.56±0.06[34]
HD143699^{mr}	2.65±0.12	15.5± 0.4[41]	4.6± 0.2	115[126]	1.323[126]	–	<0.60[4,37,126]	-7.09±0.06[14,124]
HD144334	2.34±0.12	14.8± 0.4[41]	4.0± 0.1	82[32]	1.495[110]	55^{+7}_{-8}	$3.6^{+0.3}_{-0.3}$[110]	-6.62±0.06[14,17,31]
HD145102	2.02±0.12	10.8± 0.5[86]	3.0± 0.1	84[32]	1.418[55]	–	<0.98[8]	<-6.94[124]
HD145482^{r}	3.59±0.17	24.2± 4.3[126]	8.1± 0.8	166[32]	5.804[126]	–	<0.38[8]	<-7.05[14]
HD145501C	2.46±0.15	14.5± 0.5[86]	4.0± 0.2	70[32]	1.026[110]	89^{+0}_{-2}	$5.8^{+0.3}_{-0.3}$[110]	-6.08±0.06[14,17,123]
HD146001^{mr}	2.38±0.14	13.8± 0.3[41]	3.61± 0.06	90[32]	0.586[55]	–	<0.50[4,126]	-6.70±0.06[14]
HD147010	1.65±0.08	12.5± 0.6[86]	2.45± 0.09	15[95]	3.921[58]	10^{+4}_{-5}	19^{+0}_{-0}[19,112,126]	<-7.06[14]
HD147890	2.43±0.12	11.3± 0.5[86]	3.7± 0.2	65[32]	4.336[55]	–	<0.90[8]	<-6.24[124]
HD147932	2.50±0.20	17.0± 1.0[110]	4.8± 0.3	140[50]	0.864[89]	0^{+6}_{-0}	$7.6^{+9.6}_{-0.5}$[110,125]	-5.13±0.06[111]
HD147933	3.30±0.17	20.8± 0.5[109]	7.3± 0.2	200[109]	0.747[109]	75^{+9}_{-11}	$4.7^{+0.5}_{-0.4}$[109,125]	-5.53±0.06[109]
HD148112	1.85±0.02	9.2± 0.1[101]	2.52± 0.01	44[38]	3.044[102]	0^{+9}_{-0}	$0.76^{+0.41}_{-0.11}$[102,126]	<-7.15[6]
HD148199	1.88±0.12	11.7± 0.7[86]	2.5± 0.1	15[32]	7.726[25]	63^{+9}_{-12}	$5.0^{+0.6}_{-0.7}$[8,15,126]	<-6.54[14]
HD149438	4.47±0.13	32.0± 1.0[103]	17.5± 0.9	7[92]	41.0[35]	75^{+7}_{-8}	$0.31^{+0.10}_{-0.01}$[73]	<-7.93[84]
HD149822^{mr}	1.85±0.18	10.8± 0.3[41]	2.7± 0.2	60[32]	1.966[126]	87^{+2}_{-3}	$4.0^{+2.1}_{-1.1}$[16,36,64,126]	<-7.38[17]

Table A1 – *continued*

Star	$\log \frac{L_{\rm bol}}{L_\odot}$	$\frac{T_{\rm eff}}{\rm kK}$	$\frac{M_*}{\rm M_\odot}$	$\frac{v \sin i}{\rm km\ s^{-1}}$	$\frac{P_{\rm rot}}{\rm d}$	$\frac{\beta}{\rm deg}$	$\frac{B_{\rm d}}{\rm kG}$	$\log \frac{L_{\rm rad}}{\rm L_\odot}$
HD151346	2.44±0.17	13.7± 1.1[86]	3.8± 0.2	46[32]	2.180[86]	–	<1.7[4]	<-6.64[14]
HD152107	1.47±0.01	8.8± 0.1[101]	2.15± 0.01	21[101]	3.857[102]	19^{+4}_{-5}	$4.2^{+0.5}_{-0.2}$[102,126]	<-7.98[6,14]
HD156424	3.00±0.40	18.0± 3.0[118]	4.6± 0.3	7[92]	0.524[118]	39^{+18}_{-21}	$8.0^{+12.0}_{-2.0}$[118]	-4.83±0.06[84]
HD163472	3.81±0.10	25.2± 1.1[103]	10.3± 0.5	62[92]	3.639[29]	46^{+13}_{-14}	$1.1^{+1.3}_{-0.2}$[106]	<-6.63[84]
HD164429^{mr}	1.85±0.04	12.0± 0.5[126]	2.99± 0.06	90[32]	1.082[126]	88^{+1}_{-12}	$3.0^{+0.7}_{-0.3}$[15,126]	-6.91±0.06[17,34]
HD165474	2.06±0.26	13.2± 3.4[126]	1.82± 0.08	18[32]	9.0 (yr)[78]	89^{+0}_{-0}	$3.0^{+4.9}_{-1.8}$[78,126]	<-7.05[124]
HD168785^{r}	3.48±0.08	23.0± 1.2[126]	8.1± 0.4	14[105]	–	–	>4.0[88]	<-5.26[124]
HD168856^{mr}	2.10±0.09	11.9± 1.2[126]	3.0± 0.1	73[75]	2.428[108]	55^{+15}_{-16}	$3.5^{+3.7}_{-0.6}$[75,83,33,126]	<-6.67[124]
HD170000	2.36±0.01	11.6± 0.0[101]	3.47± 0.02	83[101]	1.716[102]	70^{+10}_{-12}	$1.8^{+0.0}_{-0.1}$[102]	-7.11±0.06[34]
HD170973^{mr}	2.32±0.13	10.8± 0.2[41]	3.39± 0.06	4[95]	18.1[126]	83^{+2}_{-3}	$4.8^{+11.2}_{-0.5}$[15,13,126]	<-6.65[124]
HD171247^{mr}	2.79±0.16	12.2± 0.3[41]	4.0± 0.2	68[95]	3.910[126]	85^{+3}_{-34}	$4.1^{+3.1}_{-0.4}$[126]	-5.17±0.06[17,31]
HD175132^{r}	2.78±0.04	13.2± 0.5[126]	4.0± 0.2	40[32]	8.030[126]	–	>3.5[28]	<-6.71[17,124]
HD175362	2.64±0.12	17.6± 0.4[103]	5.3± 0.2	34[92]	3.674[92]	68^{+5}_{-6}	17^{+3}_{-0}[106]	-6.73±0.06[14,17,18]
HD176582	2.90±0.15	17.0± 1.0[103]	5.6± 0.2	103[92]	1.582[51]	89^{+0}_{-1}	$5.4^{+0.1}_{-0.1}$[106]	-6.08±0.06[34]
HD177003	3.05±0.10	17.7± 0.7[86]	5.7± 0.2	12[32]	1.800[86]	–	<0.81[28]	<-7.10[17]
HD177410	2.30±0.10	13.4± 0.5[86]	3.7± 0.1	211[105]	1.123[86]	–	<1.4[15,67]	<-7.18[17]
HD179527	2.63±0.16	10.4± 0.3[38]	3.39± 0.05	33[38]	7.098[38]	88^{+1}_{-12}	$0.52^{+0.71}_{-0.11}$[38]	<-6.47[124]
HD182180^{f}	3.09±0.18	19.8± 1.4[103]	6.5± 0.2	306[92]	0.521[48,47]	81^{+3}_{-4}	$9.6^{+0.6}_{-0.3}$[106]	-4.65±0.06[85,126]
HD183056	2.69±0.11	11.7± 0.4[38]	4.0± 0.2	35[95]	2.992[38]	82^{+3}_{-4}	$1.6^{+2.4}_{-0.4}$[38]	<-7.12[17]
HD183339^{r}	2.70±0.05	14.0± 0.6[126]	4.3± 0.1	41[32]	4.204[126]	–	>4.5[28]	<-6.34[124]
HD184927	3.59±0.16	22.0± 1.0[103]	8.4± 0.5	8[92]	9.531[68]	67^{+3}_{-4}	$8.8^{+1.4}_{-0.5}$[68]	<-6.05[17,124]
HD186205	3.84±0.25	19.6± 0.8[103]	8.3± 0.6	6[92]	37.2[92]	7^{+3}_{-4}	$2.9^{+4.0}_{-0.1}$[106]	<-4.78[124]
HD187474	1.76±0.03	9.9± 0.1[101]	2.52± 0.02	0[95]	6.4 (yr)[102]	89^{+0}_{-3}	$7.2^{+2.1}_{-0.2}$[102]	<-7.18[124]
HD188041^{mr}	1.40±0.01	8.5± 0.1[101]	2.07± 0.04	4[95]	224.0[102]	0^{+25}_{-0}	$4.1^{+16.6}_{-0.4}$[102,126]	<-7.57[124]
HD192678	1.65±0.27	9.0± 0.1[41]	2.5± 0.2	6[126]	12.9[23]	25^{+11}_{-12}	$5.5^{+4.4}_{-0.1}$[23,126]	<-6.74[124]
HD196178^{mr}	2.15±0.10	13.1± 0.5[86]	4.2± 0.2	50[32]	1.101[126]	41^{+7}_{-9}	$3.9^{+0.4}_{-0.2}$[3,126]	-5.97±0.06[34]
HD196502	2.01±0.39	8.9± 0.4[41]	2.55± 0.05	9[95]	20.3[25]	88^{+1}_{-12}	$1.7^{+0.3}_{-0.3}$[1,2,11,112,126]	<-6.47[6]
HD202671	2.70±0.07	13.2± 0.1[41]	4.0± 0.2	20[95]	1.992[86]	–	<0.056[49]	<-6.94[124]
HD205021	4.26±0.11	25.0± 1.0[103]	11.9± 1.1	34[92]	12.0[57]	86^{+2}_{-4}	$0.27^{+0.03}_{-0.01}$[106]	<-7.43[84]
HD208057^{f}	3.01±0.11	16.5± 1.2[103]	5.3± 0.3	105[92]	1.368[92]	89^{+0}_{-0}	$0.55^{+0.15}_{-0.16}$[106]	<-7.38[126]
HD215441	2.31±0.09	14.5± 0.4[41]	3.9± 0.1	5[95]	9.490[23]	37^{+7}_{-7}	62^{+6}_{-3}[23]	-5.14±0.06[6,14,18,31,71]
HD224801	2.19±0.10	11.9± 0.5[86]	3.2± 0.1	30[32]	3.740[22]	–	>4.6[1]	<-6.68[124]
HD260858^{r}	3.52±0.27	18.0± 1.0[41]	6.7± 0.4	47[105]	–	–	>1.8[90]	<-4.84[6]
HD335238	1.62±0.23	9.4± 0.5[86]	2.25± 0.04	–	48.7[78]	85^{+4}_{-44}	$5.9^{+2.0}_{-2.5}$[78,107,126]	<-6.24[124]

Table A1 – *continued*

Star	$\log \frac{L_{\rm bol}}{L_\odot}$	$\frac{T_{\rm eff}}{\rm kK}$	$\frac{M_*}{\rm M_\odot}$	$\frac{v \sin i}{\rm km\ s^{-1}}$	$\frac{P_{\rm rot}}{\rm d}$	$\frac{\beta}{\rm deg}$	$\frac{B_{\rm d}}{\rm kG}$	$\log \frac{L_{\rm rad}}{\rm L_\odot}$

Table A1 – *continued*

Reference key:

1, Babcock (1958); 2, Wolff & Bonsack (1972); 3, Borra & Landstreet (1980); 4, Borra et al. (1983); 5, Brown et al. (1985); 6, Drake et al. (1987); 7, Bohlender et al. (1987); 8, Thompson et al. (1987); 9, Ruediger & Scholz (1988); 10, Shore & Brown (1990); 11, Weiss et al. (1990); 12, Lanz & Mathys (1991); 13, Mathys (1991a); 14, Linsky et al. (1992); 15, Bohlender et al. (1993a); 16, Bohlender et al. (1993b); 17, Leone et al. (1994); 18, Leone et al. (1996); 19, Mathys & Hubrig (1997a); 20, Adelman (1997); 21, Mathys & Hubrig (1997b); 22, Catalano & Renson (1998); 23, Landstreet & Mathys (2000); 24, Leone & Catanzaro (2001); 25, Renson & Catalano (2001); 26, Briquet et al. (2001); 27, Neiner et al. (2003a); 28, Bychkov et al. (2003); 29, Neiner et al. (2003b); 30, Kochukhov et al. (2004); 31, Leone et al. (2004); 32, Głębocki & Gnaciński (2005); 33, Hubrig et al. (2006); 34, Drake et al. (2006); 35, Donati et al. (2006); 36, Kudryavtsev et al. (2006); 37, Landstreet et al. (2007); 38, Aurière et al. (2007); 39, Hubrig et al. (2007); 40, Alecian et al. (2008); 41, Netopil et al. (2008); 42, Semenko et al. (2008); 43, Adelman (2008); 44, Silvester et al. (2009); 45, Townsend et al. (2010); 46, Leone et al. (2010); 47, Rivinius et al. (2010); 48, Oksala et al. (2010); 49, Makaganiuk et al. (2011); 50, Alecian et al. (2011); 51, Bohlender & Monin (2011); 52, Kochukhov et al. (2011); 53, Dubath et al. (2011); 54, Grunhut et al. (2012); 55, Wraight et al. (2012); 56, Silvester et al. (2012); 57, Henrichs et al. (2013); 58, Bailey & Landstreet (2013); 59, Fossati et al. (2014); 60, Kochukhov et al. (2014); 61, Alecian et al. (2014); 62, Silvester et al. (2014a); 63, Silvester et al. (2014b); 64, Bagnulo et al. (2015a); 65, Bagnulo et al. (2015b); 66, Khalack & LeBlanc (2015); 67, Romanyuk et al. (2015); 68, Yakunin et al. (2015); 69, Shultz et al. (2015); 70, Oksala et al. (2015a); 71, Chandra et al. (2015); 72, Silvester et al. (2015); 73, Kochukhov & Wade (2016); 74, Rusomarov et al. (2016); 75, Romanyuk et al. (2016b); 76, Romanyuk et al. (2016a); 77, Sikora et al. (2016); 78, Mathys (2017); 79, Kochukhov et al. (2017); 80, Mikulášek et al. (2017); 81, Kounkel et al. (2017); 82, Romanyuk et al. (2017a); 83, Romanyuk et al. (2017b); 84, Kurapati et al. (2017); 85, Leto et al. (2017); 86, Netopil et al. (2017); 87, Shultz et al. (2017); 88, Järvinen et al. (2018); 89, Rebull et al. (2018); 90, Romanyuk et al. (2018); 91, Oksala et al. (2018); 92, Shultz et al. (2018b); 93, Leto et al. (2018); 94, Shultz et al. (2018c); 95, Ghazaryan et al. (2018); 96, Kochukhov et al. (2019); 97, Das et al. (2019b); 98, Romanyuk et al. (2019); 99, Moiseeva et al. (2019); 100, Shultz et al. (2019a); 101, Sikora et al. (2019a); 102, Sikora et al. (2019b); 103, Shultz et al. (2019b); 104, Shultz et al. (2019c); 105, Ghazaryan et al. (2019); 106, Shultz et al. (2019d); 107, Romanyuk et al. (2020); 108, Bernhard et al. (2020); 109, Leto et al. (2020a); 110, Shultz et al. (2020); 111, Leto et al. (2020b); 112, Bychkov et al. (2020); 113, Romanyuk et al. (2021a); 114, Romanyuk et al. (2021b); 115, Woodcock et al. (2021); 116, Pritchard et al. (2021); 117, Shultz et al. (2021a); 118, Shultz et al. (2021b); 119, Erba et al. (2021); 120, Leto et al. (2021); 121, Das & Chandra (2021); 122, Kochukhov et al. (2021); 123, Das et al., submitted; 124, Drake (priv. comm.); 125, Shultz et al., in prep.; 126, This Work .

APPENDIX B: NEW RADIO OBSERVATIONS

Table B1. New radio observations acquired with the uGMRT. HJD stands for Heliocentric Julian Date. 'Eff. band' is the effective frequency range of observation after the edges of the original frequency band were removed due to low gain. For the stars that were not detected, we report the 3σ upper limit. For the detected stars (in bold), the quoted uncertainty includes the fitting error, the map rms, and the uncertainty associated with the absolute flux density calibration (assumed to be 10% of the flux density).

Star	HJD range -2450000	Eff. band (MHz)	Flux calibrator	Phase calibrator	Flux density (mJy)
HD 11503	8439.26±0.18	570–804	3C48, 3C147	J0204+152	0.25 ± 0.01
HD 35502	8595.03±0.06	570–716	3C147, 3C286	J0607–085	0.64 ± 0.16
HD 36526	8231.00±0.04, 8242.86±0.05	560–726	3C48, 3C147	J0503+020, J0607–085	< 0.1
HD 37061	8608.90±0.10	570–804	3C48, 3C147	J0607–085	0.54 ± 0.14
HD 37776	8711.65±0.16	570–804	3C48, 3C286	J0607–085	< 0.1
HD 61556	8273.92±0.06	570–726	3C48	J0735–175	1.21±0.18
HD 64740	8602.02±0.07	570–794	3C48, 3C286	J0828–375	0.06 ± 0.01
HD 66765	8342.74±0.05, 8391.63±0.01	560–726	3C48, 3C286	J0828–375	< 0.1
HD 182180	8348.30±0.02	560–726	3C48	J1924–292	4.17 ± 0.07
HD 208057	8239.47±0.04	560–726	3C286	J2202+422	< 0.05

APPENDIX C: STARS WITH NEW ROTATIONAL AND MAGNETIC CONSTRAINTS

C1 Least-squares deconvolution

In order to maximize the signal-to-noise (S/N) of the Stokes V spectrum from the ESPaDOnS and Narval observations we used the standard multiline analyis technique least-squares deconvolution (LSD; Donati et al. 1997), specifically the ıLSD package (Kochukhov et al. 2010). LSD applies a line mask composed of the rest wavelengths of spectral lines expected for a given $T_{\rm eff}$ and $\log g$, their line depths, and their Landé factors, to the observed spectrum in order to extract a mean line profile. The line masks were obtained from the Vienna Atomic Line Database (VALD3; Piskunov et al. 1995; Ryabchikova et al. 1997; Kupka et al. 1999, 2000; Ryabchikova et al. 2015) using 'extract stellar' requests over the wavelength interval 370 nm to 1050 nm, for solar metallicity, effective temperatures from 10 kK to 25 kK in 1 kK intervals (with the closest $T_{\rm eff}$ to the measured value used for a given star), and $\log g = 4$. Since LSD relies on the assumption that all lines can be reproduced with a common line profile, the line masks were cleaned by removing H lines, strong He lines, metallic lines formed in the wings of these lines, as well as regions contaminated by telluric bands, interstellar lines as appropriate for a given star, and parts of the spectrum affected by instrumental ripples. The line masks were then 'tweaked' by hand such that the depths matched the observed depths of each star.

The results of the LSD profile analysis are summarized for each star in Table C1. Observations were classified as magnetic definite detections (DD), marginal detections (ND), or non-detections (ND) based upon the false alarm probabilities (FAPs) in Stokes V inside the line profile according to the usual criteria, i.e. an ND if FAP$> 10^{-3}$, MD if $< 10^{-5}$ FAP $< 10^{-3}$, and a DD if FAP $< 10^{-5}$ (Donati et al. 1992, 1997). These are summarized in Table C1. Out of the 20 stars analyzed, 5 yielded at least 1 DD, 1 yielded 2 MDs, and the remainder were NDs. All null N profiles yielded NDs, verifying normal instrument performance.

To quantify the strength of the magnetic field the line-of-sight magnetic field averaged over the stellar disk $\langle B_z \rangle$ was measured using the moment method (Mathys 1989). The same measurement was performed on the N profiles. Table C1 gives the root-mean-square of $\langle B_z \rangle$ and $\langle N_z \rangle$, the mean $\langle B_z \rangle$ error bar, and the maximum $\langle B_z \rangle$ value measured. Note that for stars for which only one observation was obtained, there is no distinction between the root-mean-square and maximum $\langle B_z \rangle$.

C2 Oblique rotator models

In order to determine the surface strength and geometry of the surface magnetic field, $\langle B_z \rangle$ measurements were folded with the rotation periods determined using photometric or magnetic data, and harmonic functions in the same method as that described by Shultz et al. (2018b). For this purpose $\langle B_z \rangle$ measurements found in the literature, DAO $\langle B_z \rangle$ measurements, and the LSD measurements described above were utilized as available. DAO measurements are summarized in Table C2. The fitting parameters B_0, B_1, and Φ_1, corresponding to the mean value of $\langle B_z \rangle$, the amplitude of the $\langle B_z \rangle$ sine wave, and the phase offset, are given in Table C3. In all but one case a pure sine wave gives an adequate description of $\langle B_z \rangle$, as evaluated by the reduced χ^2; the exception being HD 21699, which requires two additional harmonics. Table C3 also gives the rotational periods $P_{\rm rot}$ and zero points T_0 for the rotatational ephemerides, where the last number in brackets gives the uncertainty in the last significant digit. In most cases T_0 corresponds to magnetic maximum; when an insufficient number of $\langle B_z \rangle$ measurements were available to constrain this, maximum light was used instead.

The $\langle B_z \rangle$ fitting parameters were then used to determine the obliquity β and surface strength of the magnetic dipole $B_{\rm d}$ from the geometric relations developed by Preston (1967), following the same procedure as that described by Shultz et al. (2019d). In a few cases there were not enough $\langle B_z \rangle$ measurements to constrain a fit; in those cases B_0 and B_1 were approximated by the mean and standard deviation of $\langle B_z \rangle$.

C3 Notes on individual stars

In the following, the characteristics of the individual datasets for each star, and the particular considerations affecting its analysis, are briefly described.

ALS 8988: This is a magnetic Herbig Be star, with 4 $\langle B_z \rangle$ measurements published by Alecian et al. (2008), all negative and of approximately the same magnitude. The star is in a crowded field, and the *TESS* light curve (obtained in cycles 6 and 33) is certainly contaminated by multiple objects. The light curves in the two cycles do not resemble one another, and yield different sets of significant periods: in order of decreasing signal-to-noise, about 33 d, 3 d, and 8 d in the cycle 6 light curve, and 12.5 d, 6.3 d, 27.8 d, 4.3 d, ad 3.2 d in the cycle 33 light curve. The longer periods likely reflect systematics, while th shorter periods are not harmonically related. The rotation period cannot be determined.

HD 21699: This star is listed in the Renson & Manfroid (2009) catalogue as a B8 He-weak Si star. Bernhard et al. (2020) give a photometric period of 2.4928(2) d. There is a large ESPaDOnS dataset, with 26xDD (Fig. C1). The period from Bernhard et al. (2020) coherently phases the ESPaDOnS measurements, but not the full magnetic dataset. Period analysis of ESPaDOnS $\langle B_z \rangle$ measurments yields 2.49187(7) d, however this period does not coherently phase the ESPaDOnS measurements with the $\langle B_z \rangle$ measurements published by Brown et al. (1985), from which a period of 2.4928(9) d is obtained. A period search for the full magnetic dataset can approximately phase the data, but the phasing of the ESPaDOnS measurements is noticeably worse. The *Hipparcos* and TESS light curves respectively yield 2.493(4) d and 2.487(3) d; combining them gives 2.49208(2) d, however this considerably degrades the phasing of the ESPaDOnS data. We therefore revert to the ESPaDOnS period in Fig. C2. It is possible that the rotational period of this star may be variable. The ESPaDOnS $\langle B_z \rangle$ curve, which is much more precise that the Brown et al. (1985) measurements, is anharmonic, indicating that the surface field of this star is not a pure dipole.

HD 22920: This star is listed in the Renson & Manfroid (2009) catalogue as a B8 Si star. 3.95 d rotation period from Catalano & Renson (1998). Bernhard et al. (2020) provide

Table C1. Summary of Least-squares deconvolution analysis. The columns give the stellar designation, the number $N_{\rm ESP}$ of ESPaDOnS observations, $N_{\rm Nar}$ of Narval observations, the $T_{\rm eff}$ of the line mask, the number $N_{\rm lines}$ of lines in the mask used for analysis as a fraction of the total number of lines, the number of definite, marginal, and non-detections, the root-mean-square longitudinal magnetic field $B_{\rm rms}$, the root-mean-square null field $N_{\rm rms}$, the mean uncertainty $< \sigma_B >$, and the maximum longitudinal magnetic field $\langle B_z \rangle_{\rm max}$.

Star	$N_{\rm ESP}$	$N_{\rm Nar}$	$T_{\rm eff}$ (kK)	$N_{\rm lines}$	DD/MD/ND	$B_{\rm rms}$ (G)	$N_{\rm rms}$ (G)	$< \sigma_B >$ (G)	$\langle B_z \rangle_{\rm max}$ (G)
HD 21699	26	–	16	946/1203	26/0/0	431	11	19	697 ± 33
HD 22920	4	4	14	1284/2059	8/0/0	354	16	16	487 ± 23
HD 23408	2	1	13	1499/2379	0/0/3	5	12	13	-13 ± 17
HD 28843	–	11	15	1099/1799	0/2/9	162	77	95	-264 ± 119
HD 36429	1	–	14	309/561	0/0/1	120	59	67	120 ± 67
HD 36540	1	–	13	1498/2328	1/0/0	430	−94	59	430 ± 59
HD 36629	2	–	22	302/502	0/0/2	4	3	4	-6 ± 4
HD 36960	1	–	28	313/558	0/0/1	5	4	10	-5 ± 10
HD 37140	1	–	14	1315/2059	1/0/0	186	17	22	-186 ± 22
HD 49606	2	–	13	1513/2328	0/0/2	0	9	7	0 ± 7
HD 89822	4	1	10	616/1138	0/0/5	2	1	2	2 ± 3
HD 131120	1	–	19	247/389	0/0/1	77	19	54	77 ± 54
HD 142884	–	1	14	330/461	0/0/1	295	137	147	295 ± 147
HD 143699	1	–	18	250/462	0/0/1	78	57	77	78 ± 77
HD 144844	1	–	15	1288/1799	0/0/1	3	9	9	-3 ± 9
HD 146001	2	–	14	1287/2059	0/0/2	67	76	66	97 ± 66
HD 147084	2	–	10	623/1138	0/0/2	2	1	2	-2 ± 1
HD 162374	1	–	16	1014/1504	0/0/1	12	25	27	12 ± 27
HD 170973	3	–	10	623/1138	3/0/0	297	2	7	-431 ± 7
HD 207840	2	–	13	1663/2328	0/0/2	2	5	4	-3 ± 5

Table C2. Summary of DAO $\langle B_z \rangle$ measurements

Star	N	$B_{\rm rms}$ (G)	$< \sigma_B >$ (G)	$\langle B_z \rangle_{\rm max}$
HD 21699	29	453	157	-955 ± 106
HD 36668	7	1726	538	3363 ± 1048
HD 37642	13	2782	595	-5162 ± 307
HD 51418	2	350	125	-550 ± 157
HD 133029	25	2302	178	4056 ± 311
HD 135679	22	792	190	1546 ± 262
HD 164429	24	614	288	-1467 ± 409
HD 170973	15	412	115	768 ± 126
HD 171247	25	348	260	1179 ± 188
HD 184961	18	646	175	1212 ± 375
HD 188041	11	793	71	1292 ± 27
HD 196178	31	920	182	-1470 ± 422

a photometric period of 3.9489(3) d. The *TESS* light curve gives a 3.956(3) d period; combining it with *Hipparcos* yields 3.94724(1) d. All 8 ESPaDOnS observations are definite detections (Fig. C1). This period gives a good phasing of the ESPaDOnS and Narval data; while it does not quite phase the modern measurements with the measurements published by Borra et al. (1983), the latter have large uncertainties. The photometric and magnetic data are shown in Fig. C3.

HD 23408: This star is listed in the Renson & Manfroid (2009) catalogue as a B7 He-weak Mn star. No magnetic field was detected in the FORS observation by Bagnulo et al. (2015a), with a 64 G error bar. There are 3 ESPaDOnS measurements, all non-detections, with the smallest error bar of 5 G (Fig. C1). There are no obviously significant periodicities in the *Hipparcos* or *K2* light curves. This is not a magnetic star.

HD 28843: This star is listed in the Renson & Manfroid (2009) catalogue as a B9 He-weak Si star. Bychkov et al. (2005) inferred the $\langle B_z \rangle$ curve from only 5 measurements from Borra et al. (1983), using the 1.37 d period from Mathys et al. (1986). There are 11 Narval observations (Fig. C1), two yielding marginal detections and the remainder non-detections, with a mean error bar of 95 G. The 1.37 d periodicity is absolutely unambiguous in the *Hipparcos* light curve, and the $\langle B_z \rangle$ measurements phase coherently with this period. The same is true of the TESS light curve, although there are large-scale variations in the amplitude of the TESS light curve (see the bottom panel of Fig. C4) which appear to be real and require further analysis to determine their origin. The evidence suggests either that this is a rapidly rotating star with a weak magnetic field, or that the period is related to pulsation.

HD 35575: This star is listed in the Renson & Manfroid (2009) catalogue as a B3 He-weak star. The *TESS* light curve was obtained in sector 6. Despite some systematics, there is clear rotational modulation at 0.9841(2) d, with several harmonics of the rotational frequency present. The light curve is shown folded with the rotation period in Fig. C5. This is consistent with the star's large $v \sin i = 150$ km s^{-1} (Romanyuk et al. 2019). Four magnetic measurements were reported by Romanyuk et al. (2019), all non-detections, however as can be seen in Fig. C5 they were all acquired at a similar rotation phase; it is possible that observation at other phases may successfully detect the field.

HD 36313: Romanyuk et al. (2021a) obtained several $\langle B_z \rangle$ measurements from this SB2 star, and determined a rotation period of 0.58913 d from the TESS light curve. They noted that the magnetic field could only be detected in H lines, due to contamination of the low-resolution spectra by the non-magnetic secondary. The TESS period does

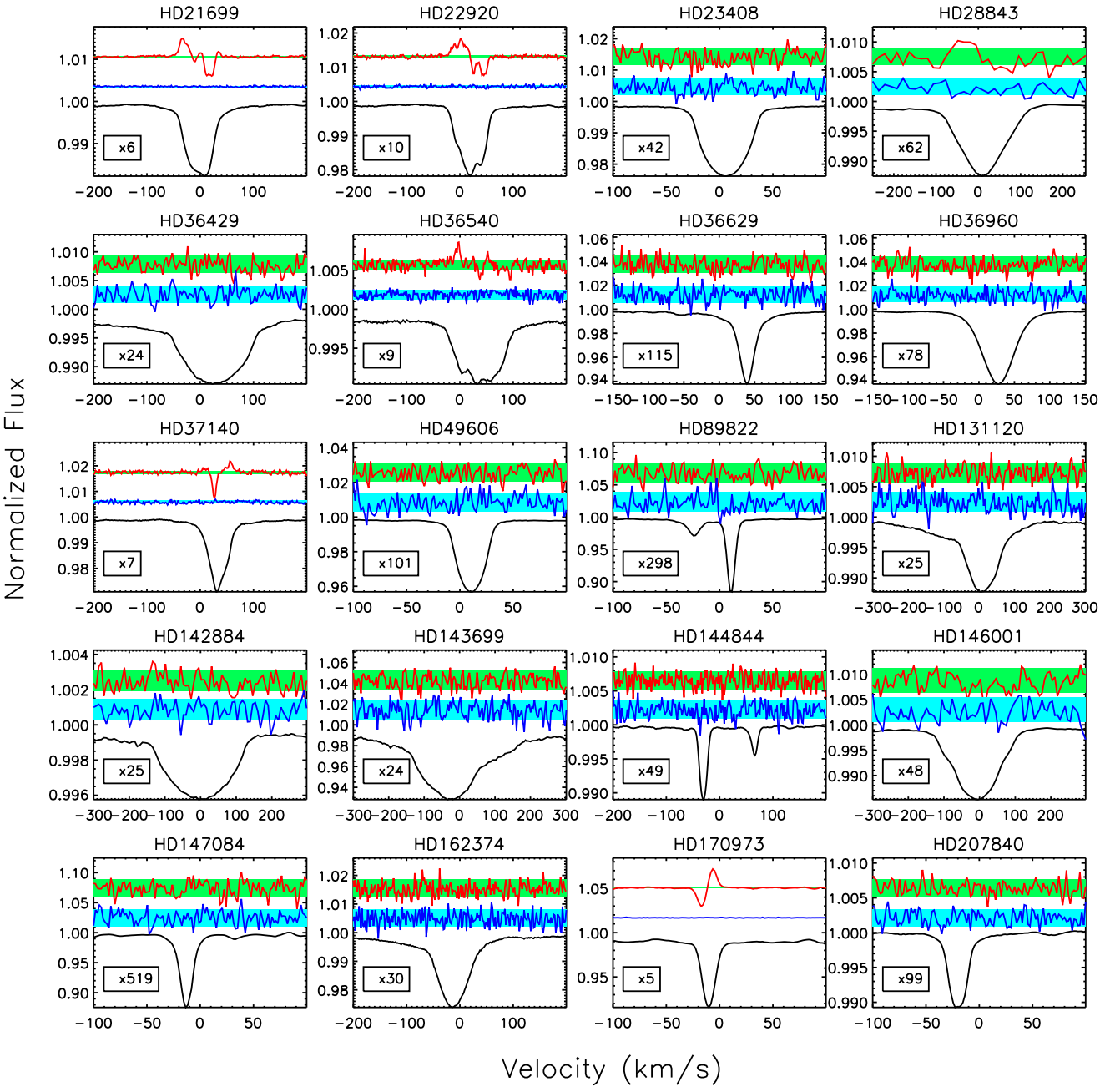

Figure C1. LSD profiles extracted from ESPaDOnS and Narval observations. Each panel shows Stokes I (black, bottom), N (blue, middle), Stokes V (red, top). Blue and green shaded regions show the mean error bars for N and Stokes V, respectively. Box gives the amplification factor for N and Stokes V.

not phase the $\langle B_z \rangle$ measurements. Romanyuk et al. (2021a) noted the presence of other periods in the light curve, which they attributed to the rotation period of the cooler secondary; this periodicity appears to be only marginally significant. The light curve contains 11 harmonics of the rotational frequency; simultaneous fitting of the rotational frequency and all harmonics yields 0.58921(1) d, which still does not provide a coherent phasing of $\langle B_z \rangle$. The closest period that provides an acceptable phasing is 0.58884(2) d, which is used to phase the Romanyuk et al. (2021a) and DAO $\langle B_z \rangle$ measurements in Fig. C6. While this period is well outside the formal uncertainties from period analysis of the TESS data, it provides an almost equivalently good phasing of the photometry as determined by eye. This start should certainly be followed up with high-resolution spectropolarimetry in order to evaluate the accuracy of the existing magnetic data in light of the star's binarity.

HD 36429: This star is listed in the Renson & Manfroid

Table C3. New and revised rotation periods and $\langle B_z \rangle$ fitting parameters. Periods with an asterisk may not be related to rotation. Superscripts b and p respectively indicate that T_0 is defined by $\langle B_z \rangle_{\max}$ and maximum light.

Star	$P_{\rm rot}$ (d)	T_0 −2400000	B_0 (kG)	B_1 (kG)	Φ_1 (rad)
HD 21699	2.49187(7)	55170.8(1)^b	0.158 ± 0.005	0.614 ± 0.006	1.91 ± 0.01
HD 22920	3.9472(1)	56556.7(1)^p	0.312 ± 0.009	0.19 ± 0.01	1.47 ± 0.06
HD 28843	1.37382(6)	47908.54(4)^b	0.01 ± 0.04	0.19 ± 0.06	2.0 ± 0.3
HD 35575	0.9841(2)	58467.55(1)^p	0.08 ± 0.08	0.15 ± 0.06	0.23 ± 0.21
HD 36313	0.58884(2)	58468.608(2)^p	-0.1 ± 0.4	1.7 ± 0.6	1.5 ± 0.3
HD 36429	15.6(7)*	58471.2(4)^p	–	–	–
HD 36540	2.1732(1)	58469.833(2)^p	0.09 ± 0.07	-0.3 ± 0.1	1.6 ± 0.4
HD 36668	2.1192(2)	58466.50(2)^p	0.0 ± 0.1	1.2 ± 0.1	1.7 ± 0.2
HD 36916	1.56548(8)	58467.186(7)^p	-0.53 ± 0.09	-0.49 ± 0.04	1.5 ± 0.3
HD 37140	2.7606(9)	55557.1(2)^b	-0.18 ± 0.05	-0.8 ± 0.1	1.52 ± 0.06
HD 37210	11.043(8)	52682.8(7)^b	0.07 ± 0.02	0.45 ± 0.04	1.55 ± 0.06
HD 37642	1.07876(1)	55582.75(7)^p	-1.2 ± 0.1	-3.9 ± 0.2	1.58 ± 0.06
HD 37808	1.098535(5)	58469.585(9)^p	1.2 ± 0.1	0.6 ± 0.2	2.9 ± 0.1
HD 51418	5.431(3)	58843.62(2)^p	-0.01 ± 0.03	-0.56 ± 0.03	1.53 ± 0.07
HD 89897	1.11037(5)	58545.434(3)^p	–	–	–
HD 131120	1.56873(1)	58598.552(4)^p	0.06 ± 0.03	0.04 ± 0.05	3 ± 1
HD 133029	2.88767(5)	54480.9(7)^b	2.23 ± 0.05	0.48 ± 0.07	1.26 ± 0.14
HD 135679	5.321(1)	55259(1)^b	0.78 ± 0.04	0.55 ± 0.05	1.72 ± 0.09
HD 137193	4.867(3)	59330(3)^p	0.6 ± 0.2	0.2 ± 0.4	0.4 ± 1.2
HD 143699	0.89421(5)*	58627.368(5)^p	–	–	–
HD 145482	5.804(2)	58628.09(1)^p	–	–	–
HD 149822	1.9661(1)	8982.72(8)^p	-0.09 ± 0.06	-0.69 ± 0.07	1.6 ± 0.1
HD 157779	3.2566(8)	58981.29(3)^p	–	–	–
HD 164429	1.081751(1)	54714.5(1)^b	-0.06 ± 0.06	-0.84 ± 0.07	1.5 ± 0.1
HD 168856	2.4277(1)	47992.2(5)^b	-0.30 ± 0.05	0.75 ± 0.09	0.8 ± 0.1
HD 170973	18.064(5)	46547(2)^b	0.22 ± 0.02	0.66 ± 0.02	1.62 ± 0.03
HD 171247	3.9098(8)	55077(1)^p	0.11 ± 0.08	0.3 ± 0.1	1.7 ± 0.3
HD 175132	8.0295(2)	58106.5(2)^p	–	–	–
HD 183339	4.2040(5)*	58682.10(6)^p	–	–	–
HD 184961	6.335(5)	55720(1)^b	0.65 ± 0.03	0.24 ± 0.05	1.4 ± 0.12
HD 188041	224.0(2)	46319.5(5)^b	0.82 ± 0.01	0.51 ± 0.02	1.68 ± 0.04
HD 196178	1.10111(1)	42592.6(2)^b	-0.94 ± 0.04	-0.20 ± 0.05	1.6 ± 0.3

(2009) catalogue as a B6 He-weak star. No magnetic field was detected by Borra (1981). There is one ESPaDOnS measurement, a non-detection with a 67 G error bar. The LSD Stokes I profile may be consistent with binarity (see Fig. C1). The *TESS* light curve is dominated by a 15.6(7) d period, which could be rotational but is clearly inconsistent with the large $v \sin i$ (77 km s^{-1}; Fig. C1) and is therefore related either to orbital motion or instrumental systematics. The light curve also demonstrates numerous high-frequency signals likely related to pulsation. This is probably not a magnetic chemically peculiar star.

HD 36540: This star is listed in the Renson & Manfroid (2009) catalogue as a B7 He-weak star. The largest set of magnetic measurements were published by Romanyuk et al. (2017b). The magnetic field was also detected by Bagnulo et al. (2015a). There is 1 ESPaDOnS observation, which yields a definite detection in the LSD Stokes V profile (see Fig. C1). By combining all available magnetic data together with the *Hipparcos* photometry, we get a period of 2.1725(4) d, consistent with the *Hipparcos* period determined by Dubath et al. (2011). The *TESS* light curve gives a period of 2.1723(1) d, formally consistent with the *Hipparcos* period, which is used to phase the data in Fig. C7.

HD 36629: This star was included in the Bychkov et al. (2005) catalogue due to an old measurement by Conti (1970). However, its magnetic field was not detected by Bagnulo et al. (2015a) or by Romanyuk et al. (2017b). There are 2 ESPaDOnS observations, both of which are non-detections with 4 G error bars (Fig. C1). The rotational period given by Bychkov et al. (2005), based on $\langle B_z \rangle$ measurements, is therefore certainly spurious and this star was dropped from the analysis.

HD 36668: Romanyuk et al. (2021a) determined a period of 2.1204 d using the *TESS* light curve, however this utterly fails to phase either the SAO or DAO $\langle B_z \rangle$ measurements, whether the datasets are treated individually or combined. Reanalysis of the *TESS* light curve yields 2.1192(2) d. Fig. C8 shows $\langle B_z \rangle$ and the *TESS* data phased with the nearest period **to the *TESS* period** providing a reasonably coherent variation **of both $\langle B_z \rangle$ and *TESS* data**, although there is considerable scatter. Additional magnetic observations, preferably at high resolution, are necessary in order to constrain both the magnetic and rotational properties.

HD 36916: The *Hipparcos* light curve yields a period of 1.5652(2) d (Romanyuk et al. 2017a). There are $\langle B_z \rangle$ measurements available from Borra et al. (1983), Bagnulo et al. (2015b), and Romanyuk et al. (2017a, 2018, 2020). The *TESS* period is 1.5652(1), identical to the *Hipparcos* period

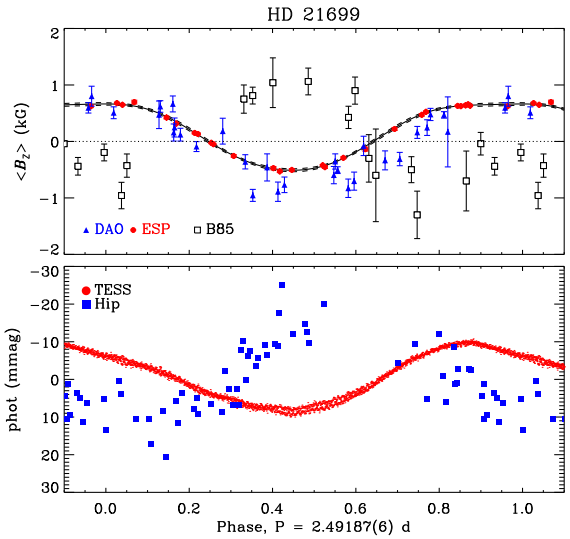

Figure C2. *Top*: $\langle B_z \rangle$ measurements for HD 21699, obtained from Brown et al. (1985), DAO, and ESPaDOnS data, folded with the rotation period. Solid/dashed curves show third-order harmonic fit and uncertainty. *Bottom*: *TESS* and *Hipparcos* light curves folded with the rotation period.

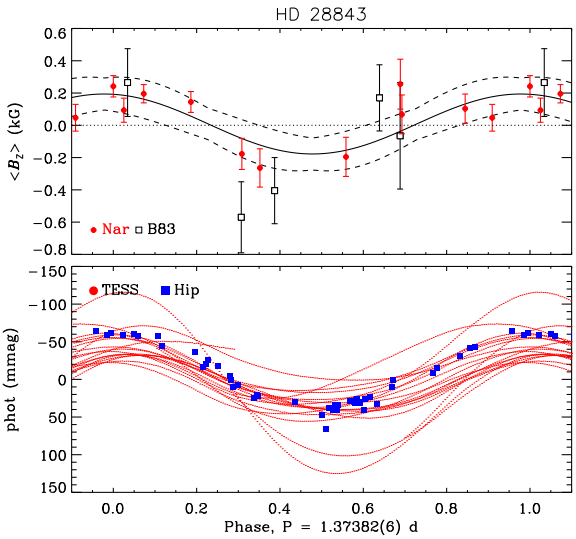

Figure C4. *Top*: $\langle B_z \rangle$ measurements for HD 28843, obtained from Borra et al. (1983) and Narval, folded with the rotation period. Solid/dashed curves show first-order harmonic fit and uncertainty. *Bottom*: *Hipparcos* and *TESS* light curves folded with the rotation period.

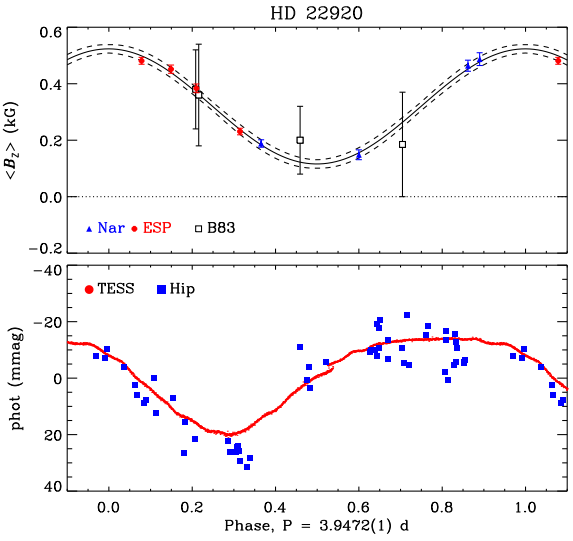

Figure C3. *Top*: $\langle B_z \rangle$ measurements for HD 22920, obtained from Borra et al. (1983), ESPaDOnS, and Narval, folded with the rotation period. Solid/dashed curves show first-order harmonic fit and uncertainty. *Bottom*: *Hipparcos* and *TESS* light curves folded with the rotation period.

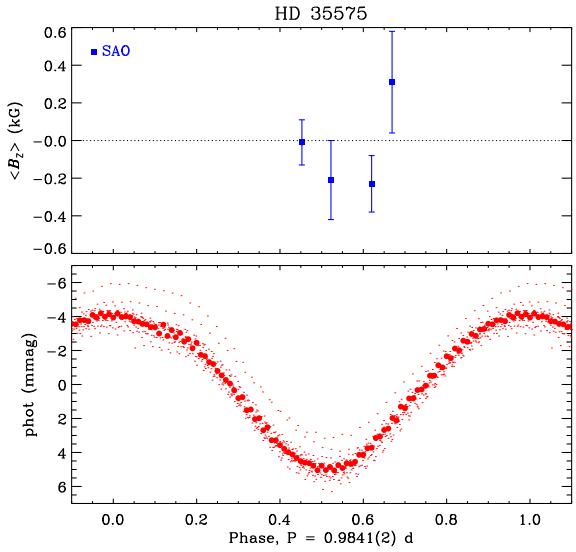

Figure C5. SAO $\langle B_z \rangle$ measurements (*top*) and *TESS* photometry (*bottom*) of HD 35575 phased with the rotation period.

but slightly more precise. The photometric periods do not quite provide a coherent phasing of the magnetic data; the closest period which does is 1.56548(8) d, which still provides a reasonable phasing of the photometry (Fig. C9).

HD 36960: This star is listed in the Renson & Manfroid (2009) catalogue as a B0 Si star. No magnetic field has been detected either in FORS observations (Bagnulo et al. 2015a) or with ESPaDOnS (10 G error bar, Fig. C1). Furthermore, a rotation period cannot be determined as there is no indication of regular variation in the TESS light curve. This star is probably not magnetic.

HD 37041: This star was included in the Bychkov et al. (2005) catalogue, however the rotation period was determined using old $\langle B_z \rangle$ measurements (Kemp & Wolstencroft 1973; Borra 1975), which have been superseded by modern low-resolution spectropolarimetry (Bagnulo et al. 2015a)

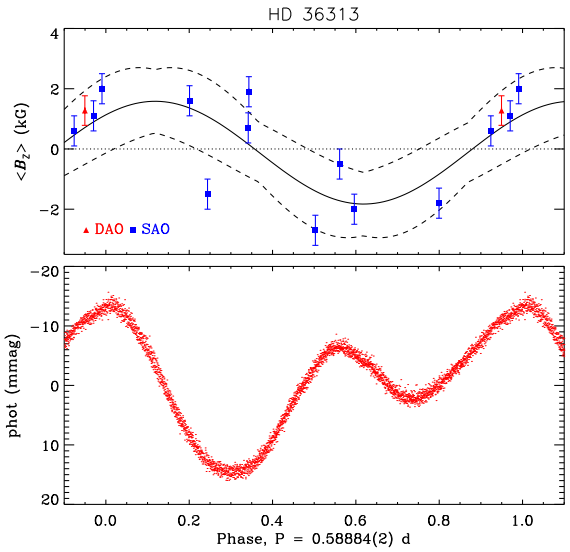

Figure C6. *Top*: SAO and DAO $\langle B_z \rangle$ measurements from Romanyuk et al. (2021a) phased with the rotation period. *Bottom*: *TESS* photometry phased with the rotation period.

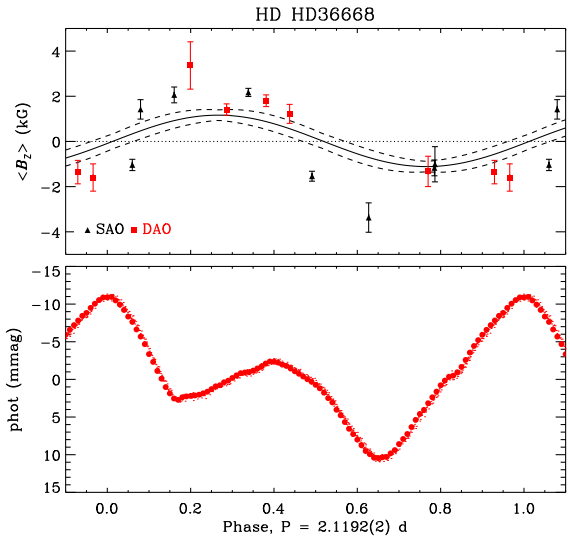

Figure C8. *Top* DAO and SAO $\langle B_z \rangle$ measurements phased with the rotation period. *Bottom*: *TESS* light curve phased with the rotation period. Larger points indicate phase-binned data.

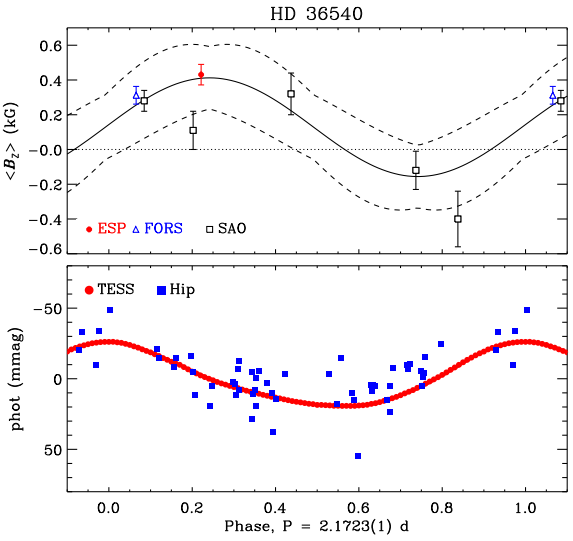

Figure C7. *Top*: $\langle B_z \rangle$ measurements for HD 36540, obtained from Romanyuk et al. (2017b), Bagnulo et al. (2015a), and ESPaDOnS, folded with the rotation period. Solid/dashed curves show first-order harmonic fit and uncertainty. *Bottom*: *Hipparcos* and *TESS* light curves folded with the rotation period. Larger points indicate phase-binned data.

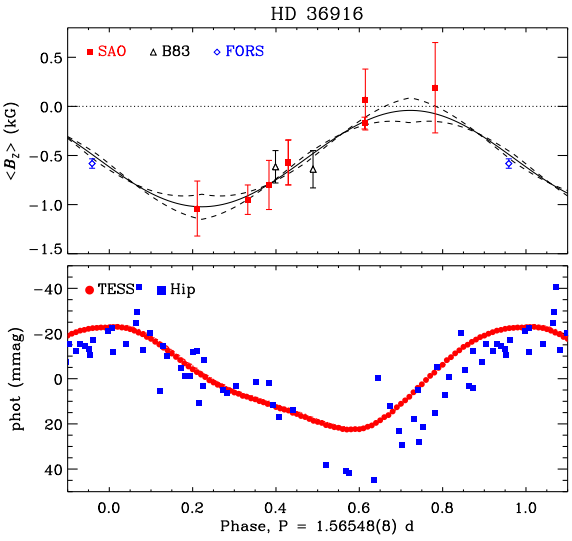

Figure C9. *Top*: $\langle B_z \rangle$ measurements phased with the rotation period. *Bottom*: *Hipparcos* and *TESS* photometry phased with the rotation period. Larger points indicate phase-binned data.

and by high-resolution MiMeS data (Grunhut et al. 2017), all non-detections. Petit et al. (2019) established an upper limit of 193 G on B_d. This star is therefore not magnetic, the period is clearly spurious, and it was dropped from the analysis.

HD 37129: This star is listed in the Renson & Manfroid (2009) catalogue as a B3 He-weak star. No magnetic field has been detected (Borra et al. 1983). There are numerous significant periods in the *TESS* light curve, which do not resemble rotation and are therefore likely pulsations.

HD 37140: This star is listed in the Renson & Manfroid (2009) catalogue as a B8 SiSr star. It is included in the Bychkov et al. (2005) catalogue, where the 2.7 d period from North (1984) was used to phase available $\langle B_z \rangle$ measurements. More recent magnetic data have been provided by Romanyuk et al. (2017b, 2020). There is one available ESPaDOnS observation, yielding a definite detection (-186 ± 22 G; Fig. C1). Romanyuk et al. (2021a) used the TESS

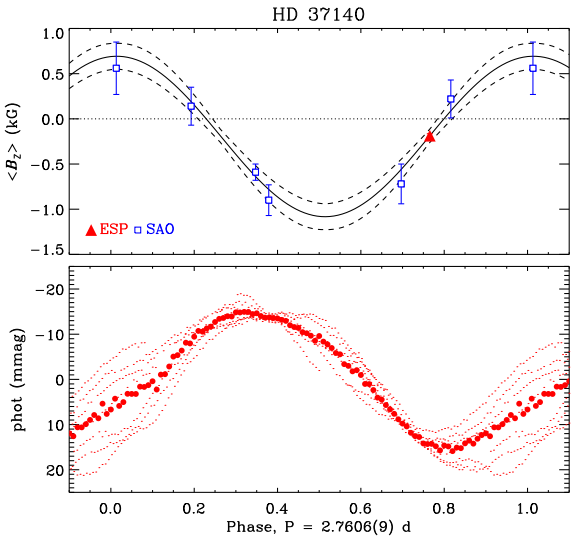

Figure C10. *Top*: SAO and ESPaDOnS $\langle B_z \rangle$ measurements for HD 37140. *Bottom*: TESS light curve folded with the rotation period. Larger points indicate phase-binned data.

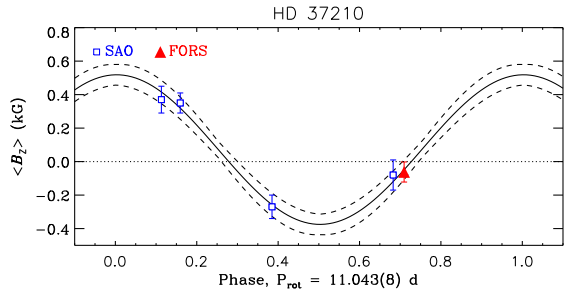

Figure C11. SAO and FORS $\langle B_z \rangle$ measurements for HD 37210.

light curve to refine the period to 2.70418(1) d. However, this does not coeherently phase the combined SAO and ESPaDOnS dataset. Our own analysis of the TESS data gives 2.702(2) d, which also fails to phase the magnetic data. The closest period to the TESS period resulting in a smooth variation is 2.7606(9) d (Fig. C10). The *TESS* data are severely affected by systematics (or other sources of variability beyond rotation) that may affect the accuracy of the photometric period; only one rotational cycle of *TESS* data are shown in Fig. C10.

HD 37150: This B3 III star is not listed in the Renson & Manfroid (2009) catalogue, and no magnetic field was detected by Borra (1981). The *TESS* light curve has two closely spaced peaks at around 0.7 and 0.8 d, which are too short to be associated with rotation in the absence of other compelling evidence that the star is magnetic.

HD 37210: The 11.0494(1) d photometric period (Catalano & Renson 1998) does not quite phase the available $\langle B_z \rangle$ measurements from FORS (Bagnulo et al. 2015a) and the SAO (Romanyuk et al. 2021b). The *TESS* light curve is heavily affected by systematics and cannot

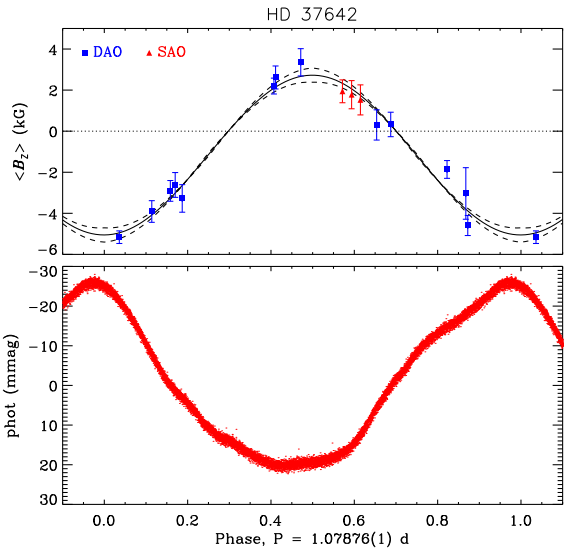

Figure C12. *Top*: DAO and SAO $\langle B_z \rangle$ measurements for HD 37642, phased with the TESS rotation period. *Bottom*: TESS photometry phased with the rotation period.

be used to determine the period. The closest period that coherently phases the data is 11.043(8) d (Fig. C11).

HD 37321: This star is listed in the Renson & Manfroid (2009) catalogue as a B5 He-weak star. No magnetic measurements are available. The *TESS* light curve, acquired in sector 6, is dominated by high-frequencies (more than 2 c/d) that must be pulsation; there is no obvious rotational modulation in the time series.

HD 37642: This star is listed in the Renson & Manfroid (2009) catalogue as a B9 He-weak Si star. The period determined from the *TESS* data is 1.07876(1) d. $\langle B_z \rangle$ measurements from DAO and SAO are phased with this period in Fig. C12.

HD 37808: This star is listed in the Renson & Manfroid (2009) catalogue as a B9 Si star. Clear rotational modulation is present in the *Hipparcos* light curve at 1.0989(1) d (Dubath et al. 2011); reanalysis of the *Hipparcos* data confirms this period. Bernhard et al. (2020) found a period of 1.09852(2) by combining KELT, ASAS-3, and MASCARA data. The *TESS* light curve gives a period of 1.09851(8) d, consistent with previous results. Combining *TESS* and *Hipparcos* yields a coherent phasing with a period of 1.098535(1) d, which is used to phase the data in Fig. C13. Five magnetic measurements were published by Romanyuk et al. (2021b). This star is detected in radio, and is an obvious candidate for spectropolarimetric follow-up given the sparse magnetic coverage.

HD 45105: This star is listed in the Renson & Manfroid (2009) catalogue as a B9 Si star. There are no magnetic data. There is no indication in the *TESS* light curve of rotational modulation. There is one peak in the periodogram at about 2.6 d, however it is exceedingly weak (0.015 mmag) and probably not associated with rotation.

HD 49606: Bychkov et al. (2005) found a 1.1 d period using $\langle B_z \rangle$ measurements collected from Bohlender et al. (1993a) and Bychkov et al. (1997). It is listed in the

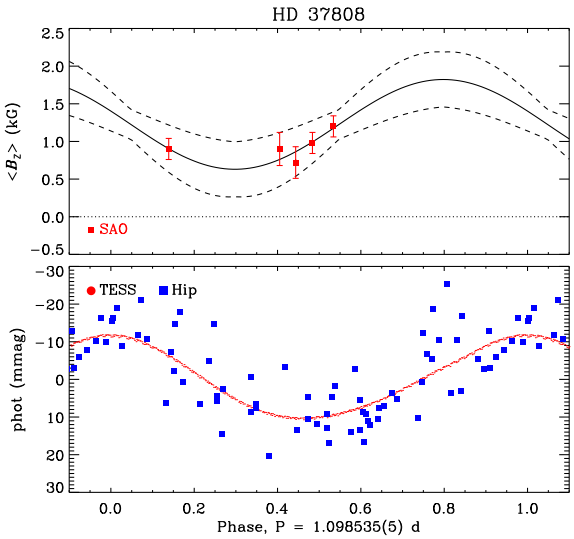

Figure C13. *Top*: DAO and SAO $\langle B_z \rangle$ measurements for HD 37808, phased with the TESS rotation period. *Bottom*: *Hipparcos* and *TESS* photometry phased with the rotation period.

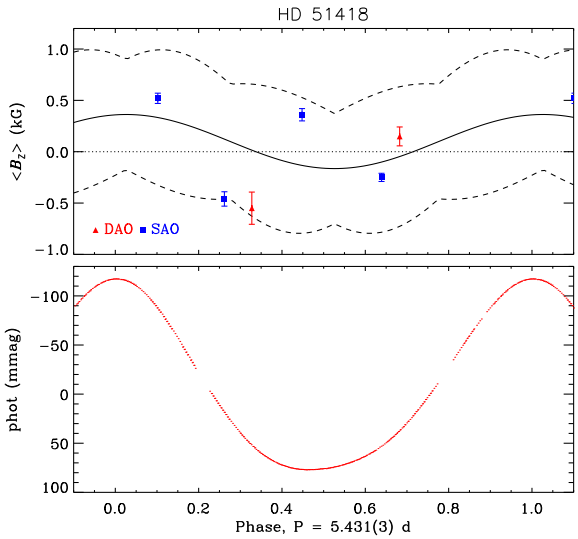

Figure C14. *Top*: DAO and SAO $\langle B_z \rangle$ measurements for HD 51418, phased with the TESS rotation period. *Bottom*: TESS photometry phased with the rotation period.

Renson & Manfroid (2009) catalogue as a B8 HgMn star, a class generally known to be non-magnetic (Makaganiuk et al. 2011). There are two ESPaDOnS observations, both non-detections with 7 G error bars (Fig. C1). The period determined from $\langle B_z \rangle$ measurements is therefore certainly spurious. The TESS light curve give a period of 8.546(1) d (Kochukhov et al. 2021).

HD 50204: This star is listed in the Renson & Manfroid (2009) catalogue as a B9 Si star. There are no magnetic data. There is no suggestion in the *TESS* light curve of rotational modulation. While there is a single peak in the periodogram at about 2.3 d, it is very weak (0.04 mmag) and therefore unlikely to be associated with rotation.

HD 51418: Bychkov et al. (2020) found a rotation period of 2.2908 d from the Romanyuk et al. (2017b) SAO magnetic measurements, in disagreement with the 5.4379 d photometric period from Renson & Catalano (2001). The *TESS* light curve shows clear rotational modulation with a period of 5.431(3) d (Fig. C14). Combining the SAO $\langle B_z \rangle$ measurements with DAO $\langle B_z \rangle$ measurements yields a period of 2.3357(4) d, with no power in the periodogram at higher periods. As can be seen in Fig. C14, the magnetic and photometric periods are completely incompatible assuming a single-wave variation in $\langle B_z \rangle$. We adopt the photometric period, and rather than sinusoidal fitting parameters for $\langle B_z \rangle$ use the mean and standard deviation of $\langle B_z \rangle$ to approximate B_0 and B_1.

HD 57219: This star is listed in the Renson & Manfroid (2009) catalogue as a B3 He-variable star. There are no magnetic data. There is possible rotational modulation in the *TESS* light curve with a period of about 1.4 d, however the 0.4 mmag amplitude is much lower than is usually associated with chemical spots (Sikora et al. 2019c), there are several other closely spaced peaks, and the peaks are fairly broad, all of which suggest that this is pulsation rather than rotation.

HD 60344: This star is listed in the Renson & Manfroid (2009) catalogue as a B3 He star. A magnetic field was detected by Järvinen et al. (2018). *TESS* observations were acquired in sectors 7 and 34. As the star is in a crowded region, contamination by other sources is highly likely. The sector 34 light curve is heavily affected by systematics. The sector 7 light curve is affected by a long-term trend, likely systematic; while there is real variability on top of this, with an apparent period of about 9 days, it is irregular in amplitude and there is no reason to think it is related to the star's rotation.

HD 78556A: This star is listed in the Renson & Manfroid (2009) catalogue as a B9 Si star. There are no magnetic data. There is no indication in the *TESS* light curve of rotational modulation.

HD 89822: Bychkov et al. (2005) phased the available $\langle B_z \rangle$ measurements (Babcock 1958; Conti 1970; Borra & Landstreet 1980; Bohlender et al. 1993a; Plachinda et al. 1993) with a 7.6 d period determined photometrically by Catalano & Leone (1991). The star is listed in the Renson & Manfroid (2009) catalogue as an A0 HgSiSr star. The 7.6 d period cannot be confirmed via *Hipparcos* photometry. Furthermore, all 5 of the available ESPaDOnS observations are non-detections, with 2 G error bars (Fig. C1). The rotation period is therefore spurious, and the star is not magnetic. The system is an SB2, with a HgMn primary and an Am secondary in an 11.579 d orbit (Adelman 1994; Pourbaix et al. 2004); Kochukhov et al. (2021) found an 11.581 d periodicity in the *TESS* light curve, which they attributed to heartbeat variability.

HD 89897: This star is listed as a B9 SiCr star by Renson & Manfroid (2009). No magnetic data are available. The *TESS* light curve yields a clear 1.11037(5) d periodicity (see Fig. C15). Despite the rapid rotation, the star is radio-dim, suggesting that its magnetic field must be weak if present.

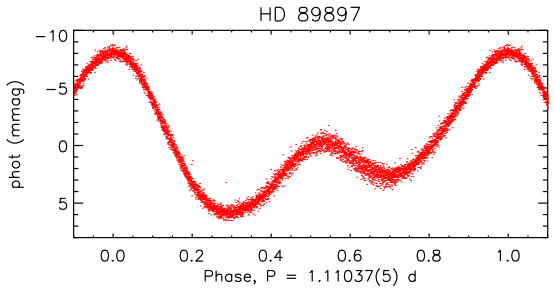

Figure C15. *TESS* light curve of HD 89897 folded with the rotation period.

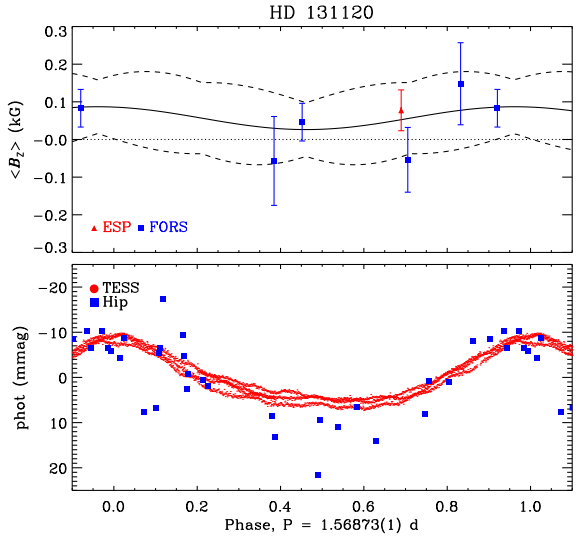

Figure C16. *Top*: $\langle B_z \rangle$ measurements phased with the rotation period determined from photometric and magnetic data. *Bottom*: TESS photometry phased with the rotation period

HD 120709: This star is listed in the Renson & Manfroid (2009) catalogue as a B5 He-weak star. The *TESS* light curve is dominated by a 0.27 d period and its 1st harmomic, almost certainly pulsation as this is much too fast to be rotation. Furthermore, all magnetic measurements are non-detections (Borra et al. 1983; Bagnulo et al. 2015a).

HD 131120: This star is listed in the Renson & Manfroid (2009) catalogue as a B6 He-weak star. *Hipparcos* photometry yields a 1.5690(3) d period (Dubath et al. 2011). The *TESS* light curve gives a period of 1.5686(1) d, formally compatible with the *Hipparcos* period. The *TESS* data shows some evidence of variability between cycles, which may indicate that the period is due to pulsation rather than rotation, or that it is also affected by pulsation (Fig. C16). Combining the *TESS* and *Hipparcos* data yields a coherent phasing with a period of 1.56873(1) d. No magnetic field was detected in 5 FORS2 observations, with error bars of 50-100 G (Bagnulo et al. 2015a). There is 1 ESPaDOnS observation, also a non-detection with a 50 G error bar (Fig. C1). Asymmetry in the LSD profile is indicative of binarity. Under the assumption that the ∼1.5 d period is in fact rotational, the available $\langle B_z \rangle$ measurements are phased with the

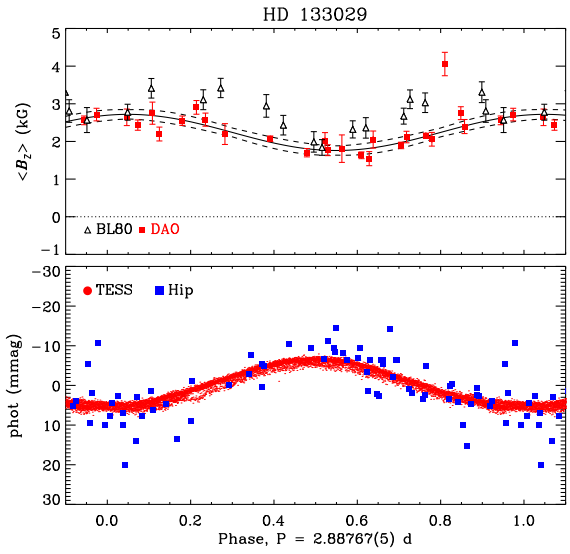

Figure C17. *Top*: $\langle B_z \rangle$ measurements phased with the rotation period determined from photometric and magnetic data. *Bottom*: TESS photometry phased with the rotation period

TESS period in Fig. C16. Since the magnetic field was not detected, B_0 and B_1 were approximated using the mean and standard deviation of $\langle B_z \rangle$. As can be seen, while no magntic field is detected there is a tendency for $\langle B_z \rangle$ to be systematically positive, which may be indicative that the star is indeed magnetic, even though no individual measurement is formally consistent with a detection.

HD 133029: The 2.8804(3) d *TESS* period provides a poor phasing of the $\langle B_z \rangle$ measurements. The period from Adelman (2008) is similar (2.88756 d), but more precise, and while it does phase the individual $\langle B_z \rangle$ datasets this period does not phase the combined DAO and Borra & Landstreet (1980) magnetic datasets. The nearest period which approximately phases $\langle B_z \rangle$ is 2.88767(6) d, which also gives a coherent phasing of the TESS and *Hipparcos* photometry, although this does not result in a perfect match in $\langle B_z \rangle$(see Fig. C17). It is possible the period may not be constant. There are systematic differences between the two $\langle B_z \rangle$ datasets; as the DAO dataset is larger and exhibits less scatter, it was used to fit $\langle B_z \rangle$.

HD 135679: The period derived from the *TESS* light curve is 5.314(1) d, but this doesn't quite phase the $\langle B_z \rangle$ measurements. Combining the DAO and SAO data, the nearest period that approximately phases the magnetic data is 5.321(1) d, which also provides acceptable phasing of the *TESS* data (Fig. C18). While *Hipparcos* data are available, the amplitude of the photometric variation is smaller than the mean error bar of those measurements, which therefore cannot be used to improve the period.

HD 137193: This star is listed in the Renson & Manfroid (2009) catalogue as a B9 Si star. The *Hipparcos* light curve gives a period of 16.3 d. However, the *TESS* light curve gives a clear period of 4.867(3) d, which also phases the *Hipparcos* data coherently. Since the amplitude of the modulation in the *TESS* light curve is comparable to the uncertainty in the *Hipparcos* data, it is probable that the *Hipparcos* result

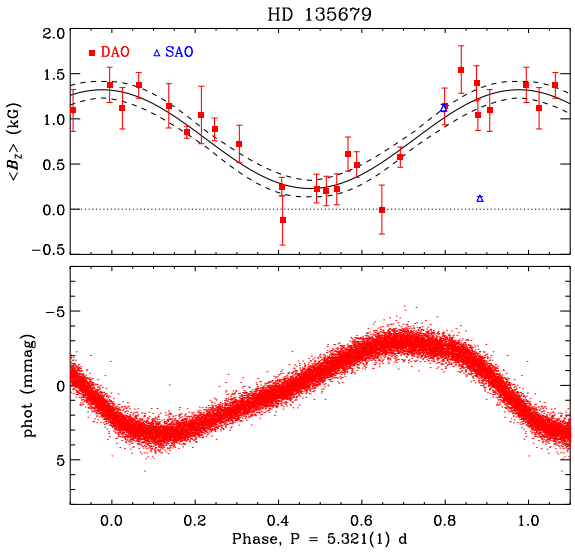

Figure C18. *Top*: $\langle B_z \rangle$ measurements phased with the rotation period determined from photometric and magnetic data. *Bottom*: *TESS* photometry phased with the rotation period.

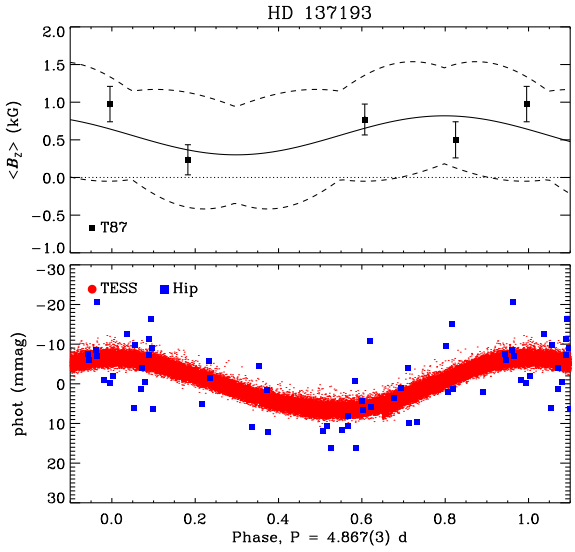

Figure C19. *Top*: $\langle B_z \rangle$ measurements for HD 137193, obtained from Thompson et al. (1987), folded with the rotation period. Solid curve shows first-order harmonic fit; fit uncertainty is larger than the y-axis. *Bottom*: *Hipparcos* and *TESS* light curves folded with the rotation period.

is spurious. Four magnetic measurements were published by (Thompson et al. 1987), shown phased with the TESS period in Fig. C19.

HD142250: This star is listed in the Renson & Manfroid (2009) catalogue as a B6 He-weak star. No magnetic field was detected by Thompson et al. (1987). The *TESS* light curve is clearly dominated by pulsation, with several peaks around 0.4 d with similar amplitudes (0.3–0.5 mmag). There is one low-amplitude (0.14 mmag) peak at around 3.1 d

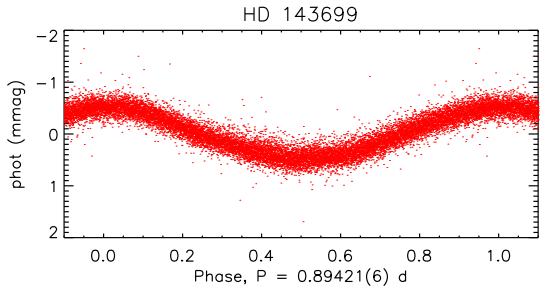

Figure C20. TESS light curve for HD 143699, folded with the rotation period. The data have been pre-whitened with the probable pulsation frequency at 1.12 c/d.

which may be associated with rotation, however this could easily be *g*-mode pulsation.

HD 142884: This star is listed in the Renson & Manfroid (2009) catalogue as a B9 Si star. Netopil et al. (2017) give a period of 0.8 d, as confirmed from *K2* data by Rebull et al. (2018), and by Bernhard et al. (2020) from ASAS-3, KELT, and MASCARA photometry. No magnetic field was detected by Borra et al. (1983). There is 1 Narval observation, a non-detection with a 150 G error bar (Fig. C1). The broad spectral lines ($v \sin i = 130$ km s^{-1}) are consistent with an 0.8 d rotation period.

HD 143699: This star is listed in the Renson & Manfroid (2009) catalogue as a B6 He-weak star. The strongest frequency in the TESS light curve corresponds to a period of 0.89421(6) d, which is used to phase the light curve in Fig. C20; however, there is also an unrelated peak in the periodogram corresponding to a possible rotational period of 1.3188(5) d, with the first harmonic of this frequency also present. No magnetic field was detected by Borra et al. (1983). There is one ESPaDOnS observation, a non-detection with a 76 G error bar. The LSD Stokes *I* profile is highly asymmetric, possibly indicating binarity (Fig. C1). The broad lines ($v \sin i \sim 115$ km s^{-1}) are consistent with a short rotation period, however, the extremely low amplitude of the variation (below 1 mmag), and the presence of multiple unrelated frequencies, suggests star may also display *g*-mode pulsations, which may be related to one or all of the frequencies. However, it is a radio-bright star, indicating that it is probably magnetic.

HD 144844: This star is listed in the Renson & Manfroid (2009) catalogue as a B9 MnPGa star, a higher-mass analogue to HgMn stars in which magnetic fields have not been detected (Shultz et al. 2018a). Netopil et al. (2017) give a photometric period of 2.69 d. No magnetic field was detected by Borra et al. (1983). There is one ESPaDOnS observation, a ND with a 9 G error bar. The LSD profiles indicate the star is an SB2 (Fig. C1).

HD 145482: This star is not listed in the Renson & Manfroid (2009) catalogue. The 2 published magnetic measurements are non-detections (Thompson et al. 1987). However, there is clear modulation in the TESS light curve at 5.804(1) d, together with numerous low-amplitude, high-frequency (above about 3 c/d) signals, as can be seen superimposed on the probable rotational modulation in Fig. C21.

HD 146001: This star is listed in the Renson & Manfroid

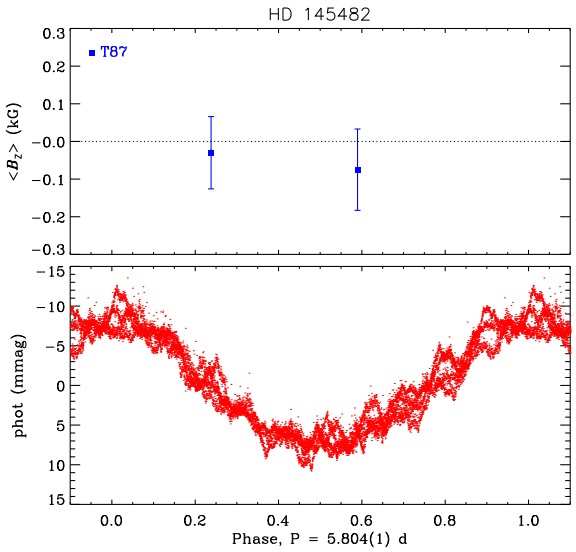

Figure C21. *Top* $\langle B_z \rangle$ measurements phased with the rotation period. *Bottom*: TESS light curve for HD 145482, folded with the rotation period. The light-curve also exhibits high-frequency pulsations.

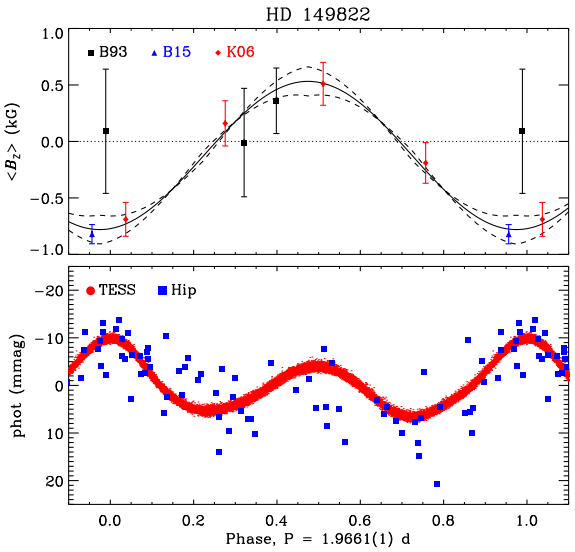

Figure C22. *Top*: $\langle B_z \rangle$ measurements for HD 149822, obtained from Bohlender et al. (1993a), Kudryavtsev et al. (2006), and Bagnulo et al. (2015a), folded with the rotation period. Solid curve shows first-order harmonic fit. *Bottom*: *Hipparcos* and *TESS* light curves folded with the rotation period.

(2009) catalogue as a B8 He-weak star. Wraight et al. (2012) give two photometric periods, 3.6 d and 0.58612 d. There are 2 ESPaDOnS observations. The LSD profiles are both non-detections with 65 G error bars (Fig. C1). The broad lines ($v \sin i \sim 90$ km s^{-1}) are inconsistent with the longer Wraight et al. (2012) period, but are consistent with the short period. The LSD profiles exhibit line profile variability, which could be consistent with spots, binarity, or pulsations. There is no indication of a 0.58 d period in the *Hipparcos* light curve, and the lowest FAP in the periodogram is 0.57. However, despite the lack of clear rotational modulation in the *Hipparcos* data and the lack of a magnetic detection, this star is radio-bright.

HD 147084: This star is not listed in the Renson & Manfroid (2009) catalogue. The published magnetic data are non-detections (Thompson et al. 1987; Bagnulo et al. 2015a). There are 2 ESPaDOnS measurements, both NDs with 2 G error bars (Fig. C1). The *Hipparcos* period is 1.8611(2) d, although as the FAP is 0.04 this signal is probably spurious. This is probably not a magnetic star.

HD 149822: This star is listed in the Renson & Manfroid (2009) catalogue as a B9 SiCr star. There are several low-resolution magnetic measurements (Bohlender et al. 1993a; Kudryavtsev et al. 2006; Bagnulo et al. 2015a). The *TESS* light curve gives a period of 1.9663(3) d; a period of 1.9661(1) d coherently phases the *TESS* and *Hipparcos* data, which provides a reasonable phasing of the sparse magnetic data (Fig. C22).

HD 157779: This star is listed in the Renson & Manfroid (2009) catalogue as a B9 Si star. There are no magnetic data. The *TESS* light curve shows probable rotational modulation on a 3.2566(8) d period (see Fig. C23); the multiple harmonics of the rotational period are difficult to reconcile with other mechanisms such as pulsation.

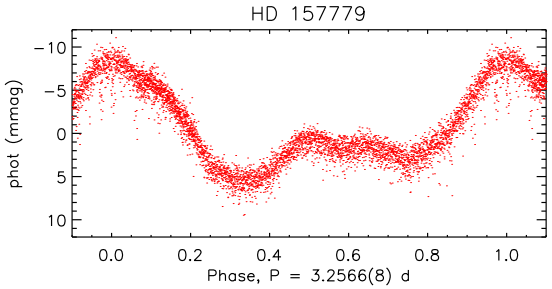

Figure C23. *TESS* light curve of HD 157779 folded with the rotational period.

HD 162374: This star is listed in the Renson & Manfroid (2009) catalogue as a B7 He-weak star. Catalano & Renson (1998) give a photometric period of 1.66 d. Its magnetic field was not detected by Borra et al. (1983). There is one available ESPaDOnS measurement, a ND with a 27 G error bar. *Hipparcos* photometry does not confirm the 1.66 d period; the maximum amplitude is at 1.15 d, with a FAP of 0.09. Given the non-detection of the magnetic field and the low significance of the photometric period, the period is probably not a rotational period, and this is probably not a magnetic star. Asymmetry in the LSD Stokes I profile is consistent with binarity (Fig. C1).

HD 164429: This star is listed in the Renson & Manfroid (2009) catalogue as a B9 SiCrSr star. There is only one published magnetic measurement, a non-detection (Bohlender et al. 1993a), however the magnetic field is clearly detected in the much larger DAO dataset. The *Hipparcos* light-curve gives a period of 1.0817(1) d, although as the FAP is 0.43 this period could not be confirmed. However, the photmetric variation is clearly seen in the *TESS*

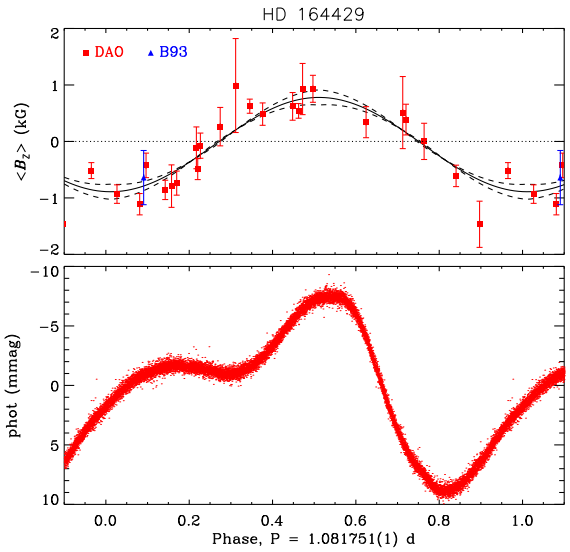

Figure C24. *Top*: $\langle B_z \rangle$ measurements for HD 164429, phased with the period determined from TESS data. *Bottom*: TESS light curve folded with the rotation period.

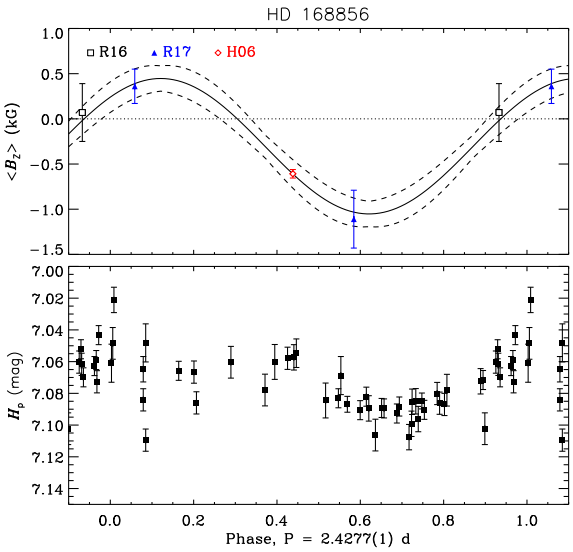

Figure C25. *Top*: $\langle B_z \rangle$ measurements for HD 168856, obtained from Romanyuk et al. (2016b), Romanyuk et al. (2017b), and Hubrig et al. (2006), folded with the rotation period. *Bottom*: *Hipparcos* light curve phased with the rotation period.

light curve, which yields a period of 1.08175(1) d, almost identical to the period recovered from the *Hipparcos* data. The DAO $\langle B_z \rangle$ measurements are shown phased with this period in (Fig. C24).

HD 166182: This is a chemically normal B2 IV star. No magnetic field was detected by Landstreet (1982). The *TESS* light curve has two low-amplitude (0.06–0.1 mmag) periodicities at around 4 d, which are probably associated with pulsation.

HD 168785: This star is listed in the Renson & Manfroid (2009) catalogue as a B3 He star. A magnetic field was detected by Järvinen et al. (2018). It is in a crowded field, and the *TESS* light curve is probably contaminated by other stars; there is furthermore an artifact at the beginning of the time series, for which reason the first day was discarded. The light curve is dominated by a long-term trend, likely systematic. There are significant periods at 11.47 d, 4.98 d, and 6.43 d, which do not appear to be harmonically related and therefore likely do not reflect the star's rotation.

HD 168856: This star is listed in the Renson & Manfroid (2009) catalogue as a B9 Si star. A magnetic detection was reported by Romanyuk et al. (2017b). The photometric period of 2.4277(1) d was reported by Bernhard et al. (2020), based on ASAS-3, KELT, and MASCARA data. Available $\langle B_z \rangle$ and the *Hipparcos* light curve are shown folded with this period in Fig. C25.

HD 170973: This star is listed in the Renson & Manfroid (2009) catalogue as an A0 SiCrSr star. Bychkov et al. (2005) gave a period of 18.52 d based on sparse $\langle B_z \rangle$ measurements (Mathys 1991b; Bohlender et al. 1993a). *Hipparcos* photometry gives a period of 18.09(3) d, with a FAP of 0.02. There are 3 available ESPaDOnS measurements, all DDs (Fig. C1). The *Hipparcos* period does not phase the available $\langle B_z \rangle$ measurements coherently; by combining them, a period of 18.064(5) d is obtained (see Fig. C26).

HD 171247: This star is listed in the Renson & Manfroid

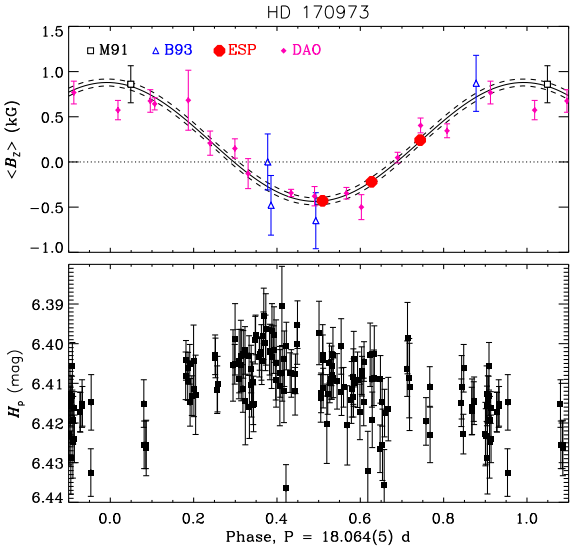

Figure C26. *Top*: $\langle B_z \rangle$ measurements for HD 170973, obtained from Mathys (1991b), Bohlender et al. (1993a), and ESPaDOnS, folded with the rotation period. Solid curve shows first-order harmonic fit. *Bottom*: *Hipparcos* light curve folded with the rotation period.

(2009) catalogue as a B8 Si star. The star is notable for being one of the only radio-bright stars apparently in the second half of the main sequence, which is difficult to explain given that magnetospheric braking should have long ago spun the star down to the point where its radio emission should have disappeared, whereas to the contrary its radio luminosity is relatively high. There is clear rotational modulation in the *Hipparcos* light curve at 3.9124(8) d, with a FAP of 10^{-15}.

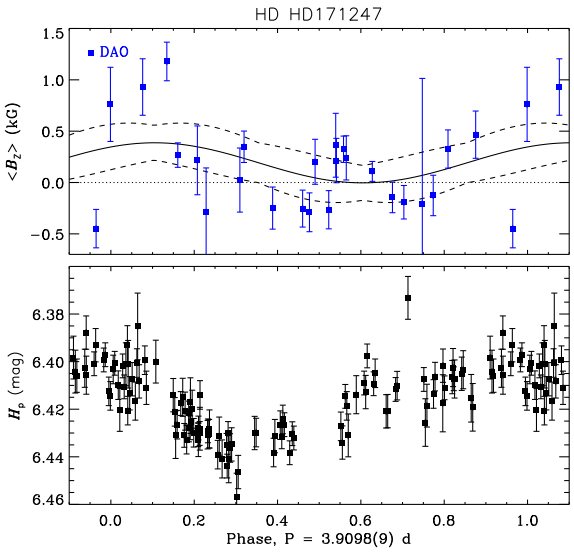

Figure C27. DAO $\langle B_z \rangle$ measurements (*top*) and *Hipparcos* light curve (*bottom*) of HD 171247 folded with the photometric period.

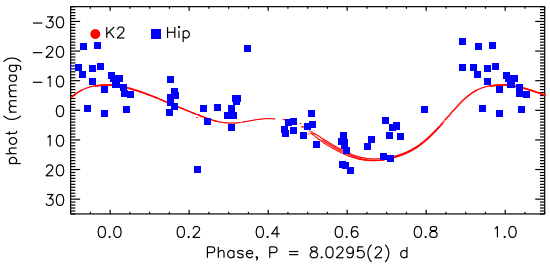

Figure C28. *Hipparcos* and *K2* light curves of HD 175132 folded with the rotation period.

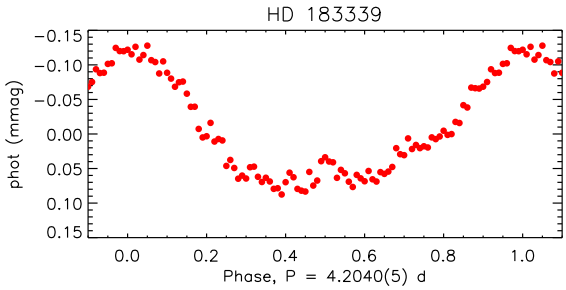

Figure C29. Phase-binned *TESS* light curve of HD 183339, folded with the strongest period.

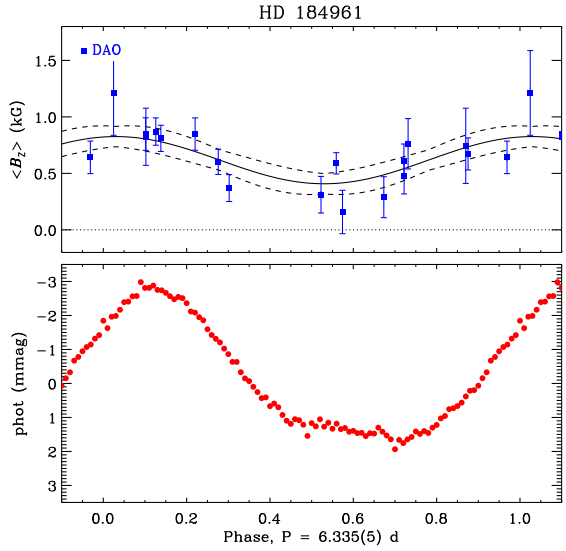

Figure C30. DAO $\langle B_z \rangle$ measurements (*top*) and phase-binned *TESS* light curve (*bottom*) phased with the period determined from the magnetic data.

This period does not provide a coherent phasing of $\langle B_z \rangle$, period analysis of which yields 1.14482(6) d, with a FAP of 0.009; however, this period fails to phase the photometry. The closest period that can approximately phase both datasets is 3.9098(9) d (see Fig. C27), a 3σ difference from the best photometric period.

HD 175132: This star is listed in the Renson & Manfroid (2009) catalogue as a B9 Si star. The magnetic field was reported by Bychkov et al. (2003), although only the root-mean-square $\langle B_z \rangle$ was published, not the individual measurements. *Hipparcos* photometry gives a period of 8.031(6) d, with a FAP of 10^{-6}. Hümmerich et al. (2018) reported that a period could not be determined from the K2 light curve, however, examination of these data yields a clear periodicity of 8.033(5) d, approximately consistent with the period inferred from *Hipparcos*. Combining the two gives a period of 8.0295(2) d, which is used in Fig. C28.

HD 183339: This star is listed as a B8 He-weak star by Renson & Manfroid (2009). Bychkov et al. (2003) reported $B_{\rm rms} = 1300 \pm 465$ G based upon 8 measurements, although these were not individually published, and Bychkov et al. (2020) phased the available magnetic data with a 2.42 d period. The star was observed in 7 *TESS* sectors. There is no indication of the 2.42 d periodicity in the light curve. The strongest peak in the periodogram is at 4.2040(5) d. The phase-binned light curve is shown folded with this period in Fig. C29. The amplitude of the variation is extremely low (less than 0.1 mmag), and it is likely that this reflects $g-$mode pulsation rather than rotational modulation. Evaluating the $\langle B_z \rangle$ curve published by Bychkov et al. (2020), the uncertainties in the $\langle B_z \rangle$ measurements used to obtain the magnetic model are very large (about 500 G). This star's magnetic field should be re-evaluated using modern instruments.

HD 184961: This star is listed in the Renson & Manfroid (2009) catalogue as a B9 CrSiEu star. The *Hipparcos* light curve yields a 6.016(3) d period, although the FAP of 0.95 indicates this is probably not significant. The *TESS* light curve yields a period of 6.35(1) d, although this is uncertain due to the presence of multiple flares which may indicate contamination by a late-type star. DAO $\langle B_z \rangle$ measurements yield a period of 6.692(6) d, which is similar to albeit formally different from the *TESS* period. The nearest period to the *TESS* period that provides a good phasing of $\langle B_z \rangle$ is

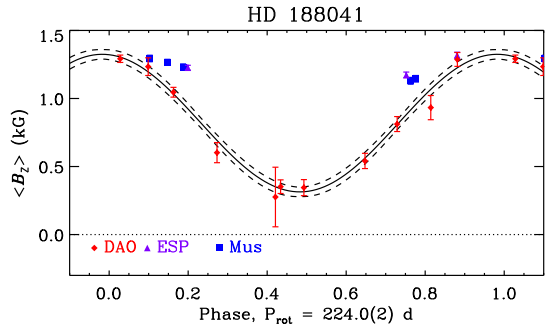

Figure C31. $\langle B_z \rangle$ measurements of HD 188041 phased with the period determined from the same measurements.

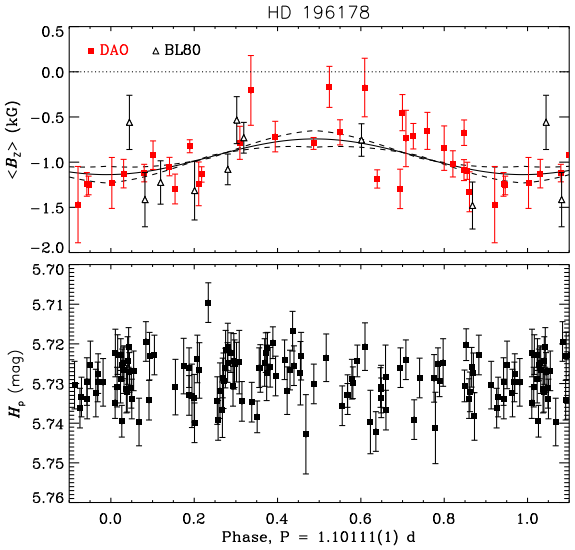

Figure C32. $\langle B_z \rangle$ measurements of HD 196178 (*top*) and *Hipparcos* light curve (*bottom*) phased with the period determined from the magnetic data.

6.335(5) d, which is consistent within uncertainty with the *TESS* period. The DAO $\langle B_z \rangle$ measurements and *TESS* photometry are shown phased with this period in Fig. C30.

HD 188041: ESPaDOnS and MuSiCoS $\langle B_z \rangle$ measurements were published by Sikora et al. (2019b), but did not cover the entire rotation cycle. Fig. C31 shows these measurements together with new DAO measurements, phased with the rotation period adopted by Sikora et al. (2019b), with which we have re-determined the star's ORM parameters.

HD 196178: This star is listed in the Renson & Manfroid (2009) catalogue as a B8 Si star. A photometric period of 1.92 d was given by Watson et al. (2006), however this cannot be confirmed with the *Hipparcos* photometry, and does not phase the magnetic dataset. No secure period can be obtained from the Hippacos light curve. From the combined $\langle B_z \rangle$ measurements, obtained at the DAO and published by Borra & Landstreet (1980), we find a period of 1.10111(1) d with a FAP of 0.007 (Fig. C32).

HD 207840: This star is listed in the Renson & Manfroid (2009) catalogue as a B8 Si star. It was claimed to be magnetic by Gollnow (1971), however the 2 available ESPaDOnS observations are non-detections with 4 G error bars (Fig. C1). No rotational period is known. This is probably not a magnetic star.

HD 209339: This star is listed in the Renson & Manfroid (2009) catalogue as a B0 He star. Bychkov et al. (2003) reported $B_{\rm rms} = 493 \pm 545$ G based on 3 measurements, i.e. it is a magnetic non-detection. The star was observed by *TESS* in sectors 16, 17, and 24. The light curve exhibits numerous significant periods, but these are stochastic and likely related to pulsation rather than rotation.

HD 224128: This star is listed as a B3 He star by Renson & Manfroid (2009). No magnetic data are available. The *TESS* light curve yields several low-amplitude, closely spaced peaks near 0.5 c/d, which are likely due to g-mode pulsations rather than rotation.

HD 260858: This star is listed in the Renson & Manfroid (2009) catalogue as a B6 He star. A magnetic field was detected by Romanyuk et al. (2018). The star was observed by *TESS* in sector 6. The light curve is strongly contaminated by brighter nearby sources. It is dominated by a monotonic long-term trend, with two significant periods at 13.59 d and 5.96 d, neither of which resemble rotation.

HD 264111: This star is listed in the Renson & Manfroid (2009) catalogue as a B2 He star. No magnetic field was detected by Romanyuk et al. (2018). The star was observed by *TESS* in sector 6. There are several significant periods, none of which have any obvious harmonic relationship, suggesting that they are related to pulsation rather than rotation.

APPENDIX D: MEASURED RADIO FLUX DENSITIES

Table D1. Measured radio flux density (in mJy) at various wavelengths. Subscripts indicate the wavelength in cm. The superscripts beside each star indicate the works from which the fluxes were obtained according to the following key: *a*, Drake et al. (1987); *b*, Linsky et al. (1992); *c*, Leone et al. (1994); *d*, Leone et al. (1996); *e*, Leone et al. (2004); *f*, Drake et al. (2006); *g*, Chandra et al. (2015); *h*, Kounkel et al. (2017); *i*, Kurapati et al. (2017); *j*, Leto et al. (2017); *k*, Leto et al. (2018); *l*, Das et al. (2019b); *m*, Leto et al. (2020a); *n*, Leto et al. (2020b); *o*, Pritchard et al. (2021); *p*, Leto et al. (2021); *q*, Das & Chandra (2021); *r*, Das et al. (submitted); *s*, Drake (priv. comm.); *t*, This Work.

Star	$F_{0.3}$	F_1	F_2	F_3	F_6	F_{13}	F_{20}	F_{50}
HD108^{i}	–	< 0.04	–	< 0.02	–	–	–	–
HD886^{s}	–	–	–	< 0.21	–	–	–	–
HD3360^{i}	–	< 0.04	–	< 0.02	–	< 0.03	–	–
HD5737^{a}	–	–	–	–	< 0.27	–	–	–
HD11502^{b}	–	–	–	–	< 0.18	–	–	–
HD11503^{bt}	–	–	–	–	< 0.18	–	–	0.25 ± 0.03
HD12447^{f}	–	–	–	0.37 ± 0.09	–	–	–	1.00 ± 0.10
HD12767^{s}	–	–	–	< 0.47	–	–	–	–
HD19832^{f}	–	–	–	0.45 ± 0.12	–	–	–	–
HD20629^{s}	–	–	–	< 0.28	–	–	–	–
HD21699^{a}	–	–	–	–	< 0.42	–	–	–
HD22470^{a}	–	–	–	–	< 0.36	–	–	–
HD22920^{s}	–	–	–	< 0.27	–	–	–	–
HD23408^{a}	–	–	–	–	< 0.19	–	–	–
HD25267^{s}	–	–	–	< 0.26	–	–	–	–
HD27309^{f}	–	–	0.38 ± 0.02	0.33 ± 0.02	–	–	–	–
HD28843^{a}	–	–	–	–	< 0.25	–	–	–
HD32633^{b}	–	–	–	–	< 0.18	–	–	–
HD34452^{ab}	–	–	–	–	0.48 ± 0.10	–	–	–
HD35298^{bef}	1.61 ± 0.43	–	–	0.29 ± 0.07	0.28 ± 0.28	–	–	–
HD35456^{s}	–	–	–	< 0.20	–	–	–	–
HD35502^{ft}	–	–	–	2.97 ± 0.10	–	–	–	0.64 ± 0.16
HD35575^{c}	–	–	–	–	< 0.02	–	–	–
HD36313^{f}	–	–	–	0.49 ± 0.06	–	–	–	–
HD36429^{s}	–	–	–	< 0.20	–	–	–	–
HD36485^{abeg}	< 0.79	–	< 0.70	–	0.95 ± 0.10	–	1.20 ± 0.10	0.59 ± 0.32
HD36526^{bt}	–	–	–	–	< 0.18	–	–	< 0.10
HD36540^{s}	–	–	–	< 0.21	–	–	–	–
HD36629^{b}	–	–	–	–	< 0.35	–	–	–
HD36668^{s}	–	–	–	< 0.21	–	–	–	–
HD36916^{bc}	–	–	–	–	< 0.07	–	–	–
HD36960^{c}	–	–	–	–	< 0.12	–	–	–
HD37017^{abdeghr}	< 0.28	3.10 ± 0.40	2.10 ± 0.20	–	2.60 ± 0.06	–	2.40 ± 0.12	0.44 ± 0.08
HD37022^{g}	–	–	–	–	–	–	< 4.95	–
HD37041^{c}	–	–	–	–	< 0.30	–	–	–
HD37043^{a}	–	–	–	–	< 0.24	–	–	–
HD37058^{b}	–	–	–	–	< 0.31	–	–	–
HD37061^{ht}	–	–	–	–	0.68 ± 0.07	–	–	0.54 ± 0.14
HD37129^{a}	–	–	–	–	< 0.20	–	–	–
HD37140^{s}	–	–	–	< 0.20	–	–	–	–
HD37150^{f}	–	–	–	0.51 ± 0.07	–	–	–	–
HD37151^{s}	–	–	–	< 0.21	–	–	–	–
HD37210^{s}	–	–	–	< 0.26	–	–	–	–
HD37321^{b}	–	–	–	–	< 0.27	–	–	–
HD37479^{abdeg}	< 1.03	4.90 ± 0.40	3.70 ± 0.30	–	3.90 ± 0.10	–	3.20 ± 0.11	1.25 ± 0.28
HD37642^{f}	–	–	–	0.60 ± 0.07	–	–	–	–
HD37742^{i}	–	2.77 ± 0.05	–	1.10 ± 0.01	–	0.49 ± 0.03	–	–
HD37752^{c}	–	–	–	–	< 0.08	–	–	–
HD37776^{at}	–	–	–	–	< 0.25	–	–	< 0.10
HD37808^{ce}	< 0.36	–	–	–	0.97 ± 0.26	–	–	–
HD40312^{b}	–	–	< 0.46	–	0.31 ± 0.31	–	–	–

Table D1 – *continued*

Star	$F_{0.3}$	F_1	F_2	F_3	F_6	F_{13}	F_{20}	F_{50}
HD41269[c]	–	–	–	–	< 0.08	–	–	–
HD42509[c]	–	–	–	–	< 0.06	–	–	–
HD43819[c]	–	–	–	–	< 0.06	–	–	–
HD45105[c]	–	–	–	–	< 0.06	–	–	–
HD45583[fr]	–	–	–	0.27 ± 0.05	–	–	–	0.22 ± 0.04
HD46328[i]	–	< 0.05	–	< 0.02	–	< 45.00	–	–
HD47129[i]	–	0.39 ± 0.04	–	0.21 ± 0.01	–	< 0.03	–	–
HD47777[i]	–	< 0.03	–	< 0.04	–	–	–	–
HD49333[b]	–	–	–	–	< 0.22	–	–	–
HD49606[s]	–	–	–	< 0.20	–	–	–	–
HD50204[c]	–	–	–	–	< 0.06	–	–	–
HD51418[s]	–	–	–	< 0.21	–	–	–	–
HD52589[s]	–	–	–	< 0.17	–	–	–	–
HD57219[a]	–	–	–	–	< 0.33	–	–	–
HD57682[gi]	–	< 0.03	–	< 0.03	–	< 0.02	< 0.16	–
HD58260[ai]	–	< 0.08	–	< 0.04	< 0.18	< 0.03	–	–
HD60344[a]	–	–	–	–	< 0.20	–	–	–
HD61556[ot]	–	–	–	–	–	–	2.86 ± 0.81	1.21 ± 0.18
HD64740[t]	–	–	–	–	–	–	–	0.06 ± 0.01
HD65339[ab]	–	–	–	–	< 0.18	–	–	–
HD66665[i]	–	< 0.03	–	< 0.02	–	< 42.00	–	–
HD66765[t]	–	–	–	–	–	–	–	< 0.10
HD77653[o]	–	–	–	–	–	–	6.87 ± 1.60	6.87 ± 1.60
HD78556A[c]	–	–	–	–	< 0.06	–	–	–
HD79158[af]	–	–	–	0.45 ± 0.05	< 0.62	–	–	–
HD89822[a]	–	–	–	–	< 0.48	–	–	–
HD89897[c]	–	–	–	–	< 0.06	–	–	–
HD90044[c]	–	–	–	–	< 0.05	–	–	–
HD97441A[c]	–	–	–	–	< 0.12	–	–	–
HD98664[c]	–	–	–	–	< 0.10	–	–	–
HD100340[a]	–	–	–	–	< 0.43	–	–	–
HD105382[o]	–	–	–	–	–	–	2.20 ± 0.63	2.20 ± 0.63
HD109387[a]	–	–	–	–	< 0.18	–	–	–
HD112413[af]	–	–	–	0.29 ± 0.03	< 0.46	–	–	–
HD115735[c]	–	–	–	–	< 0.07	–	–	–
HD118022[p]	–	–	–	0.50 ± 0.25	–	–	–	–
HD120709[b]	–	–	–	–	< 0.24	–	–	–
HD120710[b]	–	–	–	–	< 0.21	–	–	–
HD122532[b]	–	–	–	–	< 0.18	–	–	–
HD124224[cdefoq]	1.32 ± 0.31	4.30 ± 0.10	4.60 ± 0.10	4.07 ± 0.14	3.80 ± 0.07	–	–	2.19 ± 0.24
HD125248[s]	–	–	–	< 0.22	–	–	–	–
HD125823[a]	–	–	–	–	< 0.55	–	–	–
HD126515[b]	–	–	–	–	< 0.18	–	–	–
HD130557[c]	–	–	–	–	< 0.18	–	–	–
HD131120[b]	–	–	–	–	< 0.21	–	–	–
HD133029[b]	–	–	–	–	< 0.22	–	–	–
HD133652[f]	–	–	–	0.24 ± 0.07	–	–	–	–
HD133880[fg]	–	–	–	4.08 ± 0.16	–	–	14.45 ± 0.11	2.04 ± 0.17
HD135679[c]	–	–	–	–	< 0.05	–	–	–
HD137193[b]	–	–	–	–	< 0.21	–	–	–

Table D1 – *continued*

Star	$F_{0.3}$	F_1	F_2	F_3	F_6	F_{13}	F_{20}	F_{50}
HD137909[a]	–	–	–	–	< 0.44	–	–	–
HD138764[c]	–	–	–	–	< 0.06	–	–	–
HD142184[ko]	–	160.00 ± 20.00	143.00 ± 2.00	121.00 ± 2.00	–	–	7.64 ± 1.75	7.64 ± 1.75
HD142250[s]	–	–	–	< 0.21	–	–	–	–
HD142301[bcde]	< 1.28	< 0.56	1.50 ± 0.30	2.76 ± 2.76	4.90 ± 0.08	–	1.81 ± 1.81	–
HD142884[b]	–	–	–	–	< 0.18	–	–	–
HD142990[bcdel]	< 0.54	< 0.52	< 0.42	1.98 ± 1.98	2.27 ± 0.07	–	< 3.30	1.10 ± 0.20
HD143473[f]	–	–	–	0.50 ± 0.07	–	–	–	–
HD143699[bs]	–	–	–	< 0.21	0.21 ± 0.21	–	–	–
HD144217[b]	–	–	–	–	< 0.21	–	–	–
HD144218[b]	–	–	–	–	< 0.21	–	–	–
HD144334[bce]	< 0.92	–	–	–	0.42 ± 0.42	–	< 0.80	–
HD144661[b]	–	–	–	–	< 0.18	–	–	–
HD144844[bs]	–	–	–	< 0.20	< 0.19	–	< 0.49	–
HD145102[s]	–	–	–	< 0.15	–	–	–	–
HD145482[b]	–	–	–	–	< 0.18	–	–	–
HD145501C[bcr]	–	–	–	1.67 ± 0.06	2.06 ± 0.07	–	1.57 ± 0.18	1.24 ± 0.12
HD145501D[b]	–	–	–	0.60 ± 0.60	0.42 ± 0.42	–	< 0.54	–
HD145502[b]	–	–	–	< 0.38	< 0.36	–	–	–
HD146001[b]	–	–	–	< 0.22	0.32 ± 0.32	–	< 0.84	–
HD147010[b]	–	–	–	–	< 0.20	–	–	–
HD147084[s]	–	–	–	< 0.17	–	–	–	–
HD147550[c]	–	–	–	–	< 0.17	–	–	–
HD147890[s]	–	–	–	< 0.20	–	–	–	–
HD147932[n]	–	–	20.00 ± 2.00	20.00 ± 2.00	20.00 ± 2.00	15.00 ± 2.00	10.00 ± 2.00	–
HD147933[m]	–	11.00 ± 0.10	11.00 ± 0.10	12.00 ± 0.10	12.00 ± 0.10	–	–	–
HD148112[a]	–	–	–	–	< 0.47	–	–	–
HD148199[b]	–	–	–	–	< 0.45	–	–	–
HD149438[i]	–	< 0.04	–	< 0.02	–	< 36.00	–	–
HD149822[c]	–	–	–	–	< 0.07	–	–	–
HD151346[b]	–	–	–	–	< 0.18	–	–	–
HD152107[ab]	–	–	–	< 0.15	< 0.40	–	–	–
HD156424[i]	–	0.49 ± 0.03	–	0.38 ± 0.01	–	–	–	–
HD157779[c]	–	–	–	–	< 0.07	–	–	–
HD159376[c]	–	–	–	–	< 0.06	–	–	–
HD162374[s]	–	–	–	< 0.33	–	–	–	–
HD163472[i]	–	< 0.03	–	< 0.02	–	< 0.03	–	–
HD164429[cf]	–	–	–	0.30 ± 0.05	0.30 ± 0.06	–	–	–
HD165474[s]	–	–	–	< 0.14	–	–	–	–
HD166182[s]	–	–	–	< 0.21	–	–	–	–
HD168785[s]	–	–	–	< 0.27	–	–	–	–
HD168814[c]	–	–	–	–	< 0.08	–	–	–
HD168856[s]	–	–	–	< 0.20	–	–	–	–
HD170000[f]	–	–	–	0.45 ± 0.05	–	–	–	–
HD170973[s]	–	–	–	< 0.16	–	–	–	–
HD171247[ce]	< 0.03	–	–	–	3.04 ± 0.09	–	–	–
HD174638[c]	–	–	–	–	3.55 ± 0.06	–	–	–
HD175132[cs]	–	–	–	< 0.14	< 0.07	–	–	–
HD175156[b]	–	–	–	–	< 0.18	–	–	–
HD175362[bcd]	–	–	–	< 0.21	0.38 ± 0.38	–	< 0.60	–

Table D1 – *continued*

Star	$F_{0.3}$	F_1	F_2	F_3	F_6	F_{13}	F_{20}	F_{50}
HD175744^{cs}	–	–	–	< 0.17	< 0.02	–	–	–
HD176582^{f}	–	–	–	0.46 ± 0.05	–	–	–	–
HD177003^{c}	–	–	–	–	< 0.07	–	–	–
HD177410^{c}	–	–	–	–	< 0.07	–	–	–
HD179527^{s}	–	–	–	< 0.16	–	–	–	–
HD182180^{jt}	–	18.00 ± 0.10	20.00 ± 0.10	20.00 ± 0.10	–	–	–	4.17 ± 0.42
HD183056^{c}	–	–	–	–	< 0.06	–	–	–
HD183339^{s}	–	–	–	< 0.17	–	–	–	–
HD184927^{cs}	–	–	–	< 0.17	< 0.07	–	–	–
HD184961^{s}	–	–	–	< 0.22	–	–	–	–
HD186205^{s}	–	–	–	< 0.21	–	–	–	–
HD187474^{s}	–	–	–	< 0.23	–	–	–	–
HD188041^{s}	–	–	–	< 0.21	–	–	–	–
HD191612^{i}	–	< 0.03	–	< 0.02	–	< 0.04	–	–
HD192678^{s}	–	–	–	< 0.17	–	–	–	–
HD196178^{f}	–	–	–	3.00 ± 0.07	–	–	–	–
HD196502^{a}	–	–	–	–	< 0.80	–	–	–
HD202671^{s}	–	–	–	< 0.15	–	–	–	–
HD205021^{i}	–	< 0.03	–	< 0.03	–	< 0.03	–	–
HD207538^{a}	–	–	–	–	< 0.35	–	–	–
HD207840^{s}	–	–	–	< 0.21	–	–	–	–
HD208057^{t}	–	–	–	–	–	–	–	< 0.05
HD208266^{s}	–	–	–	< 0.36	–	–	–	–
HD209339^{a}	–	–	–	–	< 0.29	–	–	–
HD214993^{s}	–	–	–	< 0.26	–	–	–	–
HD215441^{abdeg}	< 0.34	< 0.16	0.60 ± 0.10	–	1.10 ± 0.10	–	1.49 ± 0.10	0.98 ± 0.10
HD216916^{s}	–	–	–	< 0.21	–	–	–	–
HD223128^{s}	–	–	–	< 0.24	–	–	–	–
HD224801^{s}	–	–	–	< 0.23	–	–	–	–
HD224926^{a}	–	–	–	–	< 0.20	–	–	–
HD260858^{a}	–	–	–	–	< 0.18	–	–	–
HD264111^{a}	–	–	–	–	< 0.18	–	–	–
HD335238^{s}	–	–	–	< 0.16	–	–	–	–
ALS8988^{i}	–	< 0.04	–	< 0.02	–	< 30.00	–	–
ALS9522^{i}	–	< 0.03	–	0.08 ± 0.01	–	< 0.03	–	–
CPD-271791^{a}	–	–	–	–	< 0.18	–	–	–
CPD282561^{i}	–	–	–	< 0.02	–	< 0.03	–	–
NGC1624-2^{gi}	–	< 0.04	–	< 0.02	–	< 0.02	< 0.21	–